Probabilistic Modeling of Polycrystalline Alloys for Optimized Properties

by

Abhishek Kumar

A dissertation submitted in partial fulfillment
of the requirements for the degree of
Doctor of Philosophy
(Aerospace Engineering)
in The University of Michigan
2014

Doctoral Committee:

Associate Professor Veera Sundararaghavan, Chair
Associate Professor Vikram Gavini
Assistant Professor Nakhiah Goulbourne
Professor Anthony M. Waas

The power of God is with you at all times; through the activities of mind, senses, breathing, and emotions; and is constantly doing all the work using you as a mere instrument.

Bhagwat Gita

To my Mother Late Usha Sharma

ACKNOWLEDGEMENTS

I wish to acknowledge the gracious support of many people for their contributions towards this work both directly and indirectly. First, I thank my advisor, Prof. Veera Sundararaghavan who patiently guided me through all phases of this work. He is a true role model, and the best professor I have ever seen. I am deeply indebted to him for financial support, and for the academic resources he provided. The time and effort of Prof. Anthony Waas, Prof. Nakihah Golulbourne and Prof. Vikram Gavini as committee members is greatly appreciated.

I would like to thank Dr. Umesh Gandhi and team members of FRD in Toyota Technical Center, Ann Arbor. I was able to learn lots of skill with research while doing coop there.

I would like to thank all my labmates from the our MSSL research group, Shang, Sriram, Shardul, Adam and Nick for having always motivated and accompanied me throughout the challenges of research. Without their help, this dissertation would have been much more difficult. I acknowledge the past and the present members of the labs of Prof. John Allison, Prof. Anthony Waas and Prof. Vikram Gavini for the stimulating research discussions.

The great time I had in Ann Arbor would not have been possible without my great friends Ajay Sharma, Anurag, Mridul, Riddhiman and many others. They created a home away from home for me and I was very fortunate to be in their company.

I would like to thank Madhavi, Mayank, Prithvi, Ruchika, Sarvesh and my friends in India and all over the world for their friendship and support throughout my entire

life. They motivated and encouraged me to take this academic journey and always pushed me to do things for which I am suited the best. I will always remain indebted to them.

I would also like to thank the services provided by Research Computing Department at University of Michigan. I am also thankful to our Graduate coordinator Denise Phelps of Aerospace Engineering at the University of Michigan for her support during my graduate study.

Lastly, none of this would have been possible without the love and support of my family. I would like to thank my parents, Gadadhar Sharma and Usha Sharma for their support, suggestions and invaluable encouragement that have always made me a better man and have indirectly prepared me to tackle challenges that I came across. Without my parents support and encouragement, I never would have made it this far. I have also been blessed with the most lovely and caring wife in Naina who has become my pillar of strength in the short time that we have been together. Her sacrifice staying with me in a totally different culture and foreign country will never be forgotten.

TABLE OF CONTENTS

DEDICATION ii

ACKNOWLEDGEMENTS iii

LIST OF FIGURES vii

LIST OF TABLES xii

ABSTRACT xiii

CHAPTER

I. Introduction 1

II. Markov Random Fields for synthesis of metallic microstructures 7

2.1 Mathematical modeling of microstructures as Markov Random fields 8
2.2 Examples 11
2.2.1 Comparison of moment invariants 14
2.2.2 Comparison of microstructure sensitive properties . 18
2.2.3 Example 2. Aluminum alloy AA3002 representing the rolling plane 20
2.3 Algorithm for reconstruction of 3D microstructures 22
2.4 Results 25
2.4.1 Validation tests 27
2.4.2 Elastic properties of two phase composite 27
2.5 Conclusions and Summary 29

III. Microstructural modeling of BCC Galfenol 36

3.1 Microstructure Evolution Direct Problem 37

3.2 Single crystal model of magnetostriction 38
3.3 Numerical Examples 42

IV. Structure-property optimization in Galfenol through data mining of probabilistic descriptors 50

4.1 Modeling of texture 51
4.1.1 Representation in Rodrigues space 51
4.2 Property representation and optimization in Rodrigues space 52
4.2.1 Calculation of properties 54
4.3 Traditional structural optimization design 55
4.3.1 Linear programming 56
4.3.2 Genetic algorithms 57
4.4 Structural optimization with data mining 57
4.4.1 Framework 58
4.4.2 Database construction 59
4.4.3 Feature selection 62
4.5 Material Design Problems 63
4.5.1 4-step optimization 64
4.5.2 Optimization results 66
4.6 Conclusion 69

V. Microstructure modeling using statistical correlation functions 70

5.1 Representation of the conditional orientation correlation function 72
5.2 Probability update in finite element spaces 75
5.2.1 Case of rotationally invariant COCF: 81
5.2.2 Symmetry constraints in the COCF 82
5.3 Constitutive modeling 83
5.3.1 Interaction Law 85
5.4 Numerical examples 88
5.5 Conclusion 100

VI. Suggestions for future research 103

6.1 Key Contributions of the dissertation 103
6.2 Development of Process Design Methodologies 104
6.3 Extending the approach to other alloys, including HCP metals 106

BIBLIOGRAPHY 111

LIST OF FIGURES

Figure

1.1 *Multiscale modeling using descriptors: The initial microstructure is sampled to obtain the descriptor which is then represented in a finite element mesh. The descriptors are directly evolved during thermomechanical processing to compute change in properties.* 4

2.1 *Markov random field as an undirected graph model, circles are pixels in the image and bonds are used to connect neighbors: (a) Ising model with nearest neighbor interactions (b) Microstructure modeled by including higher order interactions in the Ising model.* 8

2.2 *The Markov random field approach [39, 146]: The image is grown from a 3x3 seed image. As the algorithm progresses, the output pixel (shown in red) is computed by searching for a pixel with a similar neighborhood (shown in blue) in the input image.* 10

2.3 *Effect of Window size, none of the image looks similar to sample image but image generated with window size of 11 has statistical correlation function very much similar to that of sample image.* 12

2.4 *Initial microstructure (left) and the synthesized microstructure (right) from our Markov random field code. Note that local features such as grain boundaries are effectively captured.* 13

2.5 *Statistics of synthesized images are compared with the seed image. The mean intercept length and rose of intersections are shown. Note that none of the synthesized images are identical to the seed image, yet global statistics of the seed image are well captured.* 14

2.6 *Reconstruction of an experimentally measured AA3002 Aluminum alloy microstructure [142] using Markov random Field algorithm. The larger microstructure from which the input image is taken is also shown for comparison. Purple regions are cube/near cube grain orientations, yellow/red regions are non-cube orientations. The fine dark spots are the intermetallic phases.* 15

2.7 *Color histograms of the input microstructure and reconstructed microstructure are compared. A novel color blot method is used to compare the distribution of cube/near cube regions, and intermetallic phases in the input and synthesized images.* 16

2.8 *SOMIM density map original(left) and synthetic(right)* 17
2.9 *PMIM density map original(left) and synthetic(right)* 17
2.10 *Comparison of the sample image statistical features with the features of the reconstructed image shown in Fig.2.3. (a) The autocorrelation function and (b) the three-point probability function S3(r,s,t) shown for s=t=5(long range correlation) and s=t=3(short range correlation)* 20
2.11 *Comparison of the distribution of the normal stress σ_y in GPa for (a)sample image (b) Synthesized image (c)Color histogram of stress contour for sample image (d) Color histogram of stress contour for synthesized image* 21
2.12 *Variation of Young Modulus with temperature for sample and synthesized image also that obtained in experiment* 22
2.13 *(a) Comparison of the equivalent stress-strain curve predicted through homogenization with Taylor Simulation for Sample and two Synthesized image (b) Variation of Young Modulus with angle of rotation for sample and synthesized image* 30
2.14 *ODF Plot for sample and synthesized image for rolling case* 30
2.15 *Comparison of the distribution of the equivalent stress with color histogram* 31
2.16 *The neighborhoods of v in the slices orthogonal to the x, y, and z axis, respectively, are shown. The windows in the input 2D micrograph shown in dotted lines are denoted by $\boldsymbol{S}_v^i$ $(i = x, y, z)$. These windows closely resemble the neighborhoods of v.* 31
2.17 *a. Input 2D microstructure showing an isotropic distribution of solid circles. b. 3D reconstruction c. 3D sectional images of the reconstructed microstructure.* 32
2.18 *a. An anisotropic case with solid circles in the z-slice (similar to case (i)) but an interconnected lamellar structure in the x- and y- slices. b. 3D reconstruction c. 3D sectional images of the reconstructed microstructure.* 33
2.19 *a. An experimental 2D polycrystalline microstructure. b. 3D reconstruction c. 3D sectional images of the reconstructed microstructure.* 34
2.20 *Comparison of the features of the 2D and reconstructed image shown in Fig. 2.16. (a) Two point probability function. (b) Three point probability function* 34
2.21 *Experimental Tungsten-silver composite image ($204 \times 236 \mu m$) from Umekawa et al. [135]. The black and white image corresponds to a thresholded image with white representing the silver phase and black representing Tungsten. A 64 μm square cell shown in inset was used to reconstruct the 3D image. (b) A 64 μm length cell of reconstructed 3D microstructure of the experimental image showing silver distribution (c) The tungsten phase of the reconstructed microstructure.* . . 35

2.22 *Comparison of properties of 3D reconstruction of Silver-Tungsten composite (a) The autocorrelation function for the silver phase (b) Experimental Young's modulus is shown along with the FEM results for the reconstructed 3D microstructure.* 35
3.1 *(left) Comparison of textures (Euler angle space, $\phi_2 = 45^o$) predicted by our model (Fig. 3.1(b)) with experiments on BCC iron in Fig. 3.1(c) [17]. Experimental rolling textures of BCC Fe-16.83%Ga results (Fig 3.1(a) [79]) are also shown. The experiment indicates a $\{112\} < 132 >$ texture in addition to the expected γ texture. (right) Comparison of results of current model with published results in [79]. The plot shows tensile test curves of as-cast polycrystalline Galfenol at different temperatures.* 44
3.2 *Final microstructure after rolling to 1% strain and unloading. The mis-orientation distribution over grains that depicts the change in Neo-Eulerian angle from the initial configuration (t=0).* 45
3.3 *Magnetostrictive $\lambda - H$ and B-H response for various compressive pre-stress values of 0, 15, 30, 45, 60 and 80 MPa along* [100] *and* [210] *crystallographic direction.* 46
3.4 *Magnetostrictive $\lambda - H$ response of polycrystal for various compressive pre-stress values of 0, 15, 30, 45, 60 and 80 MPa* 47
3.5 *Effect of Annealing Process on magnetostriction process* 48
3.6 *Magnetostrictive strain distribution in the as-rolled microstructure (to 1 % strain) under a y-direction magnetic field of 251.33 Oe. (a) Magnetostrictive strains along x-direction and (b) strains along the y- direction.* 49
4.1 *Framework of Data Mining based Material Structure Optimization* . 60
4.2 *ODF values that satisfy the Objective Function E* 67
4.3 *ODF values that satisfy the Objective Function Y* 67
4.4 *ODF values that satisfy the Objective Function m* 67
4.5 *ODF values for all 26 possible cases that satisfy the Objective Function F_2* 68
5.1 *(a) COCF ($\mathcal{F}(\boldsymbol{g}'|(\boldsymbol{g},\boldsymbol{r}))$) gives the probability density of occurrence of an orientation $\boldsymbol{g}'$ at the end point of a vector $\boldsymbol{r}$ emanating from orientation g. (b) Sampling along all directions results in a rotationally invariant OCF with scalar r. (c) Direction sensitive sampling for a vector representation of $\boldsymbol{r}$* 72
5.2 *COCF mesh representation for a planar microstructure (with fundamental region being a line between $-\pi/2$ to $\pi/2$). The $\boldsymbol{r}$ mesh is a semicircle with each node point giving the distance and orientation of a vector $\boldsymbol{r}$ drawn from orientation $\boldsymbol{g}$. Orientation $\boldsymbol{g}'$ located at the end of vector $\boldsymbol{r}$ is represented using a fundamental region connected to each node in the $\boldsymbol{r}$ mesh.* 75

5.3 *Probability update scheme in FE space: During deformation, the nodal points ($\boldsymbol{g}$) of the FE mesh are moved to reflect reorientation ($\Delta\boldsymbol{g}$) of crystals. The new ODF is obtained using Eq. 5.11 that ensures that the normalization constraint (Eq. 5.9) is met in the reoriented mesh.* 77

5.4 *During deformation, the two–point descriptor evolves due to reorientation of crystals with initial orientation $\boldsymbol{g}'$ and $\boldsymbol{g}$ at the end points of vector $\boldsymbol{r}$. In addition, both the length and orientation of $\boldsymbol{r}$ vector changes during deformation.* 80

5.5 *Real part of Green's function operator $G_{11,11}(\boldsymbol{r})$ for a 2D microstructure. The function peaks at $\boldsymbol{r} = (0, 0)$ and decays to zero at large $\boldsymbol{r}$.* 86

5.6 *(a) The initial (periodic) RVE with 324 elements and 36 crystals. Each crystal is divided into 9 elements. (b) The initial ODF sampled from the RVE is plotted on a finite element grid in the fundamental region $(-\pi/2, \pi/2)$. Both locations of nodal points and integration points are indicated.* 89

5.7 *Illustration of the sampling approach for COCF: (a) Sample a pixel in a grain with orientation g corresponding to a node point in the M_g mesh (b) Draw a line passing through the pixel to identify the orientation g' at a distance r, increment the weights in a 3D array $F(g, r, g')$ (c) Sample lines at various angles to capture orientation dependence. The lengths and orientation of the lines are chosen based on the location of node points in the $M_{r|g}$ mesh.* 90

5.8 *Various meshes used to discretize the $\boldsymbol{r}$ space for testing the convergence of the Green's function approach. The Green's function $G_{11,11}$ is superposed on the r-mesh as a color contour.* 92

5.9 *Convergence with respect to r–mesh: The y-axis shows the l_2 norm of the change in nodal coordinates when using the current mesh (compared to the previous coarser mesh). The final microstructure at $t = 1$ sec is also shown for all cases. An 82 element mesh in the r-space was chosen based on this study.* 93

5.10 *The final texture predicted by the COCF model is shown. There is strong tendency for crystals with smaller angles (close to the origin) to reorient farther away from the origin. An increase in the ODF close to an ideal orientation of $\theta = \pm\pi/2$ is seen.* 95

5.11 *Visualization of Lagrangian COCF $\hat{F}(\boldsymbol{g}'|(\boldsymbol{g} = -\pi/2, \boldsymbol{r}))$: The circles correspond to various values of $\boldsymbol{g}'$ from $(-\pi/2, \pi/2)$. The probability density of orientations $\boldsymbol{g}'$ at various distances $\boldsymbol{r}$ from orientation $\boldsymbol{g} = -\pi/2$ is shown over the r-mesh. The first mesh corresponds to $\hat{F}(\boldsymbol{g}' = -\pi/2|(\boldsymbol{g} = -\pi/2, \boldsymbol{r}))$, the second mesh corresponds to $\hat{F}(\boldsymbol{g}' = -0.39\pi|(\boldsymbol{g} = -\pi/2, \boldsymbol{r}))$ etc. The evolved COCF at $t = 1$ sec is also shown.* 96

5.12 *Visualization of Lagrangian COCF* $\hat{F}(\boldsymbol{g}' = -\pi/2|(\boldsymbol{g}, \boldsymbol{r}))$*: The circles correspond to various values of* $\boldsymbol{g}$ *from* $(-\pi/2, \pi/2)$*. The probability density of orientation* $\boldsymbol{g}' = -\pi/2$ *at various distances* $\boldsymbol{r}$ *from orientations* $\boldsymbol{g}$ *is shown over the r-mesh. The evolved COCF at* $t = 1$ *sec is also shown. The COCF shown here is closely related to that shown in Fig. 5.11 through the switching symmetry.* 97

5.13 *Switching symmetry of the COCF at* $t = 1$ *sec: The COCF* $\hat{F}(\boldsymbol{g}' = 0.055\pi|(\boldsymbol{g} = -0.5\pi, \boldsymbol{r}))$ *can be seen to be equal to* $\hat{F}(\boldsymbol{g}' = -0.5\pi|(\boldsymbol{g} = 0.055\pi, \boldsymbol{r}))$ *after multiplying it with the scaling factor* $\frac{\mathcal{P}(\boldsymbol{r}|\boldsymbol{g})\mathcal{A}(\boldsymbol{g})}{\mathcal{P}(\boldsymbol{r}|\boldsymbol{g}')\mathcal{A}(\boldsymbol{g}')}$*.* . . 98

5.14 *(a) Comparison of the Lagrangian ODF predicted by the Taylor and COCF model at times t = 0.1,0.4,0.7 and 1.0 sec. (b,c) The ODF values at* ± 85.8 *degrees predicted by the Taylor and COCF models are compared with that predicted by the aggregate model.* 99

5.15 *Direct comparison of the microstructure predicted by (a) aggregate and (b) COCF model. The average velocity gradient predicted by the COCF model (for each orientation) is used to update the microstructure mesh.* 100

5.16 *Comparison of error in (a) crystal orientations and (b) nodal coordinates that arise in Taylor and COCF models. The errors correspond to* l^2 *norm of the difference in values between Taylor/COCF models with respect to the aggregate model. Errors are plotted as a function of simulation time.* 101

5.17 *(a) COCF model reduces the error in prediction of displacements and orientations by 30 % when compared to the Taylor model. (b) Comparison of computational speed of aggregate model with respect to COCF model as number of elements in RVE increases.* 101

6.1 Pyramidal, basal, and prismatic slip systems used in titanium simulations 107

6.2 Comparison of texture evolution of Ti under plane strain compression using our ODF model after 200 sec of simple compression at the rate of $1e-3s^{-1}$ 108

6.3 (a) Comparison for Pole Figure (b) Comparison of equivalent stress-strain response with results from experiments 110

LIST OF TABLES

Table

2.1 Elastic properties of silver and tungsten phases as a function of temperature (from Ref. [107]) 28
4.1 Feature rankings produced by various methods 65
4.2 Comparison of Optimal Value for different property 68
5.1 Algorithm for COCF evolution 94
6.1 Value of elastic parameters for single crystal HCP Titanium Alloys [121] 109
6.2 Crystal Plasticity parameters for HCP 109

ABSTRACT

On Probabilistic Representations of Microstructure for Multi-scale Modeling

by

Abhishek Kumar

Chair: Veera Sundararaghavan

In this thesis, several innovative methods for microstructure representation, reconstruction, property analysis and optimization are developed. Metallic microstructures are stochastic by nature and a single snapshot of the microstructure does not give the complete variability. However, experiments to assess the complete microstructure map of large aerospace structures are computationally prohibitive. One contribution of this thesis is on the development of a Markov Random Field approach to generate microstructures from limited experimental measurements of the microstructure. The result is a simple method for generating 3D microstructures from 2D micrographs that generates visually striking 3D reconstructions of anisotropic microstructures and is computationally efficient.

Traditionally, finite elements techniques have been used to analyze properties of metallic microstructures. While finite element methods forms a viable approach for modeling a few hundred grains, a macroscale component such as turbine disk contains millions of grains and simulation of such 'macroscale' components is a challenging task even when using current state-of-the-art supercomputers. In addition, finite element simulations are deterministic while polycrystalline microstructures are

inherently stochastic in nature. An alternate class of schemes have been developed in this work that allows representation of microstructure using probabilistic descriptors.. We have employed this descriptor to represent the microstructure of an Iron-Gallium alloy (Galfenol). We have developed computational methods to link these properties with the ODF descriptor. Subsequently, we have employed data mining techniques to identify microstructural features (in the form of ODFs) that lead to an optimal combination of magnetostrictive strains, yield strength and elastic stiffness.

Since ODF representation does not contain information about the local neighborhood of crystals, all crystals are subject to the same deformation and equilibrium across grain boundaries is not captured. We also done preliminary work on the use of higher order probability descriptors that contains neighborhood information. Of specific interest is the two–point correlation function(COCF) that arises in known expressions for mechanical and transport properties. The improvement in prediction of texture and strains achieved by the COCF approach is quantified through deformation analysis of a planar polycrystalline microstructure.

CHAPTER I

Introduction

Integrated Computational Materials Engineering (ICME) is an emerging paradigm for materials design that emphasizes integration of material models at multiple length scales with engineering analysis of products and processes. For example, during simulation of metal forming processes, microstructure evolution can be explicitly tracked to facilitate design of processing paths that lead to optimized microstructure. At the microstructural level, a popular material model is based on finite element analysis of polycrystalline aggregates via crystal plasticity theory ([20, 28, 99, 18, 116, 126, 100]). Here, microstructure evolution in the form of reorientation of crystals(texturing) is modeled by deforming an aggregate of grains characterized using microdiffraction techniques. Deformation mechanisms such as dislocation slip and twinning are modeled using constitutive laws based on state variables such as dislocation densities or slip system resistances along various slip systems. Reorientation of grains and evolution of the threshold stress along each slip system due to various hardening mechanisms (self-hardening, latent hardening etc.) are modeled. The grain-level stresses are averaged to obtain the mechanical response (stress-strain curve) and crystallographic texture is post-processed. While CPFE forms a viable approach for modeling a few hundred grains, a macroscale component such as turbine disk contains millions of grains and simulation of such 'macroscale' components is a challenging task

even when using current state-of-the-art supercomputers. Thus, such simulations have not yet been successfully integrated (via two-way, run time coupling) to commercial deformation process simulation (FE) codes. Instead, several codes employ phenomenological models or decouple such material models from engineering software (through postprocessing). These methods lead to oversimplifications and often significant deviations from real behavior. In addition, finite element simulations are deterministic while polycrystalline microstructures are inherently stochastic in nature and a single snapshot of the microstructure does not predict the correct behavior of the material.

In the second chapter of the thesis, a novel method to sample microstructures is presented. Of particular interest in this work is sampling of 2D and 3D microstructures from limited information known through experiments. Towards this end, Voronoi construction has been used in several studies in modelling polycrystalline microstructures [150, 73, 138]. Microstructures are generated by altering the voronoi cell generator points, altering aspect ratios [27] and orientations. However, Voronoi constructions are largely an idealization and do not account for the complexity of real microstructures (eg. non-convex grain shapes). Physics based simulations based on Monte Carlo and phase field methods are computationally intensive and several parameters (eg. nucleation models, free energy models) need to be carefully calibrated from experiments. Markov Random Field methods developed in this thesis provide an efficient route to sample microstructures [39]. Given a small input microstructure, these algorithms can reconstruct larger microstructures pixel-by-pixel using patten matching algorithms. An inverse problem of specific interest in this thesis is the reconstruction of 3D microstructures from three orthogonal 2D sectional images taken along the x-, y- and z- planes. The information contained in these three 2D micrographs is in the form of pixels containing colors corresponding to different constituent phases. The outcome of the inverse problem is a 3D microstructure con-

taining voxels colored consistently such that any arbitrary x-, y- or z- slice 'looks' similar to the corresponding input micrographs. This reconstruction problem leads to anisotropic microstructures, which is in contrast to other such works in literature that use a single reference (2D) image and make assumptions of microstructural isotropy, i.e. slices in every direction look similar to a single input image [127]. Most popular among these methods involve matching statistical features like two-point correlation functions of a single planar image to a random 3D image using optimization procedures like simulated annealing [147, 88]. Extension of these methods to achieve anisotropic microstructures have been proposed in the past using directionally dependent statistical features [108]. However, these methods are restricted to simple two-phase microstructures and are not applicable to more complex microstructures such as metallic polycrystals. The approach proposed here involves maximizing the similarity between the solid microstructure and the 2D sectional microstructures by minimizing a neighborhood cost function. This cost function ensures that the local neighborhood on 2D slices taken along the x-,y- or z- directions through the 3D microstructure is similar to some neighborhood in the 2D micrograph imaged along that plane. The result is a simple method for generating 3D microstructures from 2D micrographs that generates visually striking 3D reconstructions of anisotropic microstructures, is computationally efficient and is applicable to diverse microstructures.

In the subsequent chapters of this thesis, an alternative to computationally expensive crystal plasticity finite element methods is studied. In this approach, probabilistic descriptors are modeled rather than actual microstructure during property computation. The simplest of these descriptors is the one-point probability measure, the orientation distribution function ($\mathcal{A}(\boldsymbol{g})$), which quantifies the volume fractions of crystals in the orientation space ($\boldsymbol{g}$). Under an applied deformation, texturing is simulated by numerically evolving the ODF using conservation laws [34]. Conventional solution schemes are based upon representation of the ODF using a series of

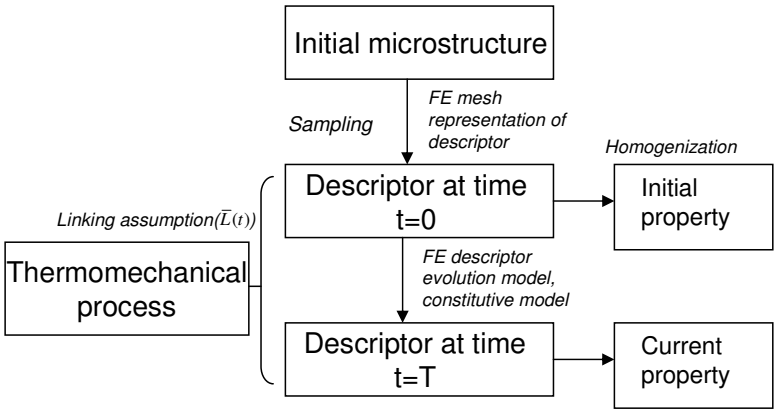

Figure 1.1: *Multiscale modeling using descriptors: The initial microstructure is sampled to obtain the descriptor which is then represented in a finite element mesh. The descriptors are directly evolved during thermomechanical processing to compute change in properties.*

harmonics [63, 29, 2, 60] or finite elements [66, 67]. We have employed this descriptor to represent the microstructure of an Iron-Gallium alloy (Galfenol). Galfenol is a recently discovered lowcost alloy that has several attractive properties including low magnetic hysteresis, high mechanical strength and good magnetostrictive strains under low magnetic fields. When a magnetic field is applied to Galfenol single crystal, the boundaries between the magnetic domains shift and rotate, both of which cause a change in the material's dimensions. This behavior, termed magnetostriction, has been successfully to transduce magnetic field to mechanical force in micro–scale (MEMS) sensors and actuators. While single crystals of Galfenol provide large magnetostriction, their preparation is expensive. It is well known that thermomechanical processes (such as rolling and extrusion) may provide means to develop polycrystalline Galfenol with properties comparable to expensive single crystals [61]. However, it has proved difficult to predict (and thus, control) the large changes in properties such as magnetostriction and yield strength that occur during thermomechanical processing. For example, warm rolled and annealed specimens retain high magnetostriction but are quite brittle; whereas, cold rolled specimens have high yield strength but lose their magnetostriction [31, 16]. Consequently, it is important to study the effect of

meso–scale features (such as texture, misorientation distribution) on the response of these alloys. For example, experimental studies suggest that internal inhomogeneous strains introduced by microstructural changes play an important role in determining the final magnetostriction in Galfenol [52]. In chapter 3, we have calibrated a rate-independent elasto-plastic model of BCC Galfenol single crystal for studying the effect of forming processes on the microstructure response. Both loading and unloading processes have been simulated and a finite strain homogenization algorithm has been developed to investigate microstructural response under coupled magnetic and stress fields. In chapter 4 of the thesis, we have used this model to identify microstructural features (in the form of ODFs) that lead to an optimal combination of magnetostrictive strains, yield strength and elastic stiffness is developed.

Since ODF representation does not contain information about the local neighborhood of crystals, Taylor assumption [132] is typically used where all crystals are subject to the same macroscopic strain and equilibrium across grain boundaries is not captured. In chapter 5 of the thesis, we investigate a higher order probability descriptor, the orientation correlation function (OCF), for representing polycrystalline microstructures. The OCF arises in known expressions for mechanical and transport properties [108, 22] and correlates with defect-sensitive properties such as stress corrosion cracking and creep [137]. The OCF defined by $\mathcal{F}(\boldsymbol{g}', \boldsymbol{g}, \boldsymbol{r})$, gives the probability density of finding orientations $\boldsymbol{g}'$ and $\boldsymbol{g}$ at the end points of a randomly placed vector $\boldsymbol{r}$ within the microstructure. In addition to containing volume fraction information, the OCF also contains crystal neighborhood information that can be used in models that predict interactions between grains. Finite element representation of the two–point measure is challenging due to its high dimensionality, for example, nine–dimensional elements are needed to fully discretize the OCF for a 3D FCC polycrystal. Analytical approximations in the form of exponentially decaying functions (based on the Corson's model, [36, 47]) have been developed for approximating the

two–point probability function. More recently, Adams exploited the use of intermediate representation called 'texture functions', approximated in Fourier space [4]. However, these are global approximations and are not efficient in capturing sharp changes in the two–point probability function that occur in real microstructures. In this work, we attempt to develop a simplified finite element representation of the two–point measure using an approach analogous to 'separation of variables' method used for solving differential equations. Here, the OCF is described using interconnected layers of meshes in $\boldsymbol{g}$, $\boldsymbol{r}$ and $\boldsymbol{g}'$ spaces. The conditional orientation correlation function (COCF), $\mathcal{F}(\boldsymbol{g}'|(\boldsymbol{g},\boldsymbol{r}))$ is described using a finite element mesh in the 3D orientation space of $\boldsymbol{g}'$. This mesh is linked to a node $\boldsymbol{r}$ in a separate mesh representing the local neighborhood of orientation $\boldsymbol{g}$. As the microstructure evolves, the crystal reorientations close to an orientation ($\boldsymbol{g}$) is captured by updating probability fields in these interconnected finite element meshes. A novel total Lagrangian approach has been developed that allows evolution of probability densities while satisfying basic normalization constraints. The piecewise polynomial functions used to represent the COCF allow ease of construction of various orientation transformations, such as differencing, interpolation and projection. The improvement in prediction of texture and strains achieved by the COCF approach over ODF–based methods has been quantified through simple deformation analysis of a planar polycrystalline microstructure. For this simulation, we employ a viscoplastic (non–hardening) constitutive model and a Green's function based first order correction to the Taylor model previously developed in [3]. In contrast to finite element methods for which simulation time increases with the size of the RVE, the simulation time is practically constant with the size or discretization of the microstructure. For realistic microstructures, the COCF approach is expected to be significantly faster than FE approaches. In chapter 6 of the thesis, we propose some future work in this area, including extension of the approach to other alloys (HCP Titanium) .

CHAPTER II

Markov Random Fields for synthesis of metallic microstructures

Microstructures and resulting properties are stochastic in nature and a single snapshot of the microstructure does not give the complete variability of microstructure. However, experiments to assess the complete microstructure map of large naval structures are computationally prohibitive. It is of interest to generate various possible microstructures from limited information known through experiments. We are interested in the following criteria for characterizing the reconstructed microstructures:

- The reconstructed microstructure must 'look like' the seed image. The similarity measures in this work come from the field of metallography/crystallography including lower order statistics (eg. grain size distribution, orientation distribution function) and finer statistical features (eg. grain boundary connectivity descriptors, higher order orientation correlations).

- Physical properties of the microstructure such as elastic moduli must be within reasonable bounds to the properties of the original microstructure. The properties were tested using finite element models and compared to experiments and bounding theories.

2.1 Mathematical modeling of microstructures as Markov Random fields

Some of early attempts at microstructure modeling were based on Ising models [58]. In the Ising model, a $N \times N$ lattice (L) is constructed with values X_i assigned for each particle i on the lattice, $i \in [1, .., N^2]$. In an Ising model, X_i is a binary variable equal to either $+1$ or -1 (eg. magnetic moment [58]). In this work, the values X_i may contain any one of G color levels in the range $\{0, 1, .., G-1\}$ (following the integer range extension of the Ising model by Besag [23]). A *coloring* of L denoted by $\boldsymbol{X}$ maps each particle in the lattice L to a particular value in the set $\{0, 1, .., G-1\}$. Ising models fall under the umbrella of *undirected graph models* in probability theory. In order to rewrite the Ising model as a graph, we assign neighbors to particles and link pairs of neighbors using a bond as shown in Fig. 2.1(a). The rule to assign neighbors is based on a *pairwise Markov property*. A particle j is said to be a neighbor of particle i only if the conditional probability of the value X_i given all other particles (except (i, j), i.e., $p(X_i|X_1, X_2, .., X_{i-1}, X_{i+1}, .., X_{j-1}, X_{j+1}, .., X_{N^2})$) depends on the value X_j.

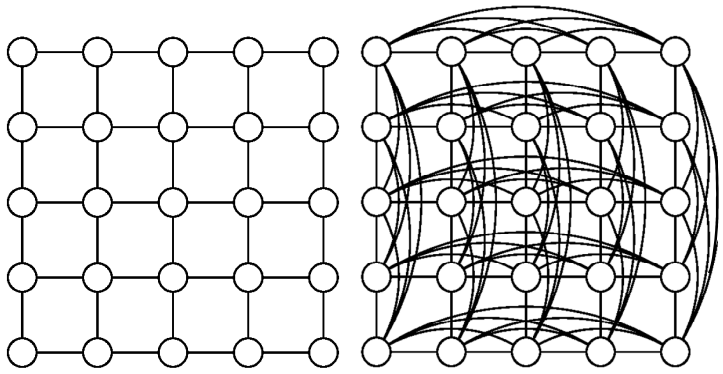

(a) (b)

Figure 2.1: *Markov random field as an undirected graph model, circles are pixels in the image and bonds are used to connect neighbors: (a) Ising model with nearest neighbor interactions (b) Microstructure modeled by including higher order interactions in the Ising model.*

Note that the above definition does not warrant the neighbor particles to be close in distance, although this is widely employed for physical reasons. For example, in the classical Ising model, each particle is bonded to the next nearest neighbor as shown in Fig. 2.1(a). In this work, we assume that a microstructure is a higher order Ising model (Fig. 2.1(b)). The particles of the microstructure correspond to pixels of the 2D image (or voxels in 3D). The neighborhood of a pixel is modeled using a square window around that pixel and bonding the center pixel to every other pixel within the window. The window size is a parameter that is chosen based on the scale of the biggest regular feature (eg. grain size). Using this graph structure, a *Markov random field* can be defined as the joint probability density $P(\boldsymbol{X})$ on the set of all possible colorings $\boldsymbol{X}$, subject to a *local Markov property*. The *local Markov property* states that the probability of value X_i, given its neighbors, is conditionally independent of the values at all other particles. In other words, $P(X_i|\text{all particles except i}) = p(X_i|\text{neighbors of particle i})$. Microstructures are obtained by sampling the Markov random field $P(\boldsymbol{X})$. In this chapter, we present methods to sample microstructures by sampling the conditional probability density $p(X_i|\text{neighbors of voxel i})$ from available 2D experimental data.

Markov random fields for texture synthesis

The approach is based on Claude Shannon's generalized Markov chain [119]. In the one dimensional problem, a set of consecutive pixels is used as a template to determine the probability distribution function (PDF) of the next pixel. Efros and Leung [39] extended the concept of Markov chain to 2D images. The texture is grown layer–by–layer from a small seed image (3x3 pixels) taken randomly from the sample. Explicit construction of the probability model for pixels is difficult. Instead, to synthesize a pixel, the algorithm first finds all windows in the sample image that are similar to the unknown pixel's neighborhood window. One of these matching windows is chosen and its center pixel is taken to be the newly synthesized pixel (Fig.

2.2). The measure of similarity between different windows is given by a normalized

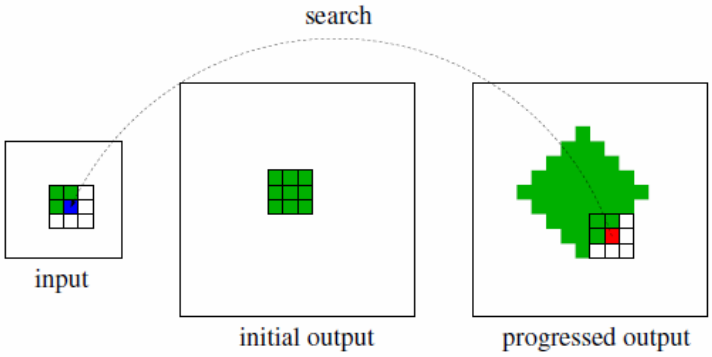

Figure 2.2: *The Markov random field approach [39, 146]: The image is grown from a 3x3 seed image. As the algorithm progresses, the output pixel (shown in red) is computed by searching for a pixel with a similar neighborhood (shown in blue) in the input image.*

sum of weighted squared differences. The weights for nearby pixels are taken to be greater than for pixels far away (Gaussian weighting kernels are typically used). All matches within p% (p=10 in [39]) of the match are considered. The center pixel values of patches in the list give a histogram for the unknown pixel, which can then be sampled, either uniformly or weighted by the distance. Note that for any pixel the values of only some of its neighborhood pixels will be known. The distance measure is computed by only matching on the known values and normalizing the error by the total number of known pixels.

The fundamental approximation in this numerical implementation is that the probability distribution function (PDF) of an unfilled pixel is assumed to be independent of the PDF of its unfilled neighbors. In other words, PDF for a pixel that is obtained by sampling may not stay valid as the rest of its neighbors are filled in. This is addressed by choosing the size of window as an adjustable parameter.

2.2 Examples

Markov random field algorithm for microstructure synthesis was performed on two different seed microstructures (1) Polycrystalline structure with grayscale data (from [77]) (2) An experimental RGB microstructure of AA3002 Aluminum alloy [142]. The free parameter in the reconstruction is the sampling window size which is taken to be $w = 13 \times 13$ pixels for case (1) and $w = 7 \times 7$ pixels for case (2). The window sizes are related to the grain size distribution in the image and can be calibrated using these reference microstructures. In Fig 2.3 we have demonstrated the effect of window size on quality of synthesized image. Higher the window size better the image quality, we have observed that close to window size of '11' synthesized image resembles very close to that of sample input both visually as well as when comparing statistical correlation functions. This example of 2 phase material is also used in next section. To compare the sample image with reconstructed image, three global feature vectors were extracted from the input microstructure.

1. Heyn's intercept histogram [43, 42] is employed for assessing the grain sizes. Histograms of the intercept length distribution (mean intercept length versus number of test lines possessing the mean intercept length) is used as the feature vector.

2. Rose of intersections is used as the feature vector for assessing grain shapes. To obtain the rose of intersections, a network of parallel equidistant lines is placed over the microstructure image at several angles and the number of grain boundary intersections with each test line is measured. The distribution of intersections with the angle of orientation of the lines is called the rose of intersection.

3. Color histogram and color clouds are used for measuring phase/orientation distribution. The color cloud used here is an attempt at showing the pixels in

'color space' rather than Euclidean space ('microstructure'). Color densities are converted into scattered random dots around the spatial position assigned to the color, with the extent of the spatial position determined by the frequency with which that RGB triplet appears in the image.

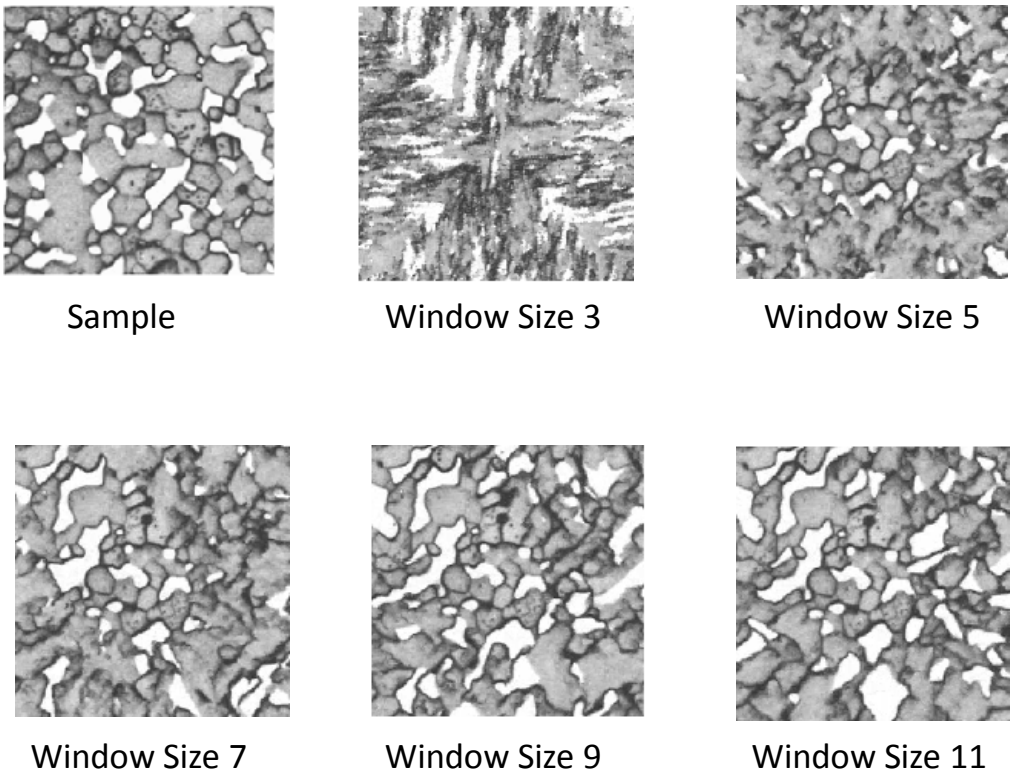

Figure 2.3: *Effect of Window size, none of the image looks similar to sample image but image generated with window size of 11 has statistical correlation function very much similar to that of sample image.*

These features were compared with similar features from a few snapshots (with the same size as the input image) extracted from the reconstructed microstructure. Our preliminary results for case (1) (Fig. 2.5) look quite impressive. The MRF model is not only able to reconstruct the local features such as grain boundaries and connectivities, the global feature vectors (intercept histogram and rose of intersections) compare favorably with the input image.

In the second example, microstructure of the Aluminum alloy AA3002 measured using polarised light microscopy (Ref. [142]) was used. The microstructure represents

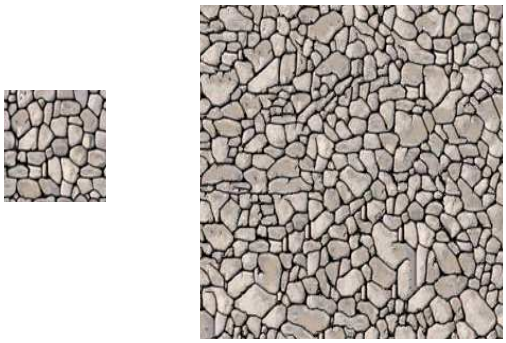

Figure 2.4: *Initial microstructure (left) and the synthesized microstructure (right) from our Markov random field code. Note that local features such as grain boundaries are effectively captured.*

the rolling plane and reveals a fully recrystallised grain structure with randomly distributed intermetallic phases (dark spots in the image). The microstructure is colored based on the occurrence of near-cube and non-cube orientations. This analysis is based on observed contrast effects when the object is rotated relative to the polarised light directions. Purple regions are cube or near-cube orientations, whereas the yellow/red regions are non-cube. The Markov random field reconstruction and the original microstructure are indicated in Fig. 2.6. The microstructure was reconstructed using a 150×170 pixel input image shown in Fig 2.6(left). The preliminary reconstruction shown here only uses the RGB data for reconstruction. The fraction of cube versus non-cube orientations and distribution of intermetallic phases was studied using color histograms.

The color blot and color histogram results shown in Fig 2.7 show good visual correlation of the reconstructed image with the experimental input image. The texture components (cube versus non–cube orientations) are well reproduced in the larger synthesized image. Comparison of the larger experimental image present a more rigorous test of correctness of the MRF approach. It is seen that the large scale texture is faithfully captured.However,the intermetallic phases (eg. black spots) appear more correlated (thinly spread out) in the experimental image as well as the input image.

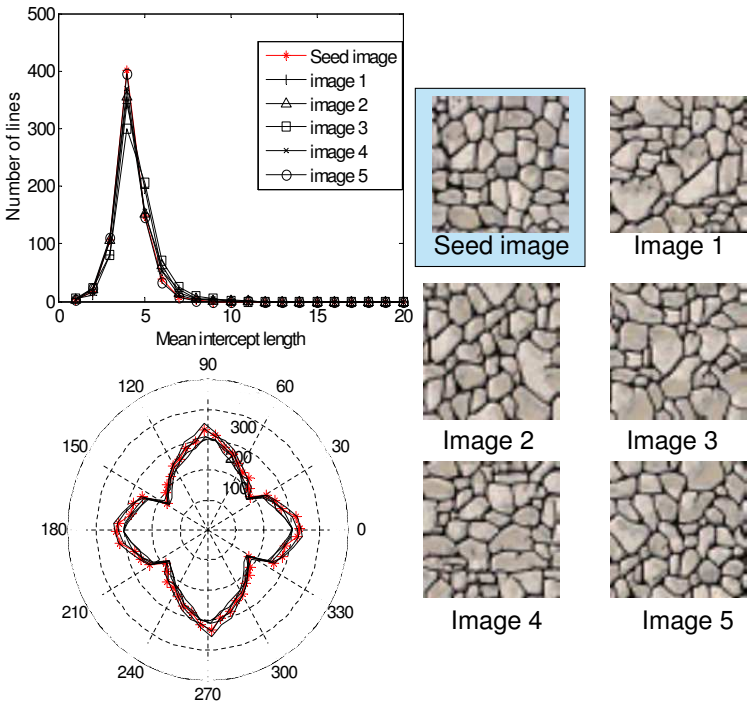

Figure 2.5: *Statistics of synthesized images are compared with the seed image. The mean intercept length and rose of intersections are shown. Note that none of the synthesized images are identical to the seed image, yet global statistics of the seed image are well captured.*

Such fine features can be better captured using a feature mapping MRF approach described before, where weights are assigned to an additional feature channel (in addition to the original RGB channel). Further, if feature mapping were utilized, a better resolution of grain boundaries could have been obtained in the synthesized image.

2.2.1 Comparison of moment invariants

Moment Invariants(MIs) are techniques to quantify the differences between two microstructure or in our case the images. MIs are generally non-linear combinations of (typically second order) moment of an object that are selected in such a way that they are invariant with respect to a class of coordinate transformations. The MIs of a set of a similar objects can be plotted as a distribution, and different object shapes generate different distribution. MIs were first used for automated identification of character

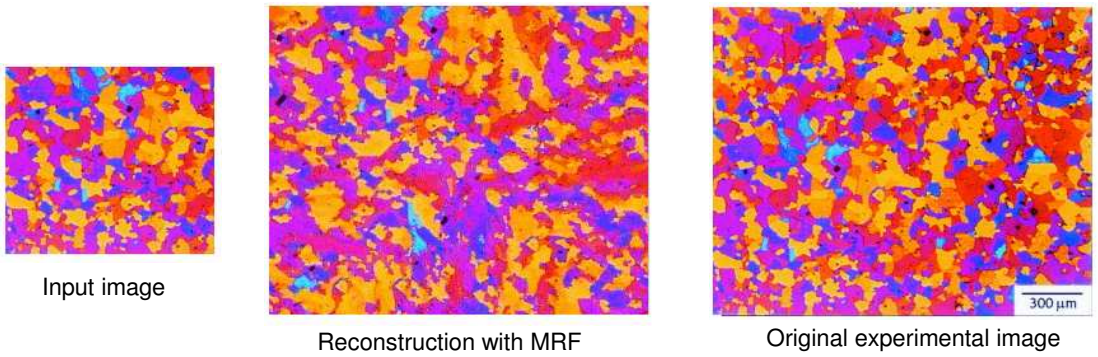

Figure 2.6: *Reconstruction of an experimentally measured AA3002 Aluminum alloy microstructure [142] using Markov random Field algorithm. The larger microstructure from which the input image is taken is also shown for comparison. Purple regions are cube/near cube grain orientations, yellow/red regions are non-cube orientations. The fine dark spots are the intermetallic phases.*

by Hu[57], and have since seen many applications in a variety of field including the material field [86]. The MIs can be expressed in a normalized(dimensionless) form by approximate scaling with respect to the object surface area, the researchers [30] have identified 2 MI's (ω_1, ω_2 of second order, details about the normalization factor and their values for various possible 2D shapes are given in [30]. Graphical representation for these 2 second order moment invariant as x-y coordinate in a plot is known as Second Order Moment Invariant map (SOMIM). SOMIM can be used for providing shape information while shape complexity is contained in higher order moments. In the generalized higher dimensional space of higher order moments, we can represent the coordinate of the morphology as $\xi = (x_1, x_2 ..... , x_N)$ where N is the number of MIs used in the description. This can be projected onto the diagonal line in this N-dimensional space by forming the dot product with the unit vector $\hat{u} = (1,1....1)/\sqrt{N}$; the result is a point on the diagonal line at a (signed) distance $d_u(x) = (\sum_{i=1}^{N} x_i)/N$ from the origin. In other words, distance along the diagonal is equal to the average of the vector components $d_u(x) = \langle x_i \rangle$. Projecting all the MIs of a given order onto a single line has the advantage that MIs of second through fourth order can be represented graphically in a single 3D diagram. We will refer to such diagrams as projected

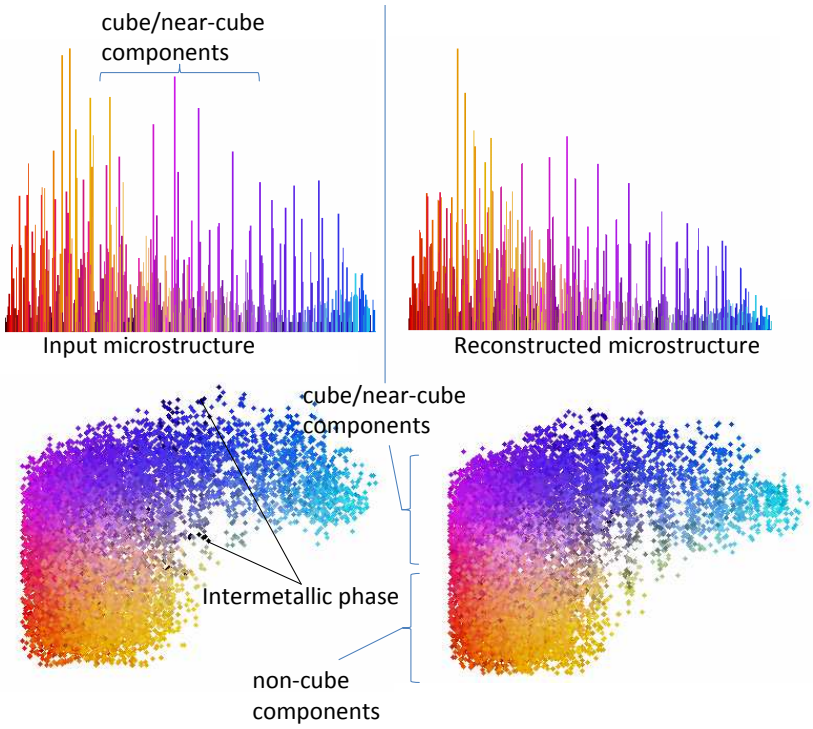

Figure 2.7: *Color histograms of the input microstructure and reconstructed microstructure are compared. A novel color blot method is used to compare the distribution of cube/near cube regions, and intermetallic phases in the input and synthesized images.*

moment invariant maps(PMIM). Details about the PMIM for various shapes is given in this paper[30]. To make a comparison of synthesized with original image we used combination of second and fourth order moments in a 2D PMIM. The x axis for this map is the average of 2nd order moment invariant while y axis is average of 4th order moment invariant. Using SOMIM and PMIM we can generate density maps to show distribution of shapes throughout an image. For 1D distribution of data second order moment is analogous to standard deviation while the 4th order moment invariant is similar to kurtosis. The density maps for SOMIM and PMIM is shown in Fig.2.8 and Fig.2.9 respectively. These density maps are for image shown in 2.4.

To compare the density maps obtained by reconstructed image to that of original image we need to introduce an appropriate similarity metric. The modified Bhattacharya coefficient H(p,q) also known as Hellinger distance, was found to provide a

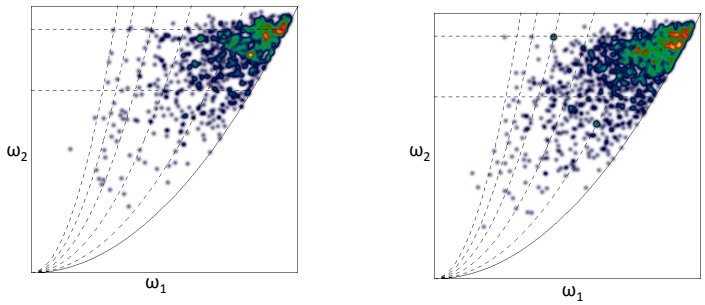

Figure 2.8: *SOMIM density map original(left) and synthetic(right)*

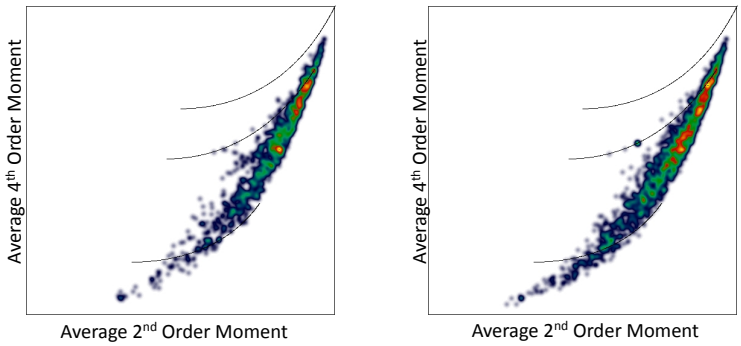

Figure 2.9: *PMIM density map original(left) and synthetic(right)*

good balance between ease of use, speed of computation and ability to distinguish between two different density maps p and q. The regular Bhattacharya coefficient $\beta(p,q)$ is a measure of the similarity between two normalized distributions and can be written in discrete form as [24][6]

$$\beta(p,q) = \sum_{i=1}^{N} \sqrt{p(i)q(i)}, \left(with \sum_{i=1}^{N} p(i) = \sum_{i=1}^{N} q(i) = 1 \right) \tag{2.1}$$

where the summation run over all of the N bins of the SOMIM or PMIM density maps. The larger the value of β, the more similar the two distributions are. The Hellinger distance H(p,q) is defined by [35] as

$$H(p,q) = \sqrt{1 - \beta(p,q)} \tag{2.2}$$

Value of H for SOMIM is 0.47 and that of PMIM is 0.37. These values for H indicate that we can able to reconstruct the synthetic image from our original image using MRF synthesis approach.

2.2.2 Comparison of microstructure sensitive properties

In this section we have calculated and compared effective properties for sample and reconstructed image. We have performed finite element analysis to compare the stress distributions in the original and synthesized image.

2.2.2.1 Example 1. Tungsten Silver Composite Image

In Fig2.3, the sample image from Ref. [135] is presented. Assuming isotropic nature of the microstructure, rotationally invariant probability functions are employed as the microstructural feature to compare the sample image with the reconstructed one. Rotationally invariant N-point correlation measure S_N^i can be interpreted as the probability of finding the N vertices of a polyhedron separated by relative distances x_1, x_2,. . .,x_N. The simplest of these probability functions is the one-point function, S_1^i, which is just the volume fraction (V) of phase i. The two-point correlation measure, S_2^i, can be obtained by randomly placing line segments of length r within the microstructure and counting the fraction of times the end points fall in phase i. All the required correlation measures for classification are obtained using a Monte-Carlo sampling procedure. The procedure involves initially selecting a large number of initial points in the microstructure. For every initial point, several end points at various distances are randomly sampled and the number of successes (of all points falling in the ith phase) are counted to obtain the required correlation measures.

Statistical measures up to the third-order were extracted from the microstructures by sampling 15,000 initial points. A 303X303 pixel region of the microstructure was converted to a black and white image for distinguishing the two phases. The rotation-

ally invariant two- and three-point correlation measures of the experimental image were then extracted using Monte-Carlo sampling techniques.Classification is based on two sets of descriptors, the autocorrelation function $\gamma(r) = \frac{S_2(r)-p^2}{p-p^2}$ and three-point measure $S_3(r,s,t)$.The statistical correlation measures of the reconstructed microstructure and the sample image are compared in Fig. 2.10.The three-point probability measure S3(r,s,t) is depicted in a feature vector format with the distances (r,s,t)μm indicated for key points in Fig.2.10(b). Object oriented finite element software developed by NIST (OOF2)[105][106] allows computation of the mechanical properties directly from the microstructure. To obtain the stress contour under a uniaxial tension(3.3% strain in y direction) we first created a binary image using ImageJ software. The binary image is then imported in OOF2 and mesh is created. For tungsten, we have used an Young's Modulus value of 411 GPa and a Poisson's ratio of 0.28, corresponding values for the silver phase is 83 GPa and 0.37. Using these elastic properties, we obtained the stress contour plot as shown in Fig 2.11 (a) and (b) for sample and reconstructed image respectively. The color histogram for stress contour plot are shown in part c and d of same figure. Color histogram of the stresses in the synthesized image matches closely to that of sample one. Average stress value for synthesized image comes out to be 9.62 GPa the corresponding value for sample image is 9.85 GPa. Using this stress value we have calculated effective Young Modulus(Y) for synthesized and sample as 288.61 GPa and 295.58 GPa respectively. This value for Young Modulus is very close to what is obtained by experiments Ref [135]. The variation of Y for original, synthesized with temperature is shown in Fig2.12, in the same plot, we also plot the value of Y at different temperatures as obtained by experiments.

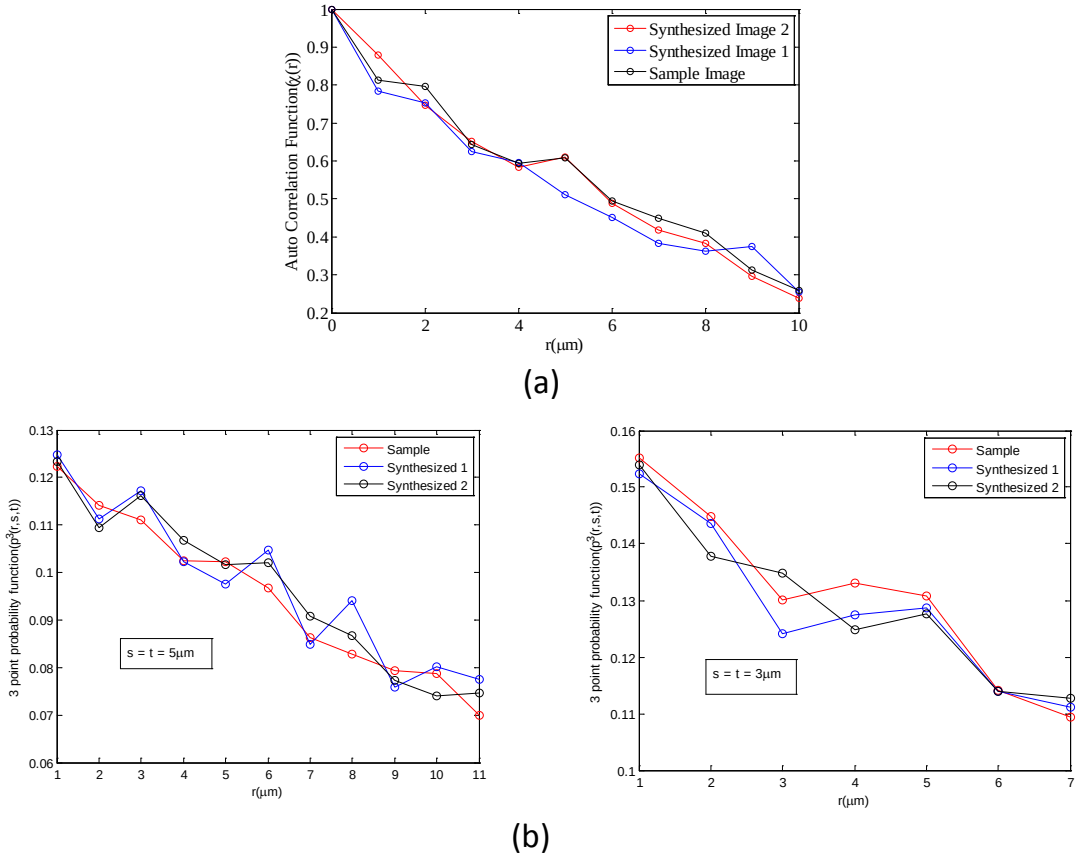

Figure 2.10: *Comparison of the sample image statistical features with the features of the reconstructed image shown in Fig.2.3. (a) The autocorrelation function and (b) the three-point probability function S3(r,s,t) shown for s=t=5(long range correlation) and s=t=3(short range correlation)*

2.2.3 Example 2. Aluminum alloy AA3002 representing the rolling plane

We performed finite element calculations on synthesized and sample image in Fig 2.6 and compared the Young's Modulus with angle of rotation for sample and synthesized image. To measure the statistically similarity between sample and synthesized image, we also calculated the orientation distribution function(ODF) by assigning a unique orientation to each pixel based on its color. In Fig 2.14 we have shown ODF for sample and two synthesized images and we observed that ODF for synthesized images is very close to that of sample image. This result clearly proves that reconstructed microstructure is very similar to the sample microstructure. In Fig

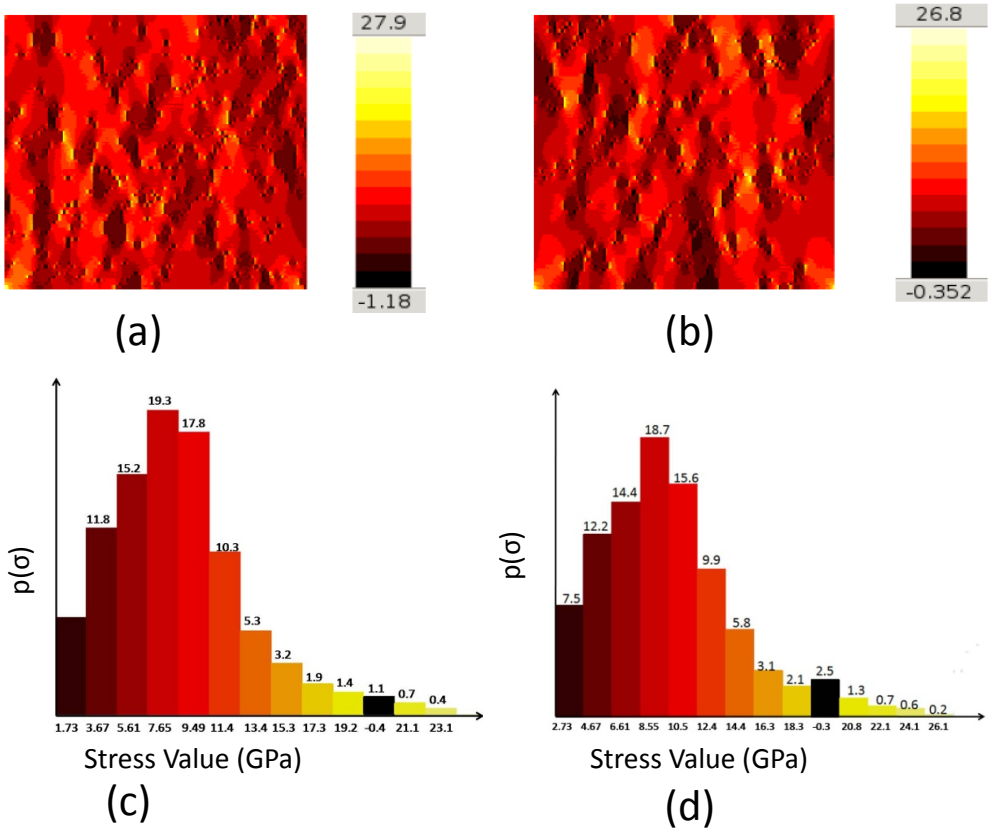

Figure 2.11: *Comparison of the distribution of the normal stress σ_y in GPa for (a)sample image (b) Synthesized image (c)Color histogram of stress contour for sample image (d) Color histogram of stress contour for synthesized image*

2.13(b) we have plotted the variation of Young's Modulus (E) with rotation angle of the crystal present in the material. We got a similar variation of E for sample and synthesized images. A crystal plasticity simulation (from our recent work[32]) was performed at a constant strain rate of 6.667e-4 s^{-1} and a temperature of 300K. The numerical experiment simulated a simple shear motion. In Fig 2.13(a) we have plotted the equivalent stress-strain response for sample and synthesized image. Contour plot with color histogram of stresses shown in Fig.2.15 reveal that the response of the synthesized image is very similar to that of sample.

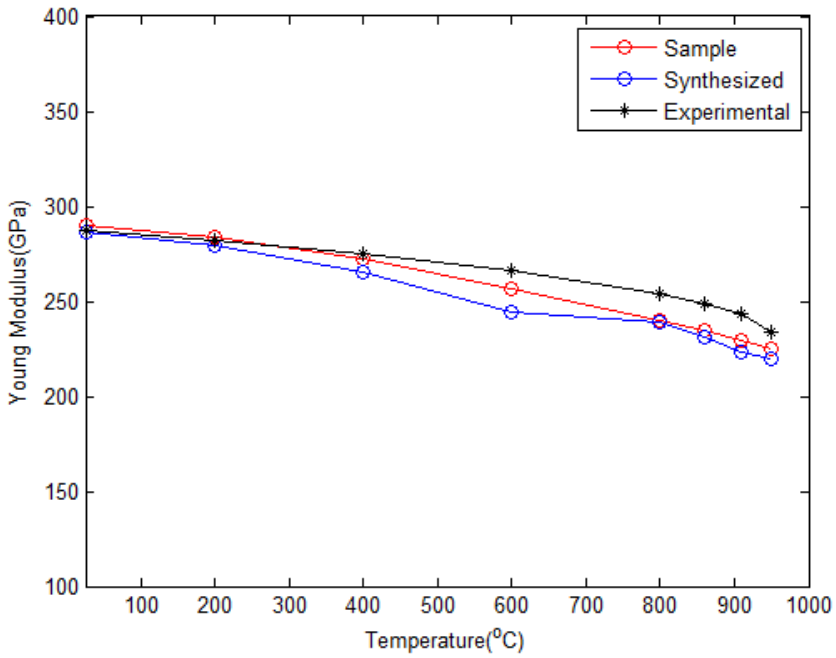

Figure 2.12: *Variation of Young Modulus with temperature for sample and synthesized image also that obtained in experiment*

2.3 Algorithm for reconstruction of 3D microstructures

Another problem of interest is the reconstruction of 3D microstructures from three orthogonal 2D sectional images taken along the x-, y- and z- planes. The information contained in these three 2D micrographs is in the form of pixels containing colors corresponding to different constituent phases. The outcome of the inverse problem is a 3D microstructure containing voxels colored consistently such that any arbitrary x-, y- or z- slice 'looks' similar to the corresponding input micrographs. This reconstruction problem leads to anisotropic microstructures, which is in contrast to other such works in literature that use a single reference (2D) image and make assumptions of microstructural isotropy, i.e. slices in every direction look similar to a single input image [127]. The approach proposed here involves maximizing the similarity between the solid microstructure and the 2D sectional microstructures by minimizing a neighborhood cost function. This cost function ensures that the local neighborhood on 2D slices taken along the x-,y- or z- directions through the 3D microstructure is similar

to some neighborhood in the 2D micrograph imaged along that plane.

In the following discussion, let $\boldsymbol{S}^x, \boldsymbol{S}^y$ and $\boldsymbol{S}^z$ denote the set of orthogonal (x, y and z, respectively) slices of the microstructure. Let $\boldsymbol{V}$ denote the solid (3D) microstructure. The color of voxel v in the 3D microstructure is denoted by $\boldsymbol{V}_v$. In addition to the color (eg. RGB triplet), the vector $\boldsymbol{V}_v$ may also contain other values including grain orientation and phase index. In this work, the color is represented using G color levels in the range $\{0, 1, .., G-1\}$ each of which maps to an RGB triplet. The number of color levels is chosen based on the microstructure to be reconstructed, eg. for binary images $G = 2$.

Recall our Markovian assumption that the probability distribution of the color for a pixel given the colors of its spatial neighborhood is independent of the rest of image. The vectors denoting the spatial neighborhood of voxel v in the slices orthogonal to the x, y, and z axis, respectively, are denoted as $\boldsymbol{V}_v^x, \boldsymbol{V}_v^y$, and $\boldsymbol{V}_v^z$ (see Fig. 2.16). The neighborhood is taken over a small user-assigned window around the voxel v. Let $\boldsymbol{S}^{x,w}, \boldsymbol{S}^{y,w}$, and $\boldsymbol{S}^{z,w}$ denote a window of the same size in the input 2D micrographs. In order to find the coloring of voxel v based on the neighbor voxels in the x–plane, one needs to compute the conditional probability density $p(\boldsymbol{V}_v|\text{color of x–plane neighbors of } v)$. Explicit construction of such a probability density is often computationally intractable. Instead, the most likely value of v is identified by first finding a window $\boldsymbol{S}^{x,w}$ that is most similar to $\boldsymbol{V}_v^x$ in the input 2D micrograph. This window is denoted by $\boldsymbol{S}_v^x$ (see Fig. 2.16). Similarly, matching windows to the y– and z– plane neighborhoods of voxel v in the corresponding 2D sectional image (denoted as $\boldsymbol{S}_v^y, \boldsymbol{S}_v^z$ are found. Each of these matching windows $\boldsymbol{S}_v^x, \boldsymbol{S}_v^y, \boldsymbol{S}_v^z$ may have different coloring of the center pixel. Thus, we need an optimization methodology to effectively merge these disparate values and identify a unique coloring for voxel v. The optimization approach is described next.

Let the value $\boldsymbol{V}_{v,u}^x$ denotes the color of voxel u in the neighborhood $\boldsymbol{V}_v^x$. Similarly,

the value $\boldsymbol{S}^x_{v,u}$ and $\boldsymbol{S}^{x,w}_u$, respectively, denote the color of pixel u in the window $\boldsymbol{S}^x_v$ and $\boldsymbol{S}^{x,w}$. The 3D microstructure is synthesized by posing the problem as a L^2 minimization of the energy [69]:

$$E(\boldsymbol{V}) = \sum_{i\in\{x,y,z\}} \sum_v \sum_u \omega^i_{v,u} \|\boldsymbol{V}^i_{v,u} - \boldsymbol{S}^i_{v,u}\|^2 \tag{2.3}$$

Here, $\omega^i_{v,u}$ denotes a per pixel weight. In order to preserve the short range correlations of the microstructure as much as possible, the weight for nearby pixel is taken to be greater than pixels farther away (Gaussian weighting is used).

The optimization is carried out in two steps. In the first step, the energy is minimized with respect to $\boldsymbol{S}^i_v$. In this step, we assume that the most likely sample from the conditional probability distribution of the center pixel in the 3D image (eg. $p(\boldsymbol{V}_v|$colors of x–plane neighbors of $v)$) is the center pixel of a best matching window in an experimentally obtained 2D slice on the corresponding plane. The best matching neighborhood of voxel v along the x–plane is selected by solving the following problem:

$$\boldsymbol{S}^x_v = \arg \min_{\boldsymbol{S}^{x,w}} \sum_u \omega^x_{v,u} \|\boldsymbol{V}^x_{v,u} - \boldsymbol{S}^{x,w}_u\|^2 \tag{2.4}$$

This is an exhaustive search that compares all the windows in the input 2D micrograph to the corresponding x–slice neighborhood of voxel v and identifies a window that leads to a minimum weighted squared distance. In this process, for 2D images of size 64×64 with a 16×16 neighborhood window, a matrix of size $16^2 \times (64-16)^2$ is built containing all possible neighborhoods of pixels that have a complete 16^2 window around it. The column in this matrix that has a minimum distance to the 3D slice $\boldsymbol{V}^x_v$ is then found through a k–nearest neighbor algorithm [8]. Note that, we are only given a limited (in this work, a single) 2D experimental sample along each cross–section, which means that the best match may not be an exact match for $\boldsymbol{V}^x_v$.

Thus, for each voxel v, a set of three best matching neighborhoods are obtained,

possibly with different colors corresponding to the center pixel. A unique value of v thus needs to be found by weighting colors pertaining to location v in not only the matching windows of voxel v but also its neighbors. This is exactly done in the second step of the optimization procedure, where the optimal color of voxel v is computed by setting the derivative of the energy function with respect to $\boldsymbol{V}_v$ to zero. This leads to a simple weighted average expression for the color of voxel v:

$$\boldsymbol{V}_v = (\sum_{i\in\{x,y,z\}} \sum_u \omega^i_{u,v} \boldsymbol{S}^i_{u,v}) / (\sum_{i\in\{x,y,z\}} \sum_u \omega^i_{u,v}) \tag{2.5}$$

Note that the subscripts u and v are switched in the above expression as compared to Eq. 2.3. This implies that the optimal color of the voxel v is the weighted average of the colors at locations corresponding to voxel v in the best matching windows ($\boldsymbol{S}^i_u$) of voxels (u) in the solid microstructure. Since $\boldsymbol{V}_v$ changes after this step, the set of closest input neighborhoods $\boldsymbol{S}^i_v$ will also change. Hence, these two steps were repeated until convergence, i.e., until the set $\boldsymbol{S}^i_v$ stops changing. As a starting condition, a random color from the input 2D images is assigned to each voxel v. The process is carried out in a multiresolution (or multigrid) fashion [64]: starting with a coarse voxel mesh and interpolating the results to a finer mesh once the coarser 3D image has converged to a local minimum. Three resolution levels ($16^3, 32^3$ and 64^3) were used. Synthesizing a 64^3 solid microstructure took between 10–15 minutes on a 3 GHz desktop computer, with about two–thirds of the time spend in step 1 (search) algorithm.

2.4 Results

The approach has been demonstrated for three test cases with 2D images corresponding to:

1. Case 1. An isotropic distribution of solid circles;

2. Case 2. An anisotropic case with solid circles in the z-slice (similar to case (i)) but an interconnected lamellar structure in the x- and y- slices;

3. Case 3. A polycrystalline microstructure.

In case 1, all three slices (x-,y- and z-) were assigned to the same 2D image depicted in Fig. 2.17(a). The resulting 3D microstructure is expected to be a random distribution of spheres. The 3D microstructure obtained by our approach is shown in Fig. 2.17(b). The internal structure of the solid microstructure is shown via slices in the x–plane at different distances from the origin. Various slices 'look' similar to the input image as expected from the Markov Random field assumption. Case 2 builds upon this case by introducing anisotropy in the x- and y- planes. Three 2D images corresponding to x–,y– and z– slices (as shown in Fig. 2.18(a)) were used in the reconstruction. An interconnected lamellar structure was used in the x- and z-planes while the z–plane image allowed merging of the solid circles to allow for a more complex microstructure. In the algorithm, we match the 2D images with all three orthogonal slices through every voxel. The resulting anisotropic 3D microstructure shown in Fig. 2.18(b) is quite complex. The y–axis slices as shown in Fig. 2.18(c) show the depth profile of various solid circles seen at the top surface, with intricate internal structure revealed.

In the last example, a polycrystalline microstructure was employed to show the applicability of the algorithm to cases beyond two-phase media. The microstructure is equiaxed and all three slices were assigned to the same 2D image shown in Fig. 2.19(a). The resulting 3D microstructure is shown in Fig. 2.19(b) and its internal structure revealed through x–axis slices in Fig. 2.19(c). The results show that the grains built by the algorithm are also equiaxed with a variety of 3D shapes identified by the algorithm. However, some of grain boundaries do not show up well in the slices which is primarily attributed to the lower resolution of the 3D image (64^3) compared to the original input image.

2.4.1 Validation tests

For testing the validity of the 3D reconstructions, quantitative comparisons were made between the original 2D image and the reconstructed image, through comparison of the statistical correlation functions as described in Ref. [145]. The statistical features of the 2D distribution of solid circles from Fig. 2.17 and its 3D reconstruction were compared. The original 2D image was a square of side $64\mu m$ and had a phase 1 (white phase) volume fraction of 70%. The comparison of two point probability ($S_{(2)}$) and the three point probability function $S_{(3)}$ are shown in Fig. 2.20(a) and Fig. 2.20(b), respectively. The three-point probability measure $S_{(3)}(r, s, t)$ is depicted in a feature vector format with the distances $(r, s, t)\mu m$ indicated for key points in Fig. 2.20(b). The first points in both graphs (Fig. 2.20) show the volume fraction of white phase for 2D image as well as the reconstructed image. The decay in the two point correlation function is identical for the reconstructed image up until $3\mu m$, showing excellent reproduction of the short–range correlation. The same aspect can also be seen from comparing the short range correlation in the three–point probability function (Fig. 2.20(b)). Although the longer range correlations match qualitatively, there is a drift seen as the distance between pixels increases. Both the excellent match in short range correlation and the small drift in the long range correlation can be explained based on the reconstruction algorithm, which models a stronger interaction of a center pixel to pixels in its immediate local neighborhood than pixels farther away. In effect, the algorithm gives a stronger weighting towards matching the short range correlations in the microstructure.

2.4.2 Elastic properties of two phase composite

The experimental image of the tungsten silver composite in Ref [135] was used to reconstruct a 3D microstructure. An instance of the reconstructed microstructure is shown in Fig. 2.21(b,c) with the distribution of each phase shown separately. The

auto-correlation function for the silver phase $\gamma(r) = \frac{S^1_{(2)}(r)-p^2}{p-p^2}$ of the reconstructed 3D microstructure and the experimental image are compared in Fig. 2.22(a) showing excellent match of short range correlations with a small difference seen in longer range correlations. Short range correlations carry the greatest weightage in determining mechanical properties such as elastic modulus (eg. [108]), although long range correlations have been found to be important for phenomena such as surface roughening during plastic deformation [75]. To test if the elastic properties are well captured in the reconstructed 3D microstructure, we compared against the experimental data from Ref. [135] of the elastic modulus as a function of temperature. The elastic properties of individual components at different temperatures are available from Ref. [107] and are listed in Table. 1. The data was used within a finite element simulation to compute the elastic modulus of the reconstructed microstructure using the method described in Ref. [46]. The computed properties of the reconstructed 3D microstructure closely follow the experimentally measured Young's modulus from Ref. [135] as shown in Fig. 2.22(b) with an average error from experimental data of about 5 %.

Table 2.1: Elastic properties of silver and tungsten phases as a function of temperature (from Ref. [107])

$T(^oC)$	E_{silver} (GPa)	ν_{silver}	$E_{tungsten}$ (GPa)	$\nu_{tungsten}$
25	71	0.36	400	0.28
200	69	0.36	392	0.28
400	63	0.36	383	0.28
600	54	0.36	373	0.28
800	45	0.37	363	0.28
860	42	0.37	361	0.28
910	39	0.37	359	0.28
950	37	0.37	357	0.28

2.5 Conclusions and Summary

A Markov Random Field approach for reconstructing diverse microstructure from two–dimensional microstructures is presented. Given a small input microstructure, these algorithms can reconstruct larger microstructures pixel-by-pixel using patten matching algorithms. The algorithm can also reconstruct 3D images through matching of 2D slices at different voxels to the representative 2D micrographs. The method is particularly promising for anisotropic cases where the x–,y– and z– slices look different. We performed rigorous testing of the stereological features (eg. grain size histograms) and other engineering properties (elastic properties, stress distribution) of reconstructed microstructures. The results demonstrate that the method can effectively model statistical features in the microstructure. The approach can be useful to rapidly build a library of 3D microstructures for modeling purposes from 2D micrographs.

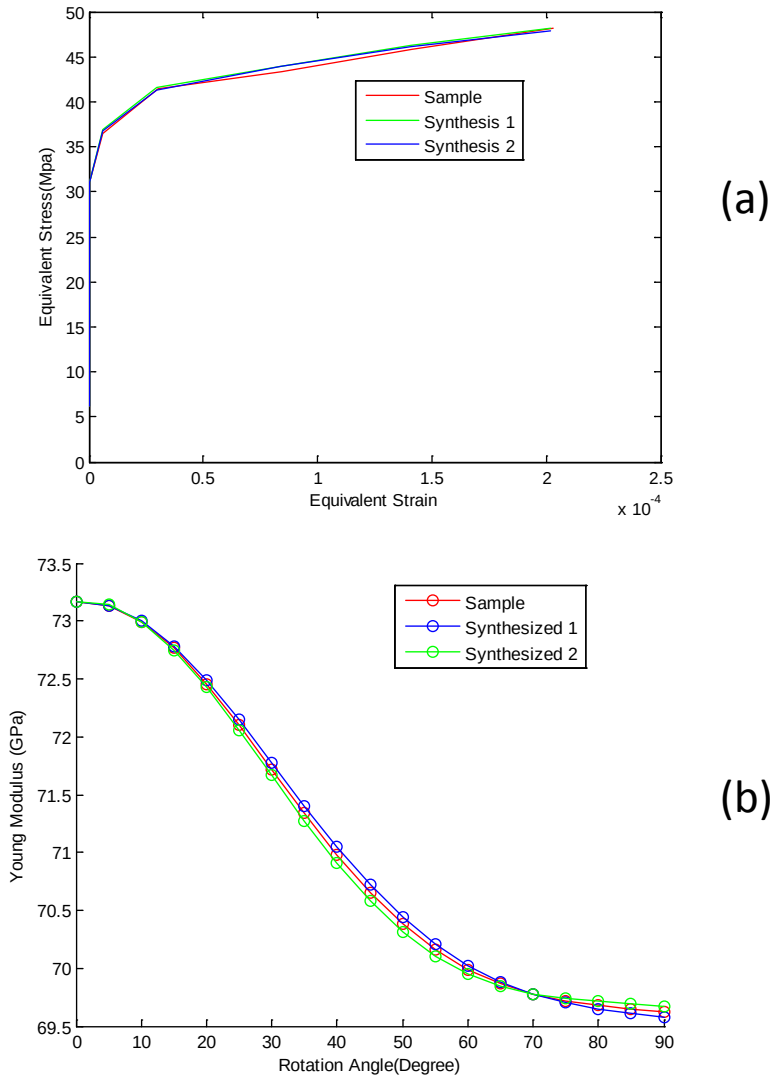

Figure 2.13: *(a) Comparison of the equivalent stress-strain curve predicted through homogenization with Taylor Simulation for Sample and two Synthesized image (b) Variation of Young Modulus with angle of rotation for sample and synthesized image*

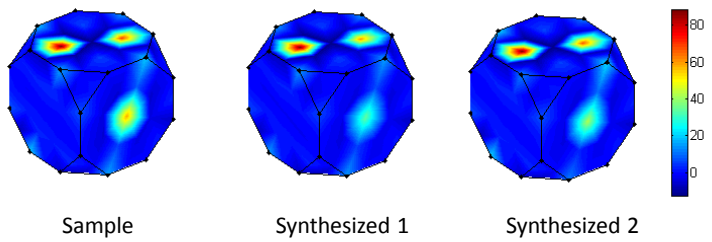

Figure 2.14: *ODF Plot for sample and synthesized image for rolling case*

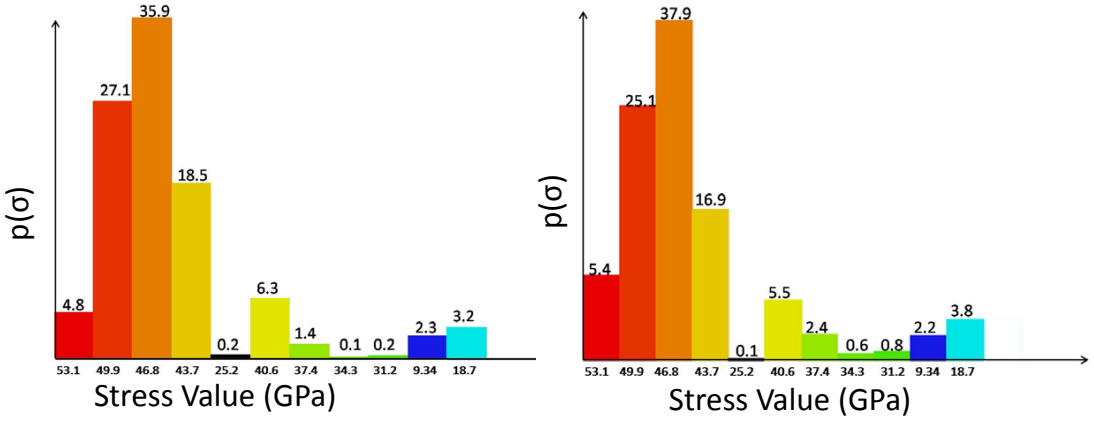

Figure 2.15: *Comparison of the distribution of the equivalent stress with color histogram*

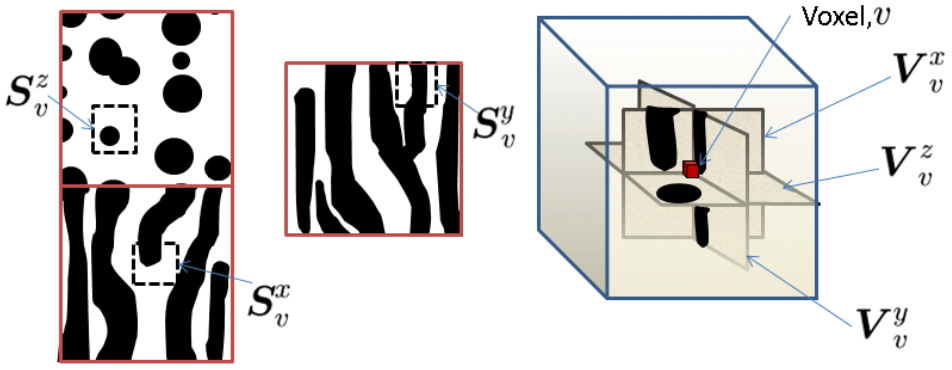

Figure 2.16: *The neighborhoods of v in the slices orthogonal to the x, y, and z axis, respectively, are shown. The windows in the input 2D micrograph shown in dotted lines are denoted by $\boldsymbol{S}_v^i$ $(i = x, y, z)$. These windows closely resemble the neighborhoods of v.*

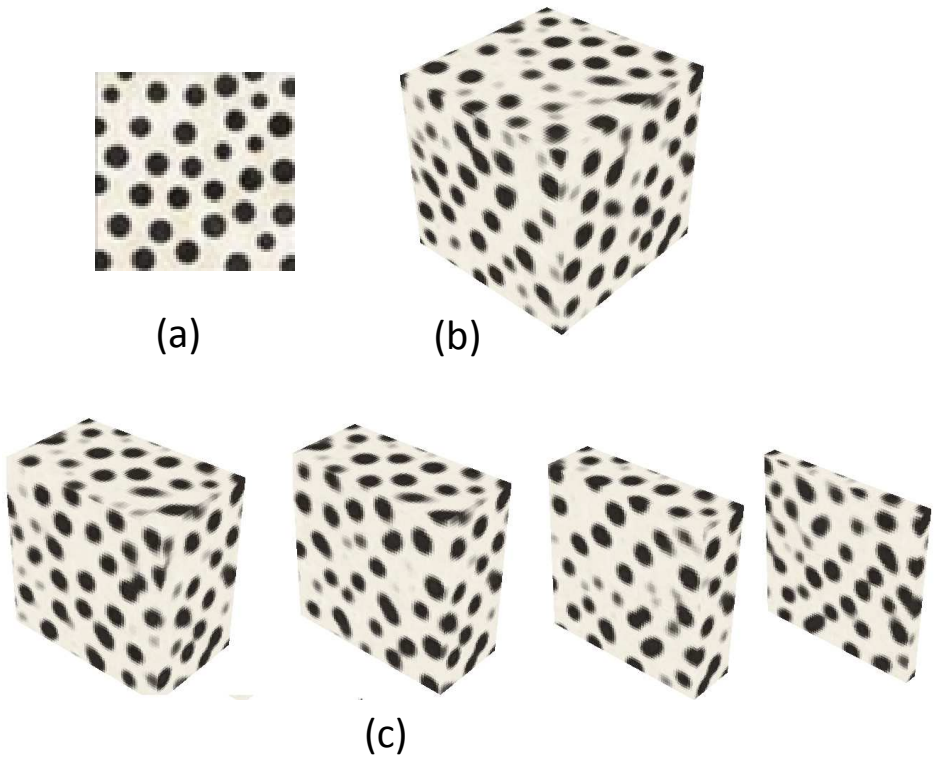

Figure 2.17: *a. Input 2D microstructure showing an isotropic distribution of solid circles. b. 3D reconstruction c. 3D sectional images of the reconstructed microstructure.*

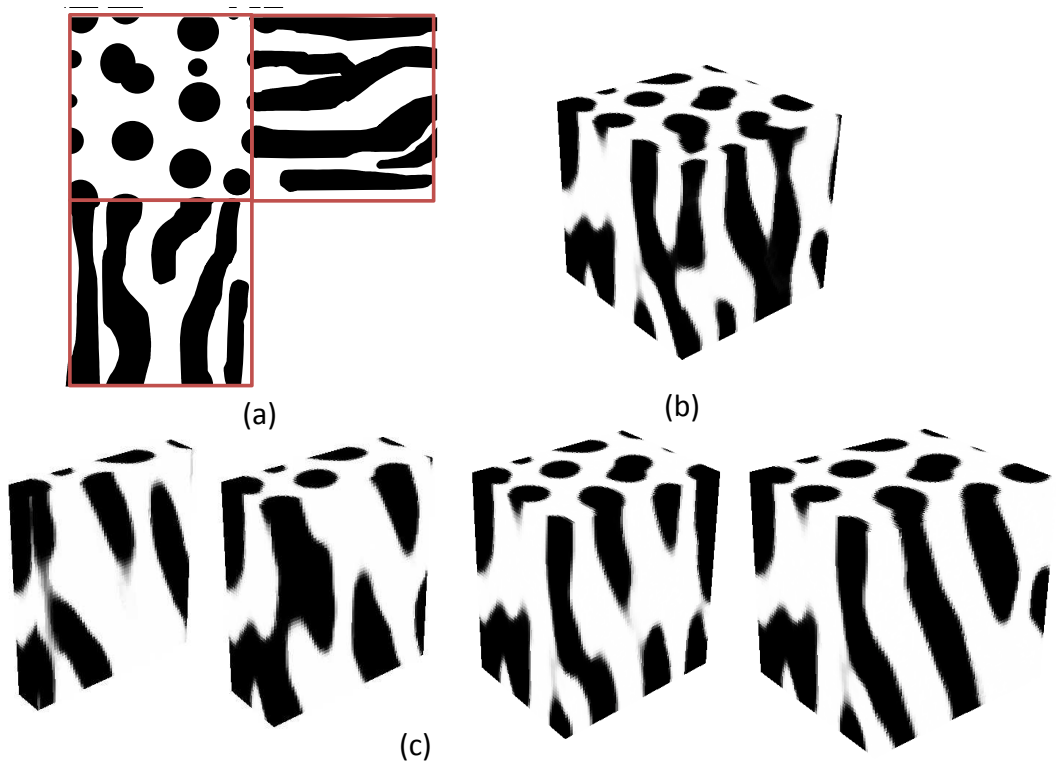

Figure 2.18: *a. An anisotropic case with solid circles in the z-slice (similar to case (i)) but an interconnected lamellar structure in the x- and y- slices. b. 3D reconstruction c. 3D sectional images of the reconstructed microstructure.*

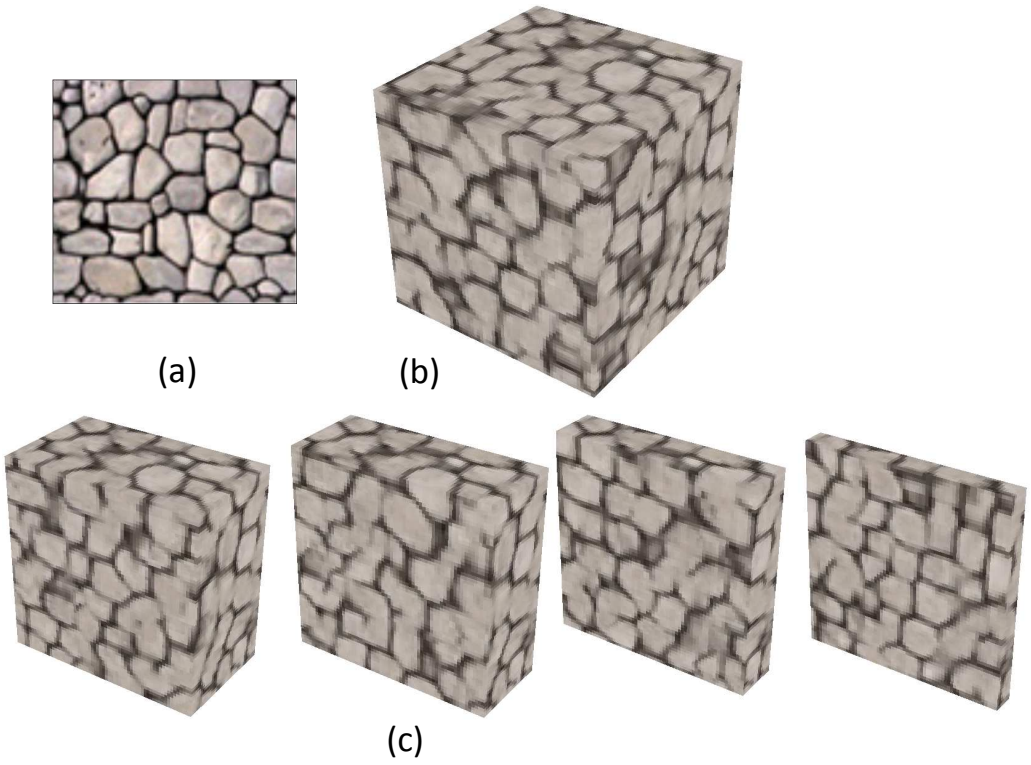

Figure 2.19: *a. An experimental 2D polycrystalline microstructure. b. 3D reconstruction c. 3D sectional images of the reconstructed microstructure.*

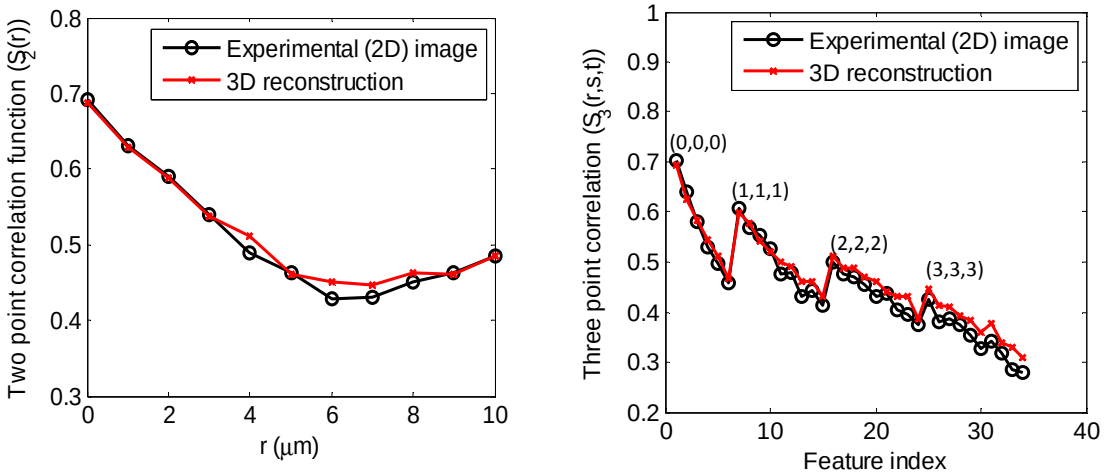

Figure 2.20: *Comparison of the features of the 2D and reconstructed image shown in Fig. 2.16. (a) Two point probability function. (b) Three point probability function*

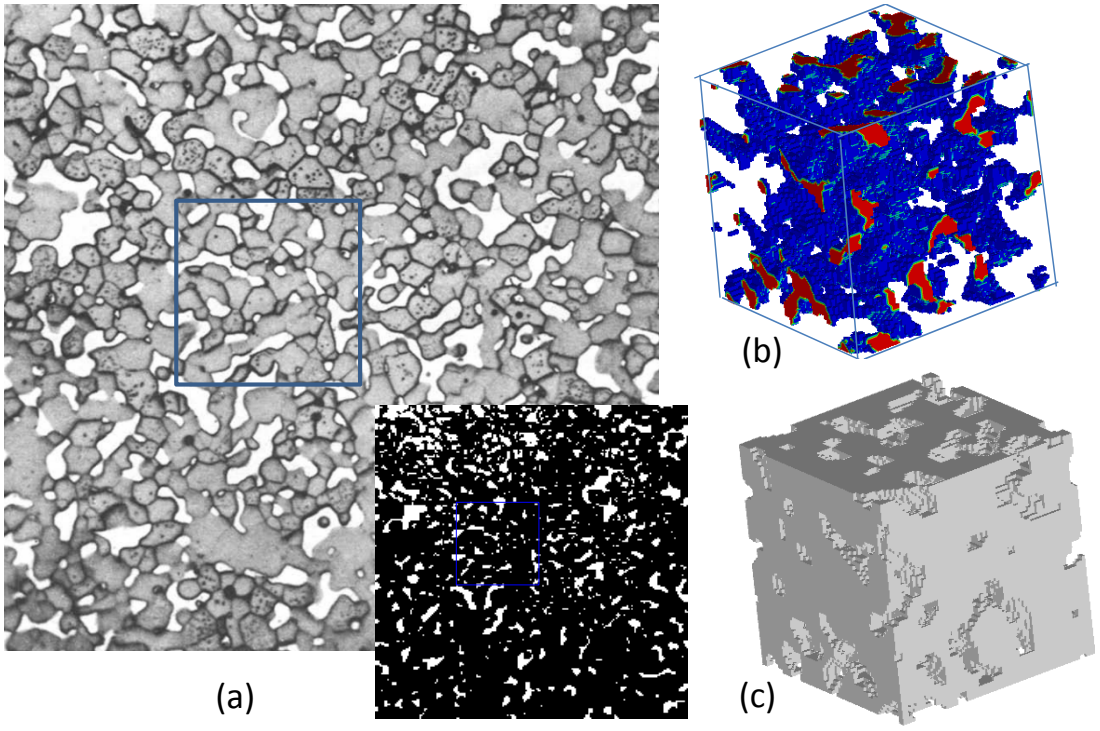

Figure 2.21: *Experimental Tungsten-silver composite image (204 × 236μm) from Umekawa et al. [135]. The black and white image corresponds to a thresholded image with white representing the silver phase and black representing Tungsten. A 64 μm square cell shown in inset was used to reconstruct the 3D image. (b) A 64 μm length cell of reconstructed 3D microstructure of the experimental image showing silver distribution (c) The tungsten phase of the reconstructed microstructure.*

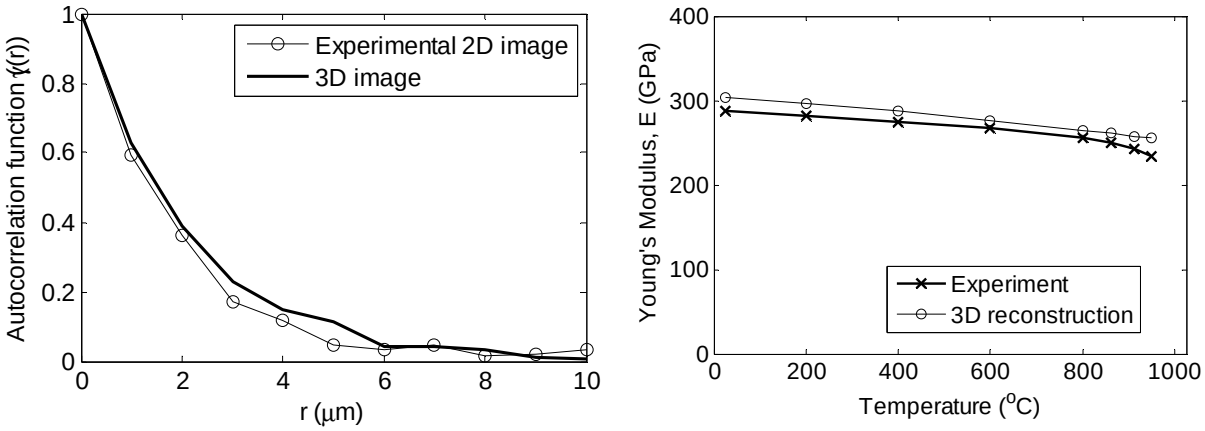

Figure 2.22: *Comparison of properties of 3D reconstruction of Silver-Tungsten composite (a) The autocorrelation function for the silver phase (b) Experimental Young's modulus is shown along with the FEM results for the reconstructed 3D microstructure.*

CHAPTER III

Microstructural modeling of BCC Galfenol

When a magnetic field is applied to Galfenol single crystal, the boundaries between the magnetic domains shift and rotate, both of which cause a change in the material's dimensions. This behavior, termed magnetostriction, has been successfully to transduce magnetic field to mechanical force in micro–scale (MEMS) sensors and actuators. While single crystals of Galfenol provide large magnetostriction, their preparation is expensive. It is well known that thermomechanical processes (such as rolling and extrusion) may provide means to develop polycrystalline Galfenol with properties comparable to expensive single crystals [61]. However, it has proved difficult to predict (and thus, control) the large changes in properties such as magnetostriction and yield strength that occur during thermomechanical processing. For example, warm rolled and annealed specimens retain high magnetostriction but are quite brittle; whereas, cold rolled specimens have high yield strength but lose their magnetostriction [31, 16]. Consequently, it is critical to develop predictive models that can be used to optimize thermomechanical processes and control properties in the final product.

Properties of Galfenol can be tailored by controlling the evolution of features of underlying polycrystalline microstructure through controlled plastic deformation. Simulation of microstructure evolution in polycrystals has been well studied in the

past. Many of the related works apply the Taylor-type (e.g. for a review see Kocks et al.[63]) or finite element homogenization [126] methods that link the kinematics of the macro- and microscopic scales. The success of such approaches has allowed efficient computation of the effect of macroscopic parameters (such as forging rates) on the microstructural response. Microstructure-sensitive design methods can then employ these techniques to address inverse/optimization problems such as computation of optimal crystal orientation distributions that lead to desired elasto-plastic properties (Adams et al) and identification of processing paths that lead to optimal microstructures [127]. In order to control properties during processing, it is important to study the effect of meso–scale features (such as texture, misorientation distribution) on the response of these alloys. For example, experimental studies suggest that internal inhomogeneous strains introduced by microstructural changes play an important role in determining the final magnetostriction in Galfenol [52]. In this chapter, we have calibrated a rate-independent elasto-plastic model of BCC Galfenol single crystal for studying the effect of forming processes on the microstructure response. Both loading and unloading processes have been simulated and a finite strain homogenization algorithm has been developed to investigate final microstructural response under coupled magnetic and stress fields.

3.1 Microstructure Evolution Direct Problem

A rate-independent single-crystal plasticity model developed in Kothari and Anand [9] is used to compute the effect of macroscopic strain on the polycrystal. For a material with $\alpha = 1, \ldots, N$ slip systems defined by ortho-normal vector pairs ($\boldsymbol{m}^\alpha$,$\boldsymbol{n}^\alpha$) denoting the slip direction and slip plane normal respectively, the constitutive equations relate the following basic fields: the deformation gradient $\boldsymbol{F}$ which can be decomposed into elastic and plastic parts as $\boldsymbol{F} = \boldsymbol{F}^e\boldsymbol{F}^p$, the Cauchy stress $\boldsymbol{T}$ and the slip resistances $s^\alpha > 0$. In the constitutive equations (intended to characterize small elastic

strains) to be defined below, the Green elastic strain measure $\check{\boldsymbol{E}}^e = \frac{1}{2}\left(\boldsymbol{F}^{eT}\boldsymbol{F}^e - \boldsymbol{I}\right)$ defined on the relaxed configuration (plastically deformed, unstressed configuration) is utilized. The conjugate stress measure is then defined as $\tilde{\boldsymbol{T}} = \det\boldsymbol{F}^e(\boldsymbol{F}^e)^{-1}\boldsymbol{T}(\boldsymbol{F}^e)^{-T}$ where $\boldsymbol{T}$ is the Cauchy stress for the crystal.

The constitutive relation, for stress, is given by $\tilde{\boldsymbol{T}} = \boldsymbol{\mathcal{L}}^e\left[\check{\boldsymbol{E}}^e\right]$ where $\boldsymbol{\mathcal{L}}^e$ is the fourth-order anisotropic elasticity tensor. It is assumed that deformation takes place through dislocation glide and the evolution of the plastic flow is given by

$$\boldsymbol{L}^p = \dot{\boldsymbol{F}}^p(\boldsymbol{F}^p)^{-1} = \sum_\alpha \dot{\gamma}^\alpha \boldsymbol{S}_0^\alpha sign(\tau^\alpha) \tag{3.1}$$

where $\boldsymbol{S}_0^\alpha = \boldsymbol{m}^\alpha \otimes \boldsymbol{n}^\alpha$ is the Schmid tensor and $\dot{\gamma}^\alpha$ is the plastic shearing rate on the α^{th} slip system. The resolved stress on the α^{th} slip system is given by $\boldsymbol{\tau}^\alpha = \tilde{\boldsymbol{T}} \cdot \boldsymbol{S}_0^\alpha$. The resolved shear stress $\boldsymbol{\tau}^\alpha$ attains a critical value s^α on the systems where slip occurs ($\dot{\gamma}^\alpha > 0$). Further, the resolved shear stress does not exceed s^α on the inactive systems with $\dot{\gamma}^\alpha = 0$. The hardening law for the slip resistance s^α is taken as,

$$\dot{s}^\alpha(t) = \sum_\beta h^{\alpha\beta}\dot{\gamma}^\beta,\ s^\alpha(0) = s_0^\alpha \tag{3.2}$$

3.2 Single crystal model of magnetostriction

When a magnetic field is applied to a Galfenol single crystal, the boundaries between the magnetic domains shift and rotate, both of which cause a change in the material's dimensions. Galfenol crystal has minimal energy in the $< 111 >$ family of directions (easy direction of magnetization) and maximal magnetocrystalline energies in the $< 100 >$ family (hard directions). Magnetostrictive strain is specified using two independent parameters, λ_{100} and λ_{111}, that characterize the changes in normal strain along the $< 111 >$ and $< 100 >$ direction resulting from the rotation of a magnetization state into these directions. The magnetostrictive strain tensor for a

crystal with magnetization direction given by the unit vector $\boldsymbol{m} = (m_x, m_y, m_z)$ (in the crystal coordinate system) is then given by the following expression:

$$\boldsymbol{\lambda} = \frac{3}{2}\begin{bmatrix} \lambda_{100}(m_x^2 - \frac{1}{3}) & \lambda_{111}(m_x m_y) & \lambda_{111}(m_x m_z) \\ \lambda_{111}(m_y m_x) & \lambda_{100}(m_y^2 - \frac{1}{3}) & \lambda_{111}(m_y m_z) \\ \lambda_{111}(m_z m_x) & \lambda_{111}(m_z m_y) & \lambda_{100}(m_z^2 - \frac{1}{3}) \end{bmatrix} \tag{3.3}$$

A magnetic free energy is then defined that represents the amount of energy required to rotate a unit volume with a known magnetization to a given direction from a reference direction. We use the model from Armstrong [12] that represents the free energy as a sum of internal and external energy terms. The internal energy represents the energy released as the magnetization vector rotates away from a hard direction towards an easier direction of magnetization. The following form of internal energy is taken:

$$E_I = K_1(m_x^2 m_y^2 + m_y^2 m_z^2 + m_x^2 m_z^2) \tag{3.4}$$

The simple form for E_I used here ensures that a domain in the crystal has minimal and maximal energies when oriented, respectively, along the $< 111 >$ directions (easy direction) and the $< 100 >$ family (hard directions). Application of an external magnetic field leads to an energy change in energy proportional to the intensity of the magnetic field, $\boldsymbol{H}$, the magnetization of the domain, $\boldsymbol{M}$, and the direction between them. The direction of the applied magnetic field is represented as $\boldsymbol{n} = (n_x, n_y, n_z)$ in the crystal coordinate system.

$$E_H = -\mu_0 M H(\boldsymbol{m} \cdot \boldsymbol{n}) \tag{3.5}$$

The energy contribution (per unit volume) associated with the interaction of ex-

ternally applied stresses with magnetostrictive strains is given as:

$$E_\sigma = -\boldsymbol{\sigma} \cdot \boldsymbol{\lambda} \tag{3.6}$$

In an ideal crystal without defects (at T = 0K), the domain would align in the direction of minimal energy. However, domain magnetization is expected to follow a Boltzmann–like distribution at higher temperatures due to an increase in entropy. The probability, P, that the magnetization direction is equal to $\boldsymbol{m}$ is given as:

$$P(\boldsymbol{m}) \propto exp(-\frac{(E_I + E_H + E_\sigma)}{\Omega}) \tag{3.7}$$

The parameter Ω represents the spread of the magnetization direction from the ideal direction (of minimal energy). The magnetostriction strain tensor is obtained by averaging the strains over the probability density of magnetization in the crystal.

$$\boldsymbol{\lambda} = \frac{\int P(\boldsymbol{m})\boldsymbol{\lambda} dm}{\int P(\boldsymbol{m}) dm} \tag{3.8}$$

In sample frame ($\boldsymbol{\lambda}_s = R^T \boldsymbol{\lambda} R$), where R is the rotation tensor.
Similarly, the average value of Magnetization($\boldsymbol{M} = M\boldsymbol{m}$) can be calculated as

$$\boldsymbol{M} = \frac{\int P(\boldsymbol{m})\boldsymbol{M} dm}{\int P(\boldsymbol{m}) dm} \tag{3.9}$$

and $\boldsymbol{M_s} = R^T \boldsymbol{M}$ is component of magnetization of domain in the sample direction. The above two integrals are calculated by using a finite element representation of the surface of a unit sphere (with 320 quadrilateral elements). Each point on the unit sphere represents a unit normal vector (magnetization direction). The free energy is computed over all the integration points for each element and the integral over $\boldsymbol{m}$ is computed by summing up the element contributions. The actual magnetization is calculated by subtracting out the strains for an unstressed reference crystal of same

orientation, but with zero applied magnetic field. The computed strains for each integration point in the FE mesh is then volume averaged in Eq.(3.8) to compute the overall magnetization strain in the material. A total Lagrangian FEM formulation is used to solve the microstructure deformation problem. The unloading process is modeled as a non-linear (finite deformation) elasto-static boundary value problem.[126]

The final stress($\boldsymbol{\sigma}$) after unloading is affected by the stress due to magnetostriction($\boldsymbol{\lambda}$) as well as residual elastic stress ($\boldsymbol{\sigma}_{res}$). Further $\boldsymbol{\lambda}$ is also dependent on $\boldsymbol{\sigma}_{res}$, this coupled configuration results in non-linear finite element formulation. For the magnetoelastic analysis, small deformation elastic model was used. It is assumed that strain at any point in the material consists of elastic strain and magnetic strain which can be added linearly i.e

$$\boldsymbol{\epsilon} = \boldsymbol{\epsilon}_{elastic} + \boldsymbol{\lambda} \tag{3.10}$$

From Hooke's law

$$\boldsymbol{\sigma} = \bar{\boldsymbol{C}}\boldsymbol{\epsilon}_{elastic} = \bar{\boldsymbol{C}}(\boldsymbol{\epsilon} - \lambda) \tag{3.11}$$

where $\bar{\boldsymbol{C}}$ is the fourth-order anisotropic elasticity tensor.
The elastic problem solved is

$$\nabla^{s}_{T}.\boldsymbol{\sigma_{res}} = 0 \tag{3.12}$$

where ∇^{T}_{s} is transpose for ∇_s defined in [1]

[1] $$\nabla_s = \begin{bmatrix} \frac{\partial}{\partial x} & 0 & 0 \\ 0 & \frac{\partial}{\partial y} & 0 \\ 0 & 0 & \frac{\partial}{\partial z} \\ 0 & \frac{\partial}{\partial z} & \frac{\partial}{\partial y} \\ \frac{\partial}{\partial z} & 0 & \frac{\partial}{\partial x} \\ \frac{\partial}{\partial y} & \frac{\partial}{\partial x} & 0 \end{bmatrix}$$

Using the Newton Raphson iterative scheme we solve the matrix equation

$$K\delta u = R \tag{3.13}$$

where Stiffness Matrix (K) and Residual(R) calculated in terms of $\bar{C}$, B and λ for zero body force(F_b) as

$$R = -\int_{\Omega^e} B^{e^T}\bar{C}^e B^e dd\Omega + \int_{\Omega^e} B^{e^T}\bar{C}\lambda d\Omega + \int_{\Gamma^e} N^{e^T}\bar{t}d\Gamma \tag{3.14}$$

$$K = \int_{\Omega} B^{e^T}\bar{C}^e B^e dd\Omega - \int_{\Omega} B^{e^T}\bar{C}\frac{\partial\lambda}{\partial u}d\Omega \tag{3.15}$$

where

$$\frac{\partial\lambda}{\partial u} = \frac{\partial\lambda}{\partial\sigma}\frac{\partial\sigma}{\partial u} = \frac{\partial\lambda}{\partial\sigma}\bar{C}B \tag{3.16}$$

Standard Galerkin formulation is used to calculate Shape function(N) and derivative of Shape function (B).

To calculate $\frac{\partial\lambda}{\partial\sigma}$ a perturbation approach is applied on the model in Eq.(3.8).

3.3 Numerical Examples

The slip system hardening model used in the examples is given as:

$$h^{\alpha\beta} = [q + (1-q)\delta^{\alpha\beta}]h^{\beta} \text{ (no sum on } \beta) \tag{3.17}$$

where h^{β} is a single slip hardening rate, q is the latent-hardening ratio and $\delta^{\alpha\beta}$ is the Kronecker delta function. The parameter q is taken to be 1.0 for coplanar slip systems and 1.4 for non-coplanar slip systems. For the single-slip hardening rate, the

following specific form is adopted:

$$h^{\beta} = h_o(1 - \frac{s^{\beta}}{s_s})^a \tag{3.18}$$

where h_o, a, and s_s are slip hardening parameters taken to be identical for all slip systems, with values $h_o = 500$ MPa, $s_s = 350$ MPa and $a = 2.25$ for BCC Galfenol single crystals. The initial value of slip system resistance is calibrated as $s_o = 180MPa$. Values of elastic parameters for Galfenol crystal are taken as $C_{11} = 213$ GPa, $C_{12} = 174$ GPa and $C_{44} = 120$ GPa. The initial texturing of the material is assumed to be random.

Plastic deformation due to crystallographic slip is assumed to occur in the $< 111 >$ direction, and the possible slip planes are of the {110}, {112}, and {123} type. The model adequately captures the macroscopic tensile mode stress-strain response at room temperature reported in [79] well as shown in Fig. 3.1(right). To further validate the microscale model, we compared the results with textures seen in BCC iron rolling processes and textures predicted by our model. The model results from Fig. 3.1(b) captures both α and γ texture seen from experiments (in Fig. 3.1(c) [17]). Results were also compared with experimental rolling textures of BCC Fe-16.83%Ga results (Fig 3.1(a) [79]). However, the experiment indicates a $\{112\} < 132 >$ texture in addition to the expected γ texture pointing to the possible presence of additional deformation mechanisms in Galfenol that needs future study.

The effect of a rolling process on polycrystalline Galfenol was subsequently studied. A microstructure with 31 grains was generated using a standard Voronoi tessellation based on our previous work [126]. Texture was randomly assigned and the microstructure was discretized into 690 quadrilateral elements. A rolling process (with plane strain compression along y-axis) was studied with a strain rate of 10^{-3} for a time of 10 seconds. The microstructure was subsequently unloaded to study the effect

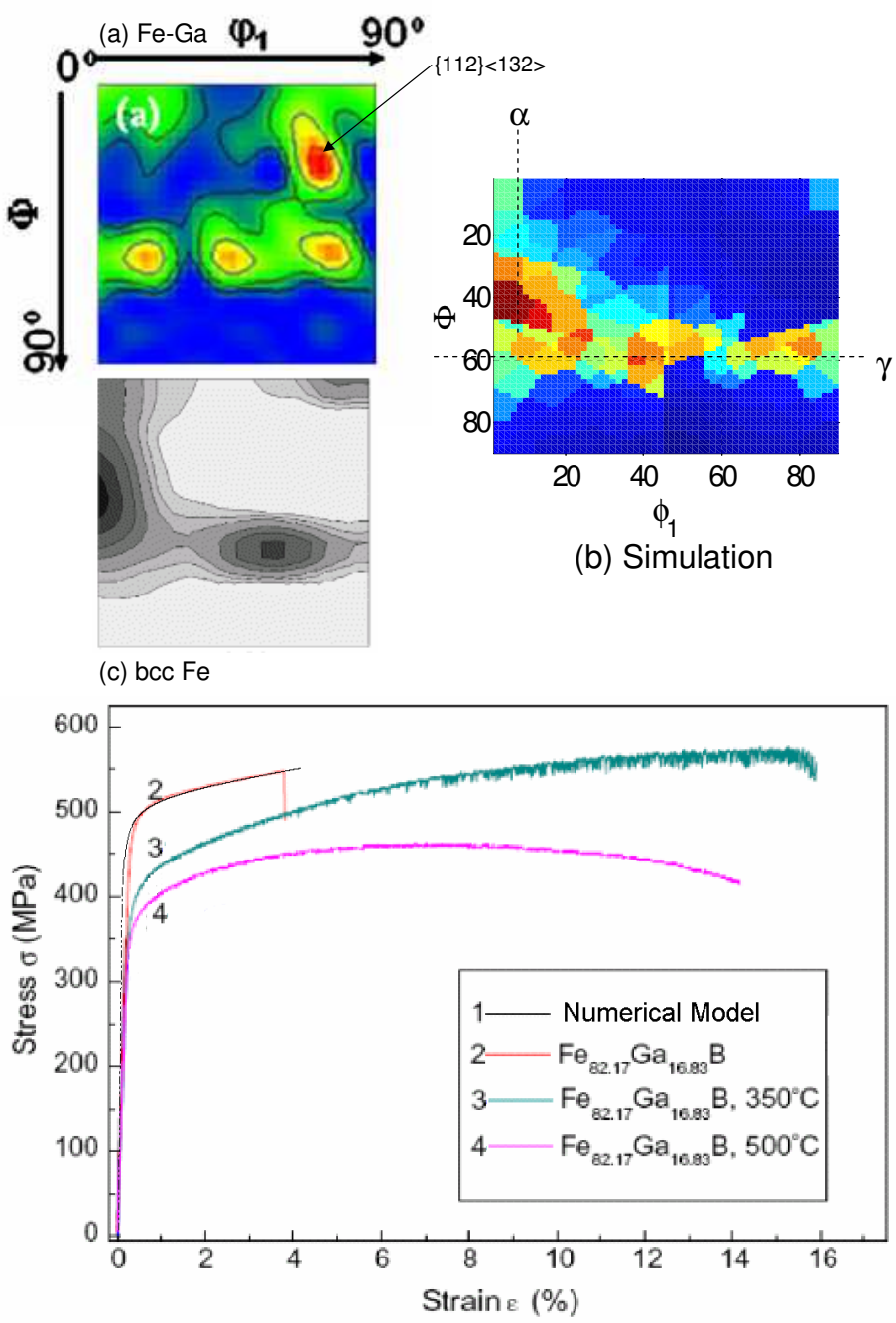

Figure 3.1: *(left) Comparison of textures (Euler angle space, $\phi_2 = 45^o$) predicted by our model (Fig. 3.1(b)) with experiments on BCC iron in Fig. 3.1(c) [17]. Experimental rolling textures of BCC Fe-16.83%Ga results (Fig 3.1(a) [79]) are also shown. The experiment indicates a $\{112\} < 132 >$ texture in addition to the expected γ texture. (right) Comparison of results of current model with published results in [79]. The plot shows tensile test curves of as-cast polycrystalline Galfenol at different temperatures.*

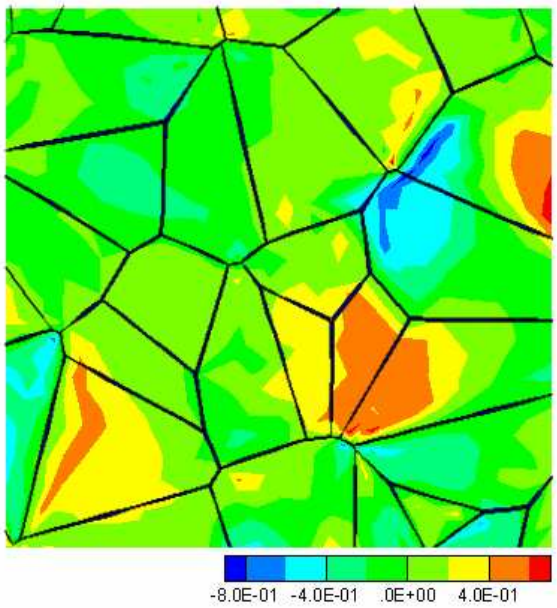

Figure 3.2: *Final microstructure after rolling to 1% strain and unloading. The misorientation distribution over grains that depicts the change in Neo-Eulerian angle from the initial configuration (t=0).*

of the rolling process. After unloading from a strain of 1%, a spring back of 0.065% was observed in the y-direction. The misorientation development was computed using the change in neo-eulerian angle of rotation $\xi(t)$ at time t from the values of $\xi(t=0)$ of the initial texture. ξ is obtained from the Rodrigues parametrization given by $\boldsymbol{r} = \boldsymbol{n}\tan(\frac{\xi}{2})$ where $\boldsymbol{n}$ denotes the axis of rotation. The change in the neo-eulerian angle from the initially assigned orientation of grains shown in Fig. 3.2(b) clearly shows the formation of disoriented regions within grains at this moderate deformation.

The magnetostrictive model developed here was subsequently validated by comparing with results in literature [16]. The values of constants used in this study are as follows:

$K_1 = 3.6 \times 10^4$ J/m^{-1}

$\lambda_{100} = 170 \times 10^{-6}$ $\lambda_{111} = -4.67 \times 10^{-6}$

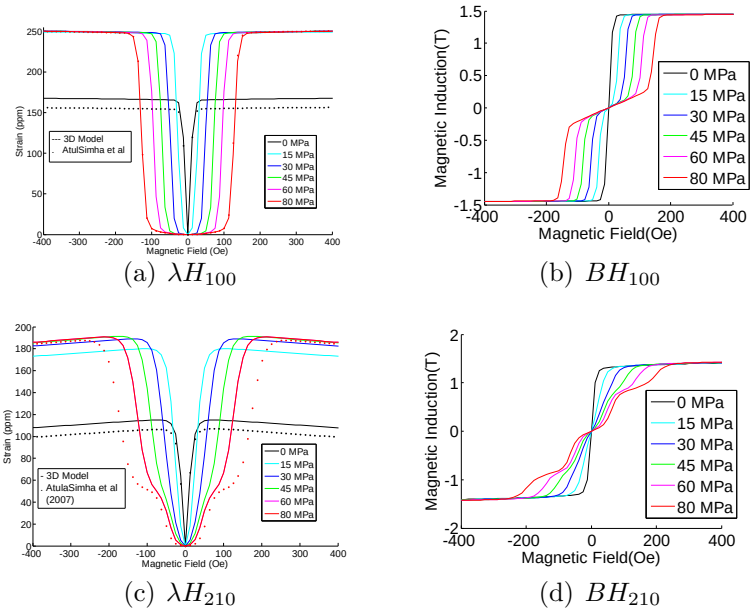

(a) λH_{100} (b) BH_{100}

(c) λH_{210} (d) BH_{210}

Figure 3.3: *Magnetostrictive $\lambda - H$ and B-H response for various compressive pre-stress values of 0, 15, 30, 45, 60 and 80 MPa along* [100] *and* [210] *crystallographic direction.*

$M_s = 1.83/\mu_0$ Am^{-1} $\Omega = 625$ J$/m^{-3}$

Our model includes two enhancements to a single crystal model to better account for the behavior of polycrystalline Galfenol. Firstly, we use a 3D model that includes all stress components in the crystal (this includes the effect of shear stress produced by rolling or any other mechanical processes). Secondly, instead of volume averaging, we have employed a finite element homogenization approach to compute the effective properties.

We show the λ-H and B-H plot of 18% Ga single-crystal FeGa in the [100],[210] and [111] directions for various compressive pre-stress values (0, 5, 20, 40 and 80 MPa) in Fig.[3.3]. In [100] case, the stress and magnetic field is applied along [100] crystallographic direction. In the plots, the continuous line (3D model) is of our work and dotted point (1D model) is from Ref. [16]. The plots for λ-H show good comparison with deviations at the highest compressive stresses but the saturation value

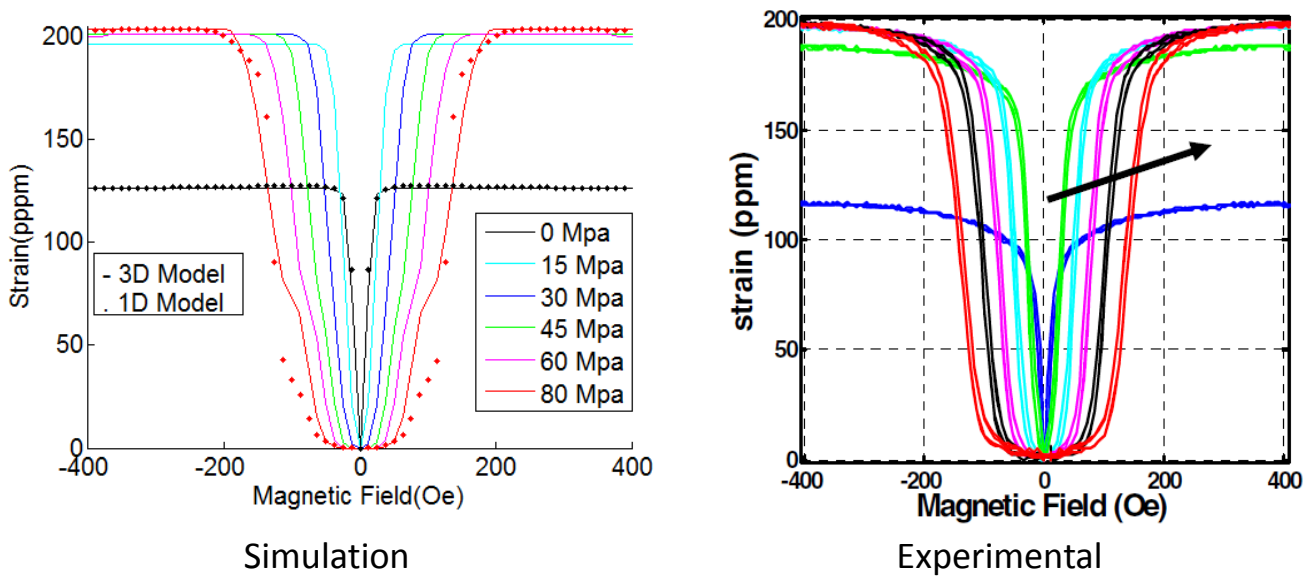

Figure 3.4: *Magnetostrictive $\lambda - H$ response of polycrystal for various compressive pre-stress values of 0, 15, 30, 45, 60 and 80 MPa*

is same for both models. Once we got the good comparison for single-crystal case, we used our model to obtain experimental actuation behavior for polycrystals which is shown in Fig.[3.4](left). These plots are also in good agreement with published results Fig.[3.4](right).

Using the magnetostriction model, the final magnetostrictive state was computed over each element. Here, a 20000 A/turn (= 251.33 Oe) magnetic field was applied along the y-direction. The magnetostrictive strains along the x- and y- directions, respectively, are plotted in Fig. 3.6. It is seen that grains with high x- strains are associated with low y- strains and vice versa. Significant changes in magnetostriction strains are seen even within a single grain due to the effect of misorientations and residual stresses.

Finally, we studied the effect of annealing on magnetostrictive behavior. In Fig[3.5], three cases are plotted. Case 1 is Galfenol without any processing, case 2 involves rolling Galfenol for 10s and case 3 involves rolling Galfenol for 10s and then annealing. As we see from the plot, rolling with annealing gives the same value for

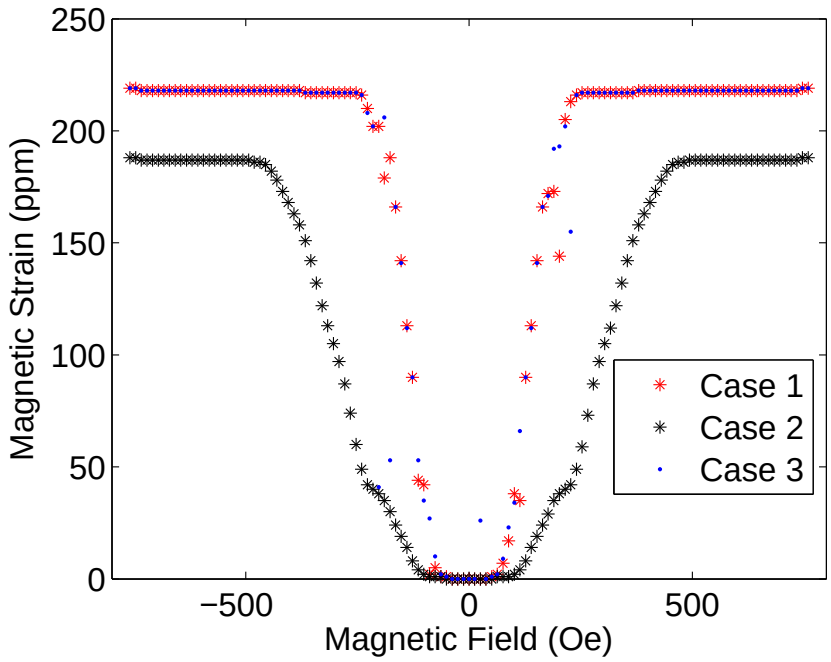

Figure 3.5: *Effect of Annealing Process on magnetostriction process*

magnetic strain(λ) as that of no processing showing that annealing effectively removes the residual stresses which has the greatest bearing on magnetostrictive properties.

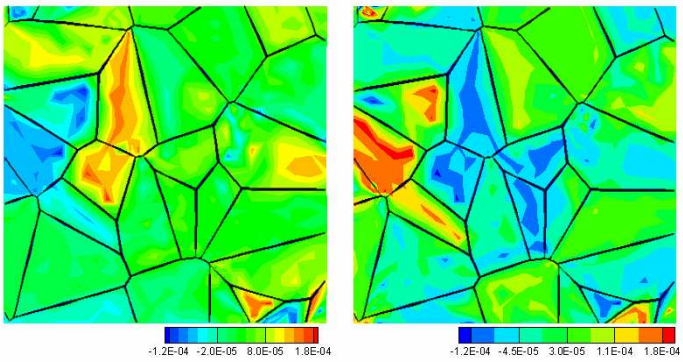

Figure 3.6: *Magnetostrictive strain distribution in the as-rolled microstructure (to 1 % strain) under a y-direction magnetic field of 251.33 Oe. (a) Magnetostrictive strains along x-direction and (b) strains along the y- direction.*

CHAPTER IV

Structure-property optimization in Galfenol through data mining of probabilistic descriptors

Recent developments in materials-by-design have allowed a more advanced systems approach that integrates processing, structure and property through multi-scale computational material models [90]. In the area of composites, techniques that enable tailoring of microstructure topology have allowed design of structures with interesting extremal properties such as negative thermal expansion [120] and negative Poisson's ratio [71]. In contrast to composites, techniques that allow tailoring of properties of polycrystalline alloys involve tailoring of preferred orientation of crystals manifested as the crystallographic texture. In this research, we propose a data mining framework for material texture-property optimization problems with high dimensionality. Given an optimization problem with an objective function that represents a certain property, and a set of texture variables as well as constraints, we first construct a database of representative variable-objective data instances with randomization techniques. Then, by employing feature selection and classification techniques, we obtain variable rankings and therefore refine the search path and search region. Finally, by applying traditional optimization methods (Linear Programming for linear functions and Genetic Algorithm for nonlinear functions) on the reduced variable set, we are able to find the optimized property with texture variable combinations that are

difficult to obtain otherwise, with significantly reduced computational effort.

4.1 Modeling of texture

4.1.1 Representation in Rodrigues space

Orientation distribution function (ODF) [29, 63], the probability density function for orientations, is employed for the quantification of crystallographic texture. Texture evolution methodologies use parameterizations for the crystal lattice rotation which together with the crystal symmetry define the problem domain. Angle-axis representations define an alternative way of representing texture compared to the use of Euler angles [29, 140]. We employ the axis-angle parametrization of the orientation space proposed by Rodrigues [68]. This is based on the unique association of an orientation with a rotation axis, and an angle of rotation about the axis. The Rodrigues' parametrization is created by scaling the axis of rotation $\mathbf{n}$ as $\mathbf{r} = \mathbf{n}tan(\frac{\theta}{2})$, where θ is the rotation angle. A proper rotation $\mathbf{R}$ relates the lattice orientation to a reference orientation. Given the Rodrigues parametrization $\mathbf{r}$, the rotation $\mathbf{R}$ can be obtained as,

$$\mathbf{R} = \frac{1}{1 + \mathbf{r}.\mathbf{r}}(\mathbf{I}(1 - \mathbf{r}.\mathbf{r}) + 2(\mathbf{r} \otimes \mathbf{r} + \mathbf{I} \times \mathbf{r})) \tag{4.1}$$

The fundamental region represents a region of the orientation space such that each crystal orientation is represented uniquely within the space. Fundamental region for the cubic symmetry group results in a truncated cube. The planes that form the faces of the cube are introduced by symmetry rotations about the $\langle 100 \rangle$ family of axes and the corners are truncated by planes introduced by rotations about the $\langle 111 \rangle$ axes. The ODF (represented by $\mathcal{A}$) describes the local density of crystals over this fundamental region of orientation space. The volume fraction of crystals within a part ($\Re^*$) of the fundamental region is given by $v_f(\Re^*) = \int_{\Re^*} \mathcal{A} dv$. The ODF is normalized to unity

over the fundamental region. Here $dv = \sqrt{det\boldsymbol{g}}\, dr_1 dr_2 dr_3$. Since the orientation space is non-Euclidean, the volume element is scaled by the term $\sqrt{det\boldsymbol{g}} = cos^4(\theta/2)$ where $\boldsymbol{g}$ is the metric for the space. If the orientation-dependent property for a single crystal $\chi(\boldsymbol{r}, t)$ is known, any polycrystal property can be expressed as an expectation value or average given by:

$$< \chi >= \int_{\mathcal{R}} \chi(\boldsymbol{r}, t)\mathcal{A}(\boldsymbol{r}, t)dv \tag{4.2}$$

4.2 Property representation and optimization in Rodrigues space

Finite element discretization of the orientation space and associated integration schemes using Gauss quadrature allows matrix representation of several properties of the ODF. ODF is assumed to be discretized into N independent nodes with N_{elem} finite elements and N_{int} integration points per element. The constraint that the ODF is normalized to unity over the fundamental region can then be written as:

$$\int_{\mathcal{R}} \mathcal{A}dv = \sum_{n=1}^{N_{elem}} \sum_{m=1}^{N_{int}} A(\boldsymbol{r}_m) w_m |J_n| \frac{1}{(1 + \boldsymbol{r}_m \cdot \boldsymbol{r}_m)^2} = 1 \tag{4.3}$$

where $A(\boldsymbol{r}_m)$ is the value of the ODF at the m-th integration point with global coordinate $\boldsymbol{r}_m$ of the n-th element, $|J_n|$ is the jacobian determinant of the n-th element and w_m is the integration weight associated with the m-th integration point. This is equivalent to the linear constraint: $\boldsymbol{q}^{int^T}\boldsymbol{A}^{int} = 1$, where $q_i^{int} = w_i|J_i|\frac{1}{(1+r_i \cdot r_i)^2}$ and $A_i^{int} = A(\boldsymbol{r}_i)$, where each i corresponds to a combination (n, m), $i = 1, \ldots, N_{int} \times N_{elem}$. If the orientation-dependent property for a single crystal $\chi(\boldsymbol{r})$ is known, any

polycrystal property can be expressed in a linear form as follows:

$$< \chi >= \int_{\mathcal{R}} \chi(\boldsymbol{r})\mathcal{A}(\boldsymbol{r})dv = \sum_{n=1}^{nel}\sum_{m=1}^{nint} \chi(\boldsymbol{r}_m)A(\boldsymbol{r}_m)w_m|J_n|\frac{1}{(1+\boldsymbol{r}_m\cdot\boldsymbol{r}_m)^2} \tag{4.4}$$

This is again equivalent to an equation linear in the ODF: $< \chi >= \boldsymbol{p}^{int^T}\boldsymbol{A}^{int}$, where $p_i^{int} = \chi(\boldsymbol{r}_i)w_i|J_i|\frac{1}{(1+r_i\cdot r_i)^2}$ and $A_i^{int} = A(\boldsymbol{r}_i)$, $i = 1,\ldots,N_{int}\times N_{elem}$.

Using reduced integration with one integration point per element at local coordinate of $(0.25, 0.25, 0.25)$ and an integration weight of $w = \frac{1}{6}$, the simplified property matrix $\boldsymbol{p}^{int}$ corresponding to polycrystal average properties $[< \chi_1 >,\ldots,< \chi_{n_p} >]$ and the normalization constraint vector ($\boldsymbol{q}^{int}$) are given as:

$$\boldsymbol{p}^{int} = \begin{bmatrix} \frac{1}{6}\chi_1(\boldsymbol{r}_1)|J_1|\frac{1}{(1+r_1\cdot r_1)^2} & \cdots & \frac{1}{6}\chi_{n_p}(\boldsymbol{r}_1)|J_1|\frac{1}{(1+r_1\cdot r_1)^2} \\ \frac{1}{6}\chi_1(\boldsymbol{r}_2)|J_2|\frac{1}{(1+r_2\cdot r_2)^2} & \cdots & \frac{1}{6}\chi_{n_p}(\boldsymbol{r}_2)|J_2|\frac{1}{(1+r_2\cdot r_2)^2} \\ \cdots & & \\ \frac{1}{6}\chi_1(\boldsymbol{r}_{N_{el}})|J_{N_{el}}|\frac{1}{(1+r_{N_{el}}\cdot r_{N_{el}})^2} & \cdots & \frac{1}{6}\chi_{n_p}(\boldsymbol{r}_{N_{el}})|J_{N_{el}}|\frac{1}{(1+r_{N_{el}}\cdot r_{N_{el}})^2} \end{bmatrix}$$

$$\boldsymbol{q}^{int} = \begin{bmatrix} \frac{1}{6}|J_1|\frac{1}{(1+r_1\cdot r_1)^2} \\ \frac{1}{6}|J_2|\frac{1}{(1+r_2\cdot r_2)^2} \\ \cdots \\ \frac{1}{6}|J_{N_{el}}|\frac{1}{(1+r_{N_{el}}\cdot r_{N_{el}})^2} \end{bmatrix}$$

The $\boldsymbol{H}$ matrix can be defined from the equation $A_e^{int} = 0.25\sum_{i=1}^{4} A_e^i$ where A_e^{int} is the integration point ODF value at element e and $A_e^i, i = 1,\ldots,4$ refers to the ODF values at the four nodes of the tetrahedral element e. The $\boldsymbol{p}$ matrix is formed as $\boldsymbol{p} = \boldsymbol{H}^T\boldsymbol{p}^{int}$ so that any property $\boldsymbol{d}$ can be represented as the scalar product $\boldsymbol{p}^T\boldsymbol{A}$ with the ODF values ($\boldsymbol{A}$) at the independent nodal points.

An additional constraint in the representation of the material set is the symmetry of the ODF. Orientations on each pair of planes in the fundamental region are

equivalent under the symmetries. In the cubic fundamental region, orientations on the {100} faces are identified with orientations on the diametrically opposed faces following rotations through $\pi/4$ about the corresponding $< 100 >$ axes. Similarly, symmetric orientations on the various {111} faces are obtained following rotations through $\pi/3$ about the $< 111 >$ axes. The space of ODF values at integration points of the FE mesh does not represent this symmetry. Symmetry conditions are enforced by considering the set of independent nodal points instead of the integration points. Independent nodal points are the reduced set of nodes obtained by accounting for symmetry conditions at the boundaries of the ODF. Let $\boldsymbol{H}$ be the matrix converting the independent nodal values $\boldsymbol{A}^{node}$ to the integration point values $\boldsymbol{A}^{int}$ through the shape functions, then, $\boldsymbol{A}^{int} = \boldsymbol{H}\boldsymbol{A}^{node}$. The independent nodal values $\boldsymbol{A}^{node}$ are sufficient to describe the ODF due to the symmetry of the fundamental region. Vector containing the values of the ODF at independent nodal points $\boldsymbol{A}^{node}$ is hereafter referred to as $\boldsymbol{A}$. The ODF constraint can then be written in terms of the modified $\boldsymbol{q}^T = \boldsymbol{q}^{int^T}\boldsymbol{H}$ as $\boldsymbol{q}^T\boldsymbol{A} = 1, \boldsymbol{A} \geq 0$. Properties are specified using the modified $\boldsymbol{p}^T \equiv \boldsymbol{p}^{int^T}\boldsymbol{H}$ as $< \chi >= \boldsymbol{p}^T\boldsymbol{A}$. For calculating more than one property, $\boldsymbol{p}$ is written in a matrix form. Another constraint is based on the positivity of the ODF which constrains the nodal values of the ODF to be positive ($\boldsymbol{A} \geq 0$). Space of all possible ODFs thus includes three constraints: normalization, positiveness and symmetry. The constraint $\boldsymbol{q}^T\boldsymbol{A} = 1, \boldsymbol{A} \geq 0$ means that the complete set of all possible ODFs is a hyperplane in the space of independent nodal values, which we call the 'material plane'.

4.2.1 Calculation of properties

In this section, we discuss methodologies used for calculation of properties such as Young Modulus(E), Yield Strength(Y) and magnetostrictive strain(m) for polycrystalline material.

1. Polycrystal stiffness calculation:

Values of elastic parameters for BCC Galfenol crystal are taken as $c_{11} = 123.0GPa, c_{12} = 174GPa, c_{44} = 120GPa$. The polycrystal stiffness, $\bar{\boldsymbol{C}}$, is computed through a weighted average (over $\mathcal{A}$) of the stiffness of individual crystals expressed in the sample reference frame.

2. Yield strength calculation:

The crystal plasticity model described in the previous chapter is used to calculate the yield strength at all Gauss points. In this method, the polycrystal at each integration point in the macro-scale mesh is subjected to uniaxial (y-axis) tension conditions up-to strain of 0.2% to obtain the corresponding 0.2% offset yield strength at each integration point.

3. Magnetostrictive Strain calculation:

The calculation for Magnetostrictive strain is given in detail in the previous chapter (Section 3.2).

4.3 Traditional structural optimization design

The material structural optimization design is essentially a mathematical optimization problem where the objective is to find structure patterns that maximize or minimize a certain property. The property function is given, either linear or nonlinear, and the optimization is conducted on a high dimensional space. The problem can be formed as follows.

$$maximize\, F(\boldsymbol{X})$$
$$\boldsymbol{X} = \{x_1, x_2, \ldots, x_D\} \subseteq \mathbf{R}^D$$
$$subject\, to\, \boldsymbol{a}^T\boldsymbol{X} = 1,\ \boldsymbol{X} \geq 0$$

The selection of material and geometry to minimize (or maximize) some given property has been a common problem in material science. Single-objective opti-

mization deals with only one objective function, whereas multi-objective optimization refers to optimizing simultaneously a collection of objective property functions. While people often approach a multi-objective optimization problem by formulating its function into a single-objective one, using methods as weighted sum, weighted product, etc., therefore in this context we do not distinguish these two types.

Traditionally, the answer that leads to an optimum can be obtained by an exhaustive search among the numerous choices in the searching domain bounded by some boundary conditions and constraints. More intelligently and less laboriously, the search can be guided by heuristics, and how the heuristic is designed is discussed by various researchers in the area of searching algorithms and artificial intelligence [112] [49].

However, traditional search-based methods suffer from the high dimensionality used to in structure representation. The increase in the number of variables would extremely enlarge the plausible space and increase the number of evaluations of the objective functions. Both the computational speed and the memory constraint become crucial issue. The reported studies on the scalability of those algorithms are scarce.

4.3.1 Linear programming

When the property objective function is linear, with also linear equality and inequality constraints on material structure, the problem can be solved efficiently using linear programming (LP). Algorithms for linear programming include simplex, interior point, active-set, etc., and simplex is the most widely used. In the structural optimization design, the constraints on ODF define a feasible region known as a polytope, in which the vertices are the best answers - ODFs that give extremal properties, and the edges are feasible ways. The algorithm starts at a vertex, walks along the edges to another vertex. This goes on until an optimal property is found for sure. The

assumption of all functions being linear is obviously too strict in real applications. Alternatively, when the function is nonlinear, the traditional way is to approximate it into a linear problem. Sequential linear programming (SLP) breaks a bigger, linear or nonlinear, problem into a sequential of approximate linear subproblems, obtained by writing linear Taylor series expansions for the objective and constraint functions. Nonlinear programming (NLP) includes a category of methods that forms further subcategories by examining the convexness of the problem space.

4.3.2 Genetic algorithms

Genetic Algorithm (GA) belongs to the class of evolutionary algorithms, which generate solutions to optimization problems using techniques inspired by natural evolution (survival of the fittest). The theory was proposed by Holland [56] and further developed by Goldberg [50] and others. GA starts from a population of candidate microstructures, and keep generating better and better offspring in iterations, with operations as mutation, selection, and crossover. The new population of microstructures are evaluated and the best ones are selected to produce the next generation, as in the nature biological evolution. The randomness and evolutionary scheme of GA ensure that the candidate microstructures produced through generations get closer and closer to the optimum stochastically. When dealing with high dimensionality problems, as the number of variable increases, so does the required population size, which implies a large number of cost-function evaluations and thus large time consumption.

4.4 Structural optimization with data mining

In recent years, the dramatic emergence of the information era has seen the development of data mining methods and tools booming. Areas of application include finance, genomics, and medicine, to name a few, where increasingly rich data are

collected, stored and shared but to manage, parse and analyze has become a bottleneck. Data mining bears the notion of "learning from data", aiming at discovering important and meaningful patterns from a collection of data instances where each instance is represented by a (often multidimensional) vector in feature space, either associated with a supervisory label (in the case of supervised learning) or not (in the case of unsupervised learning). Mining of such patterns results in dimension being reduced, information discovered, and knowledge formed.

Material scientists have begun to explore data mining strategies and nourished the area of material informatics [103]. Applications as basic as thermodynamics and crystallography, and as complex as microstructure have all seen data mining playing an important role. Both supervised data classification and unsupervised data clustering have been applied to problems as separating crystal structures into distinct classes, identifying classes of given compounds, among others. The goal is to uncover the essence of materials by understanding the structures and predicting the properties, and hence accelerate the new material discovery and design. To be able to achieve that, there is a need to link structure parameters of a material to its properties.

In our context, the purpose is to search for an optimal ODF pattern that leads to the extremal value of properties. But the number of possible patterns is almost limitless, making an empirical search laborious and expensive. Here we show that data mining can instead direct the search for possible ODF structures, towards only valuable and critical features of ODF. By reducing the searching space to only a valuable subspace, both the searching time and the quality of the optimal solutions found are dramatically improved.

4.4.1 Framework

We consider the problem of global optimization in high dimensions. It is of great interest to consider the case where the domain of the function to be optimized is

high dimensional, but the optimal values of the function depend only on a reduced, albeit unknown, set of variables. The dimensionality of searching space limits the performance of the optimization methods to a large extent. With the number of variables of the function to be optimized getting larger and larger, the traditional optimization methods either take too long to operate or the memory demand gets impractical.

Recall in the optimization problem definition we have $\boldsymbol{X} = \{x_1, x_2, \ldots, x_D\} \subseteq \mathbf{R}^D$. The original variable dimension is D. Now we assume the optimum of the function F only depends on some intrinsic dimension d, where $d \ll D$, in that only d variables in X are considered strongly and actively related to the optimum of F. Once the values of those d variables are fixed, the rest variables can be determined by taking a weighted equal value to satisfy the constraint.

We formalize such an insight and provide a framework of high dimensional global optimization based on data mining and feature selection. The framework is depicted in Fig. 4.1. As it indicates, on top of a traditional structure optimization process that consists of representation and the application of standard optimization techniques, data mining methods introduce two additional steps: database construction, and feature selection. The following two subsections are devoted to each of them. The objective is to reduce the dimension of features, and hence the searching space, by learning "which features in the microstructure vector is most related to a sufficiently high (or low) property".

4.4.2 Database construction

As we attempt to apply data mining to learn and facilitate an optimization process, data are an essential component. We focus on the supervised feature selection methods, where the importance factors of features are learned from their relationship with the class target. Hence a training set of $\{X_i, d_i\}$ is needed prior to the feature

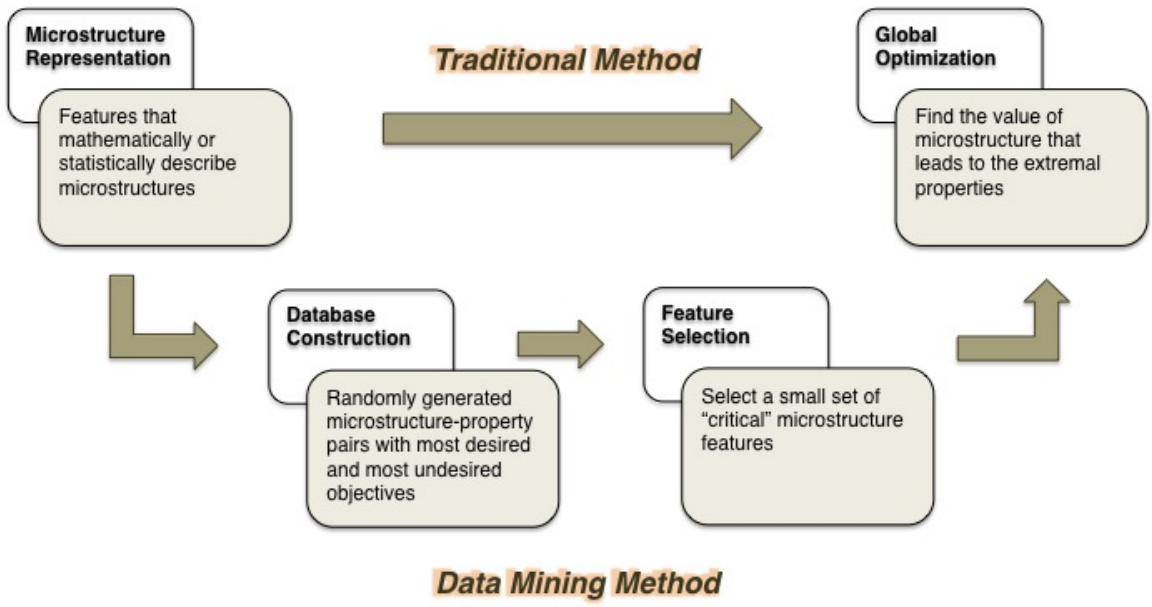

Figure 4.1: *Framework of Data Mining based Material Structure Optimization*

selection. The training set should be representative in the sense that the variable-class relationship is well embedded and presented. The set of training samples is also required to be unbiased, clean (as opposed to noisy), and sufficiently large in order to have the feature selection methods work well.

Given a property function $F(X)$, training examples $\{X_i, d_i\}$ can be generated where $X_i \subseteq R^D$, $d_i \in \{-1, 1\}$. Suppose in this problem we want to maximize the property.The class label $d_i = +1$ is assigned to the input vector X_i if the function value $F(X_i)$ is "sufficiently high". For most algorithms to work well, data from the opposing class is needed, which indicates sufficiently low property and are assigned a class label of -1.

Theoretically, with the property function $F(X)$ one can generate as much data as one wants, by varying the microstructure in any way. But the final set can only be of a certain size, and is meant to be representative. Randomness is considered the trick to remove bias. But how to randomize a microstructure under constraints is of great concern. The following serval methods, namely, Random Intervals, Random k Intervals, Random Every k, and Best-First Assignment, are developed to tackle the

issue from different angles. Firstly, they all ensure randomness. Secondly, while some of them give the right of taking values to every variable equally, the others tend to think that only a limited k variables are of importance and should be treated first, only we don't know which k. Randomness plays a role to pick them for us.

Random Intervals (RI): To account for the constraints $q^T \boldsymbol{A} = 1$ and $\boldsymbol{A} \geq 0$, we can consider the unit 1 is divided into r random intervals, or making $r - 1$ random cuts between the interval $[0, 1]$, where $r = |\boldsymbol{A}|$. Afterwards, the intervals generated are randomly assigned to each dimension of $\boldsymbol{A}$.

Random k Intervals (RkI): This is similar to Random Intervals but each time, only k intervals are generated and assigned to k random dimensions.

Random Every k (REk): Randomly generate k values at a time, continue only when the sum of the current k value does not exceed the threshold 1. Update the threshold to whats remaining, and repeat the process until the remainder is sufficiently small.

Best-First Assignment (BFA): Randomly pick a variable and assign to it a random value u, $0 \leq u \leq 1$. Distribute the remainder $1 - u$ evenly to all other variables so that the constraint is met. Compute the objective function and obtain the function value. Repeat n times and continue with whichever gives the best function value. Repeat the process until no variable is left.

We apply the four random data generating processes to obtain data entries in a input-objective form. Meanwhile, an important data polarizing procedure is overseeing this generation processes to assure that only the opposing two groups are saved, in this case, only the high valued ones and the low valued ones. As in an optimization problem one of the extremes is desired and the other one undesired, we denote them as S_D and S_U, respectively.

4.4.3 Feature selection

Variable and feature selection has become the focus of many research areas where a large number of variables are available and only a portion of them is of usage on building models. Often we refer variable to the raw input variables and feature to the constructed supposedly more meaningful variables from the input variables. But in the current context there is no need to distinguish the two since we consider the feature construction is done through finite element representation and has resulted in the ODF variables. The objective of feature selection before optimization is mainly the efficiency of running standard optimization algorithms, by reducing the measurement and storage requirements as well as narrowing the searching space.

Major variable and feature selection methods fall in the group of supervised learning based feature selection, in that they bear an insight of obtaining some metric indicating each features merit by looking at its relationship to the desired class target. Algorithms belonging to this regime include variable ranking, wrapper methods, filter methods, etc. Unsupervised feature selection studies the interrelationship among the features themselves, and attempts to eliminate the redundant features while keep representative ones. Popular methods include principal component analysis (PCA), kernel machines, clustering, etc. These methods are beyond our scope.

Four feature selection methods are applied in our experiments. They work either through calculating a metric to characterize the relevance of each feature with the class target, or through building classifiers from a subset of variables and evaluate the performance.

Correlation-based Feature Subset selection: Evaluates the worth of a subset of variables by considering the individual predictive ability of each variable along with the degree of redundancy between them. Subsets of features that are highly correlated with the class while having low intercorrelation are preferred. The dataset being used is S_D.

Chi-square: Evaluates the worth of an attribute by computing the value of the chi-squared statistic with respect to the class. The dataset being used is S_D.

Information Gain: Evaluates the worth of an attribute by measuring the information gain with respect to the class. The dataset being used is S_D.

Consistency: Evaluates the worth of a subset of variables by the level of consistency in the class values when the training instances are projected onto the subset of variables. The dataset being used is $S_D + S_U$.

SVM-based: Evaluates the worth of an attribute by using an SVM classifier. Attributes are ranked by the square of the weight assigned by the SVM. The dataset being used is $S_D + S_U$.

4.5 Material Design Problems

We are interested in applying the data mining techniques to identify microstructures that can optimize material properties specified by the following objective functions:

1. The Young Modulus (E). For metals E is inversely proportional to deflection of beams, so a lower modulus results in higher deflection for the same applied stress. Therefore our objective is to obtain a minimized E.

2. The Yield Stress (Y). Higher yield strength will increase the load bearing capacity of the structure. Therefore our objective is to maximize Y.

3. The Magnetostrictive strain (m_s). A higher value of m_s will enhance the capability of material to act as a sensor material. Therefore, our objective is to maximize m.

4. A composite function $F_1 = \frac{Y * m_s}{E}$. We are looking for a material with lighter weight and higher value for strength and magnetostrivtive strain, therefore to maximize F_1.

5. Another function F_2 is a multi–objective function given by a combination of two specific properties $\bar{\boldsymbol{C}}_{33} = 226.43GPa$ and $m_s = 28.33ppm$.

4.5.1 4-step optimization

The 4-step framework in Fig. 4.1 is applied to optimizing the problems in the following fashion.

Microstructure representation. Crystallographic texture is represented by ODF (denoted by $\mathcal{A}$), with a degree of 76. We keep this representation and treat each of the orientation in $\mathcal{A}$ as a design variable. In optimizing these objective functions we make sure the constraints $\boldsymbol{q}^T \boldsymbol{A} = 1, \boldsymbol{A} \geq 0$, explained in Section 4.2, are satisfied.

Database construction. Randomization methods in Section 4.4.2 are employed to generate a data set containing desired and undesired classes, denoted by S_D and S_U, respectively. The number of data instances generated by each randomization method is fixed as 1000. While with methods like RI and BFA it implies running the method for 1000 times, with RkI and REk it also involves a selection of k between 1 to 76 obeying a uniformed distribution. Then, a polarized procedure takes the instances with the highest and lowest objective values, the former as S_D and latter as S_U in a maximization problem (F_2,F_3,F_4,F_5), and reversely in a minimization problem (F_1).

Feature selection. With the feature selection and ranking methods described in 4.4.3, we can obtain rankings of variables either indicated by a similarity metric (e.g. Correlation, Consistency), a importance metric (e.g. Information Gain), or a classification accuracy (e.g. SVM). Table 4.2 displays the result of the ranked variables

Table 4.1: Feature rankings produced by various methods

	Correlation	Chi-square	Info Gain	Consistency	SVM
$1st$	ODF_2	ODF_3	ODF_3	ODF_3	ODF_3
$2nd$	ODF_3	ODF_2	ODF_2	ODF_2	ODF_2
$3rd$	ODF_{16}	ODF_{65}	ODF_{65}	ODF_{65}	ODF_{75}
$4th$	ODF_{30}	ODF_{66}	ODF_{66}	ODF_{64}	ODF_{73}
$5th$	ODF_{32}	ODF_{64}	ODF_{64}	ODF_{66}	ODF_{65}
$6th$	ODF_{57}	ODF_{70}	ODF_{70}	ODF_{70}	ODF_{72}
$7th$	ODF_{60}	ODF_{72}	ODF_{72}	ODF_{16}	ODF_{64}
$8th$	ODF_{64}	ODF_{30}	ODF_{30}	ODF_{72}	ODF_{70}
$9th$	ODF_{65}	ODF_{10}	ODF_{10}	ODF_{75}	ODF_{16}
$10th$	ODF_{66}	ODF_{24}	ODF_{24}	ODF_{44}	ODF_{66}
...	...	...	...	...	...

from each of the methods, for the objective function F_4. Top 10 features with the highest ranks are shown but in practice the whole list of 76 ODFs is obtained. It is normally observed that different methods produce a different ranking, since they look at the same data from different mathematical angles and with different evaluation metrics, however we do observe consistency in the results. As we proceed to the next step of feature reduction, we can only take one final ranking, which is decided by a voting (majority wins) among the five methods. The final ranking will determine the searching order in the next step.

Global optimization. With ordered variables we can conduct a standard optimization. Global optimization algorithms find the best value with the number of variables varying from 1 to 76, following the order of importance. At iteration k, while the k-th variable from the rank is being fixed by the algorithm, the top $k-1$ variables have already had values fixed, and the remaining $76-k$ are temporarily set to zero. The iteration stops when adding a variable does not improve the best value obtained. In terms of global optimization algorithms, linear programming is used for linear functions F_1 and F_2. For nonlinear functions F_3, F_4 and F_5, genetic algorithm is used. Both algorithms allow specifying the constraints, lower and upper bounds, of input variables.

4.5.2 Optimization results

Three criteria are used to evaluate the material structural design methods: the goodness of properties obtained, the efficiency of search, and the completeness of solutions. Since in this context we are dealing with design problems that optimize certain defined property functions, the goodness of method can be determined by the sheer value of the property obtained. The efficiency is judged by the time taken for obtaining the result under the same computational environment. In some cases, there exist multiple solutions of structure that produce the same best property, and we evaluate the completeness of solutions by the number of answers generated. The best solution would be the one that finds the most number of (if there exists more than one) desired optimum result within the shortest time. In this section, we first present directly the optimum results for each problem gained by our data mining method as well as how each solution is structured (single solution or multiple solutions, single-crystalline or poly-crystalline). For any of them to make sense, we compare both the results and the running time with some baseline searching methods as well as advanced optimization methods. Subsequent discussions and analyses are provided.

The minimum of Young Modulus (E^{opt}) obtained is 85.9878 GPa, given by a single-crystal microstructure with $\mathcal{A}(34) = 265.8581$ and the other variables zero. Fig. 4.2 shows the microstructure with only one orientation of the crystal in poly-crystalline material. The maximum of Yield Stress (Y^{opt}) is 3.5311 GPa and is given by three sets of answers, two of which are single-crystal microstructures: 1) $\mathcal{A}(32) = 265.8581$ and others 0; 2) $\mathcal{A}(33) = 265.8581$ and others 0; and 3) $\mathcal{A}(32) = \mathcal{A}(33) = 132.9291$ and others 0. Fig. 4.3 shows the microstructure with only one orientation of the crystal in poly-crystalline material. The maximum of magnetostrictive strain (m^{opt}) is 1.5498e-04, given again by a single-crystal microstructure where $\mathcal{A}(32) = 265.8581$ and others all 0. Fig. 4.4 shows the microstructure. As expected for linear property we get a single crystal which for Galfenol is $< 100 >$ direction, with our data mining

search we are able to find this optimal microstructure in very less amount of time.

The optimum microstructure for objective function F_1 is also a single-crystal and ODF plots is similar to previous ODF plots. The value of F_1^{opt} is 2.9347e-06. For problem F_2, however, we get 26 microstructure which give the same maximum value of $F_2^{opt} = 10$. ODF plots for all those microstructure is shown in Fig.4.5.

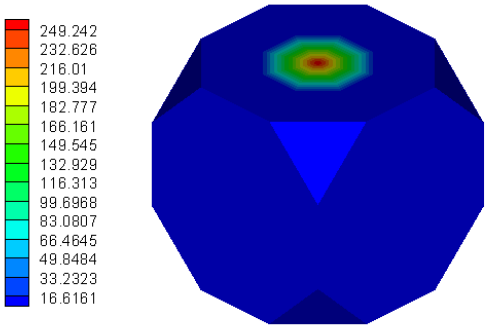

Figure 4.2: *ODF values that satisfy the Objective Function E*

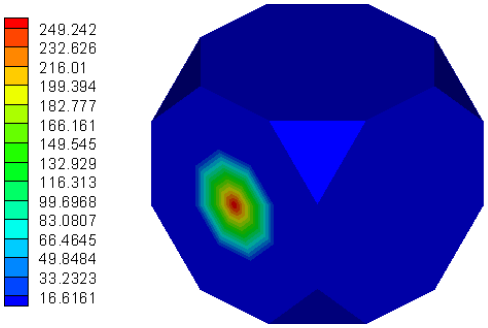

Figure 4.3: *ODF values that satisfy the Objective Function Y*

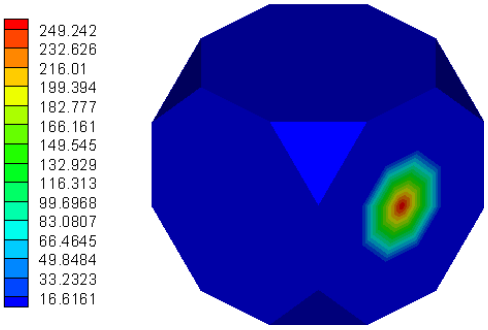

Figure 4.4: *ODF values that satisfy the Objective Function m*

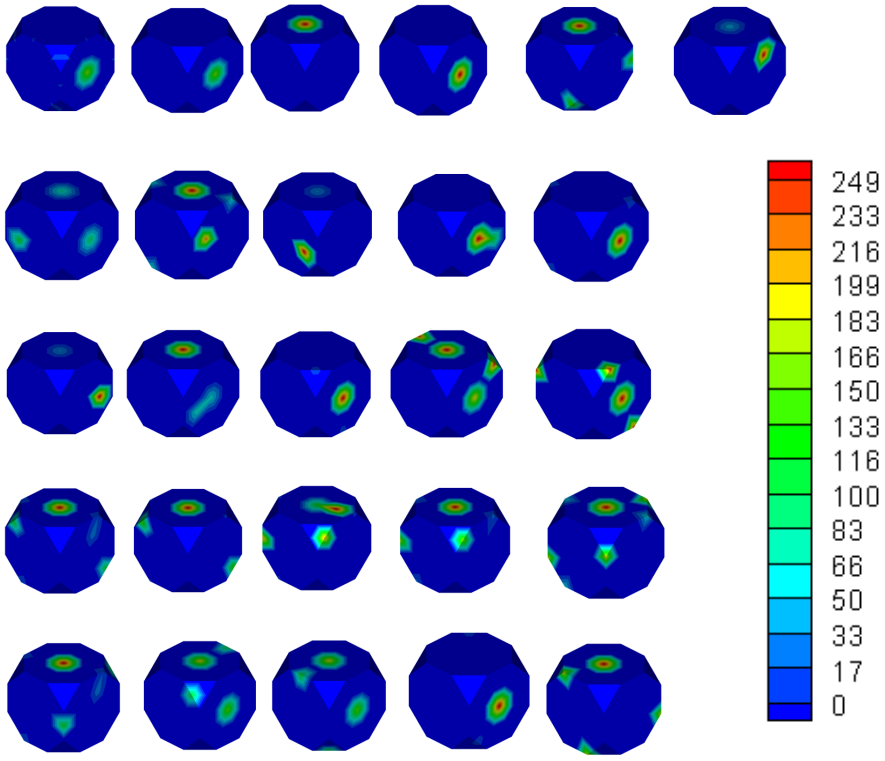

Figure 4.5: *ODF values for all 26 possible cases that satisfy the Objective Function* F_2

Table 4.2: Comparison of Optimal Value for different property

Property	Random Search	Data Mining	Genetic Algorithm
Yield Strength (Y) in GPa	0.323	0.35311	0.30654
Magnetostrictive Strain(m)	9.0034e-5	1.5498e-4	1.3797e-04
Young Modulus (E) in GPa	186.25	85.9878	89.5667

To validate the result obtained by data mining we did exhaustive search (1 million search) for Y, m and E. In table we have shown the comparison of results obtained by data mining and exhaustive search method. As we can deduce from this comparison that being linear property it's still possible to get similar optimal value for Y and m using exhaustive search. But, for non linear property such as E large number of search is still not enough to find the microstructure for which value for E is minimum. With our data mining approach we can able to find this minimum value for non linear property E in fraction of time as compared to exhaustive search method.

4.6 Conclusion

In this chapter we developed an approach for microstructure sensitive design using a data mining frame work based on feature extraction and start point recommendation.Using this data mining method we can search for microstructure that can result in optimal property in fraction of time as compared to conventional linear programming method which is generally used to solve these kinds of problems. For one of the objective function we got several combinations for microstructure which is not possible with conventional linear programming technique. In the future we will try to employ these methods for more complex problems such as finding microstructure that can results for better fatigue performance, lower hysteresis, optimal damping and numerous other properties. We will further validate these findings with series of experiments.

CHAPTER V

Microstructure modeling using statistical correlation functions

Since ODF representation does not contain information about the local neighborhood of crystals, Taylor assumption [132] is typically used where all crystals are subject to the same macroscopic strain and equilibrium across grain boundaries is not captured. In chapter 6 of the thesis, we investigate a higher order probability descriptor, the orientation correlation function (OCF), for representing polycrystalline microstructures. The OCF arises in known expressions for mechanical and transport properties [108, 22] and correlates with defect-sensitive properties such as stress corrosion cracking and creep [137]. The OCF defined by $\mathcal{F}(\boldsymbol{g}', \boldsymbol{g}, \boldsymbol{r})$, gives the probability density of finding orientations $\boldsymbol{g}'$ and $\boldsymbol{g}$ at the end points of a randomly placed vector $\boldsymbol{r}$ within the microstructure. In addition to containing volume fraction information, the OCF also contains crystal neighborhood information that can be used in models that predict interactions between grains.

Finite element representation of the two–point measure is challenging due to its high dimensionality, for example, nine–dimensional elements are needed to fully discretize the OCF for a 3D FCC polycrystal. Analytical approximations in the form of exponentially decaying functions (based on the Corson's model, Corson (1976), Garmestani et al. (2001)) have been developed for approximating the two–point prob-

ability function. More recently, Adams exploited the use of intermediate representation called 'texture functions', approximated in Fourier space (Adams et al. (2005)). However, these are global approximations and are not efficient in capturing sharp changes in the two–point probability function that occur in real microstructures. In this work, we attempt to develop a simplified finite element representation of the two–point measure using an approach analogous to 'separation of variables' method used for solving differential equations. Here, the OCF is described using interconnected layers of meshes in $\boldsymbol{g}$, $\boldsymbol{r}$ and $\boldsymbol{g}'$ spaces. The conditional orientation correlation function (COCF), $\mathcal{F}(\boldsymbol{g}'|(\boldsymbol{g},\boldsymbol{r}))$ is described using a finite element mesh in the 3D orientation space of $\boldsymbol{g}'$. This mesh is linked to a node $\boldsymbol{r}$ in a separate mesh representing the local neighborhood of orientation $\boldsymbol{g}$. As the microstructure evolves, the crystal reorientations close to an orientation ($\boldsymbol{g}$) is captured by updating probability fields in these interconnected finite element meshes. A novel total Lagrangian approach has been developed that allows evolution of probability densities while satisfying basic normalization constraints. The piecewise polynomial functions used to represent the COCF allow ease of construction of various orientation transformations, such as differencing, interpolation and projection. The improvement in prediction of texture and strains achieved by the COCF approach over ODF–based methods has been quantified through simple deformation analysis of a planar polycrystalline microstructure. For this simulation, we employ a viscoplastic (non–hardening) constitutive model and a Green's function based first order correction to the Taylor model previously developed in Adams et al. (1989).

5.1 Representation of the conditional orientation correlation function

The N-point correlation measure can be interpreted as the probability of finding the N vertices of a polyhedron separated by relative distances $x_1, x_2, ..., x_N$ in crystal orientations $\boldsymbol{g}_1, \boldsymbol{g}_2, ..., \boldsymbol{g}_N$ when tossed in the microstructure. The conditional orientation correlation function used in this work, $\mathcal{F}(\boldsymbol{g}'|(\boldsymbol{g}, \boldsymbol{r}))$, is related to the two–point descriptor ($N = 2$). The function, hereafter simply called COCF, gives the probability density of occurrence of an orientation $\boldsymbol{g}'$ at the end point of a vector $\boldsymbol{r}$ (with length r) emanating from a given orientation $\boldsymbol{g}$ (Fig. 5.1). The function satisfies the

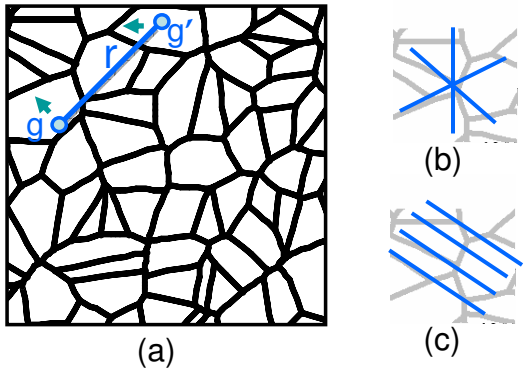

Figure 5.1: *(a) COCF ($\mathcal{F}(\boldsymbol{g}'|(\boldsymbol{g}, \boldsymbol{r}))$) gives the probability density of occurrence of an orientation $\boldsymbol{g}'$ at the end point of a vector $\boldsymbol{r}$ emanating from orientation g. (b) Sampling along all directions results in a rotationally invariant OCF with scalar r. (c) Direction sensitive sampling for a vector representation of $\boldsymbol{r}$*

following conservation equations at all times during deformation:

$$\int \mathcal{F}(\boldsymbol{g}'|(\boldsymbol{g}, \boldsymbol{r}))d\boldsymbol{g}' = 1 \tag{5.1}$$

$$\int \mathcal{F}(\boldsymbol{g}'|(\boldsymbol{g}, \boldsymbol{r}))\mathcal{P}(\boldsymbol{r}|\boldsymbol{g})d\boldsymbol{r} = \mathcal{A}(\boldsymbol{g}') \tag{5.2}$$

$$\int \mathcal{A}(\boldsymbol{g}')d\boldsymbol{g}' = 1 \tag{5.3}$$

$$\int \mathcal{P}(\boldsymbol{r}|\boldsymbol{g})d\boldsymbol{r} = 1 \tag{5.4}$$

In the above equation $\mathcal{A}(\boldsymbol{g}')$ refers to the orientation distribution function (ODF) and $\mathcal{P}(\boldsymbol{r}|\boldsymbol{g})$ gives the probability density of occurrence of vector $\boldsymbol{r}$ from a location with orientation $\boldsymbol{g}$. $\mathcal{P}(\boldsymbol{r}|\boldsymbol{g})$ is a geometrical probability distribution that accounts for the finite size of the microstructure. In the derivation of Eq. 5.2, orientations $\boldsymbol{g}'$ and $\boldsymbol{g}$ are considered mutually independent variables, with the joint probability $\mathcal{G}(\boldsymbol{g}', \boldsymbol{g}) = \mathcal{A}(\boldsymbol{g})\mathcal{A}(\boldsymbol{g}')$.

In addition, the following constraints have to be satisfied by the COCF at all times:

$$\mathcal{F}(\boldsymbol{g}'|(\boldsymbol{g}, r=0)) = \delta(\boldsymbol{g}-\boldsymbol{g}') \tag{5.5}$$

$$\mathcal{F}(\boldsymbol{g}'|(\boldsymbol{g}, \boldsymbol{r})) \geq 0 \text{ (with } \mathcal{P}(\boldsymbol{r}|\boldsymbol{g}) \geq 0, \mathcal{A}(\boldsymbol{g}') \geq 0) \tag{5.6}$$

Here, δ stands for the dirac delta function. The distance r can be considered a scalar (using the notion of rotational invariance). Note that the correlation functions may also depend on the direction of r, in which case, parameter r must be considered as a vector. Use of scalar r simplifies the computational cost but captures less information about the polycrystal. We will discuss both cases in this work. In addition to the above constraints, the orientation space corresponding to all possible $\boldsymbol{g}$'s must satisfy the crystallographic symmetries of the chosen system (FCC, HCP etc.) and the switching symmetry of the two–point measure.

Previously, analytical approximations (Garmestani et al. (2001)) have been used to represent *discrete* two–point probability functions. For example, exponential functions in the following form can be used to represent the conditional two–point probability function for a discrete set of orientations $\boldsymbol{g}$:

$$P(g_j|(g_i, r)) = \begin{cases} V_j + (1-V_j)exp(-c_{ij}r^{n_{ij}}) & \text{if } i = j; \\ V_j - V_j exp(-c_{ij}r^{n_{ij}}) & \text{if } i \neq j. \end{cases} \tag{5.7}$$

where, V_j is the volume fraction of grains with orientations $\boldsymbol{g}_j$. The parameters c_{ij} and n_{ij} are obtained by curve fitting the measured initial COCF. The above relationship is a smooth global approximation and is not efficient in capturing localized changes (at different $\boldsymbol{r}$) in the two–point probability function that occur in real microstructures. In this paper, we develop a new finite element discretization approach for representing the orientation correlation function. In this section, we first explain the representation scheme for the COCF using a *continuous* domain of orientations $\boldsymbol{g}$, i.e., the orientation space.

The complete orientation space of a polycrystal can be reduced to a smaller subset, called the fundamental region, as a consequence of crystal symmetries. Within the fundamental region, each crystal orientation is represented uniquely by a coordinate $\boldsymbol{g}$, the parametrization for the rotation (eg. Euler angles, Rodrigues vector etc.). The ODF, represented by $\mathcal{A}(\boldsymbol{g})$, describes the local density of crystals over the fundamental region of orientation space. Consider a region R_δ which is a ball of radius δ centered at orientation $\boldsymbol{g}$ in the fundamental region. Let $v_f(R_\delta)$ be the volume fraction of crystals that have orientations that occur within volume R_δ. Assuming that the ODF is a continuous function in the fundamental region, the ODF at an orientation $\boldsymbol{g}$ is defined as:

$$\mathcal{A}(\boldsymbol{g}) = \lim_{\delta \to 0} \frac{v_f(R_\delta)}{\int_{R_\delta} d\boldsymbol{g}} \tag{5.8}$$

A variety of ODF representation techniques have been developed in literature, including spectral expansions and finite element representations. We employ the finite element approach where the ODF is represented through the nodal values of a finite element grid in the fundamental region (eg. g–mesh in Fig. 5.2).

The COCF, $\mathcal{F}(\boldsymbol{g}'|(\boldsymbol{g}, r))$, is represented in the FE discretized fundamental region (called mesh $M_{g'|gr}$). Another mesh (mesh $M_{r|g}$) in real space is considered that contains all possible distances (r) from an orientation $\boldsymbol{g}$. This is a 1D mesh if only scalar magnitudes of r is considered and a nD mesh in a general case if n-dimensional

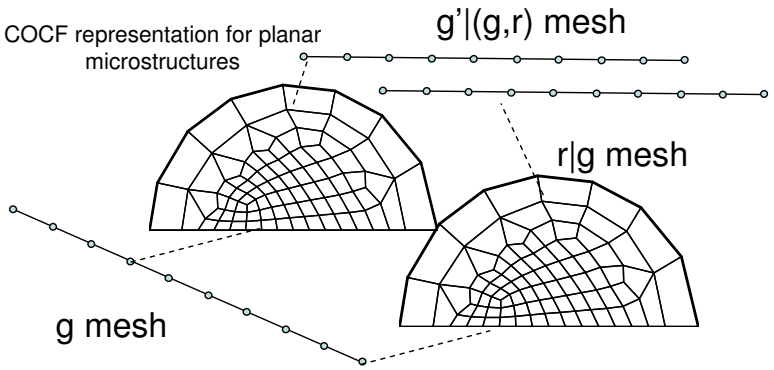

Figure 5.2: *COCF mesh representation for a planar microstructure (with fundamental region being a line between $-\pi/2$ to $\pi/2$). The $\boldsymbol{r}$ mesh is a semicircle with each node point giving the distance and orientation of a vector $\boldsymbol{r}$ drawn from orientation $\boldsymbol{g}$. Orientation $\boldsymbol{g}'$ located at the end of vector $\boldsymbol{r}$ is represented using a fundamental region connected to each node in the $\boldsymbol{r}$ mesh.*

($n = 2, 3$) vector locations $\boldsymbol{r}$ are considered. The mesh $M_{g'|gr}$ is represented at every node point in mesh $M_{r|g}$. The mesh $M_{r|g}$ is, in turn, defined for every node point in another FE discretized fundamental region (mesh M_g). The approach is illustrated in Fig. 5.2 for a planar microstructure (with fundamental region for $\boldsymbol{g}$ being a line between $-\pi/2$ to $\pi/2$). The approach used here allows easy visualization and interpretation of COCF evolution during deformation.

5.2 Probability update in finite element spaces

The probabilities are evolved from time $t = 0$ from an initial COCF that satisfies the conservation equations 5.1–5.4. The initial orientation $\boldsymbol{g}_o$ of a crystal reorients during deformation and maps to a new orientation $\boldsymbol{g}_t$ at time t. Simultaneously, the finite element mesh of fundamental region M_g deforms with nodes located at $\boldsymbol{g}_o$ moving to new locations $\boldsymbol{g}_t$. We assume that the mapping from $\boldsymbol{g}_o$ to $\boldsymbol{g}_t$ is invertible.

The ODF $\mathcal{A}(\boldsymbol{g}_t)$ represents the volume density of crystals with orientation $\boldsymbol{g}_t$ at time t. The evolution of ODF is given by the conservation equation 5.3 as:

$$\int \mathcal{A}(\boldsymbol{g}_o, t=0) d\boldsymbol{g}_o = \int \mathcal{A}(\boldsymbol{g}_t) d\boldsymbol{g}_t = 1 \tag{5.9}$$

where $d\boldsymbol{g}_o$ represents the volume element in the undeformed (initial) ODF mesh (M_{g_o}) which becomes volume element $d\boldsymbol{g}_t$ at time t. A Jacobian $J(\boldsymbol{g}_o, t) = \det(\boldsymbol{F})$ gives the ratio of elemental volumes, where $\boldsymbol{F}$ is the reorientation gradient given as $\boldsymbol{F}(\boldsymbol{g}_o, t) = \frac{\partial \boldsymbol{g}_t}{\partial \boldsymbol{g}_o}$. Using the Jacobian, a map of the current mesh (at time t) to the reference mesh (at $t = 0$) can be made:

$$\int (\mathcal{A}(\boldsymbol{g}_o, t=0) - \hat{\mathcal{A}}(\boldsymbol{g}_o, t) J(\boldsymbol{g}_o, t)) d\boldsymbol{g}_o = 0 \tag{5.10}$$

The quantity written as $\hat{\mathcal{A}}(\boldsymbol{g}_o, t)$ is the volume density $\mathcal{A}(\boldsymbol{g}_t)$ plotted over the corresponding orientation ($\boldsymbol{g}_o$) in the initial mesh. Thus, $\hat{\mathcal{A}}(\boldsymbol{g}_o, t)$ gives the Lagrangian representation of the current ODF in the initial mesh M_{g_o}. If the integrand is continuous, a localized relationship of the following form can be used to update the ODF at any time t:

$$\hat{\mathcal{A}}(\boldsymbol{g}_o, t) J(\boldsymbol{g}_o, t) = \mathcal{A}(\boldsymbol{g}_o, t=0) \tag{5.11}$$

For computing $\boldsymbol{g}_t$, a reorientation velocity (computed from the constitutive model) $\boldsymbol{v} = \frac{\partial \boldsymbol{g}_t}{\partial t}$ is used. The reorientation velocity is computed at each nodal point in the mesh and the change in orientation $\Delta \boldsymbol{g}' = \boldsymbol{g}'_t - \boldsymbol{g}'_o$ is then stored at the nodal points in the fundamental region. Fig. 5.3 gives an idea of how the approach works for a one–dimensional fundamental region that is represented using two–noded finite elements with linear interpolation. Here, the Jacobian is simply the ratio of element lengths, i.e. current length divided by the initial length. If the element length decreases over time, the probability density has to increase based on Eq. 5.11 to maintain normalization of the ODF.

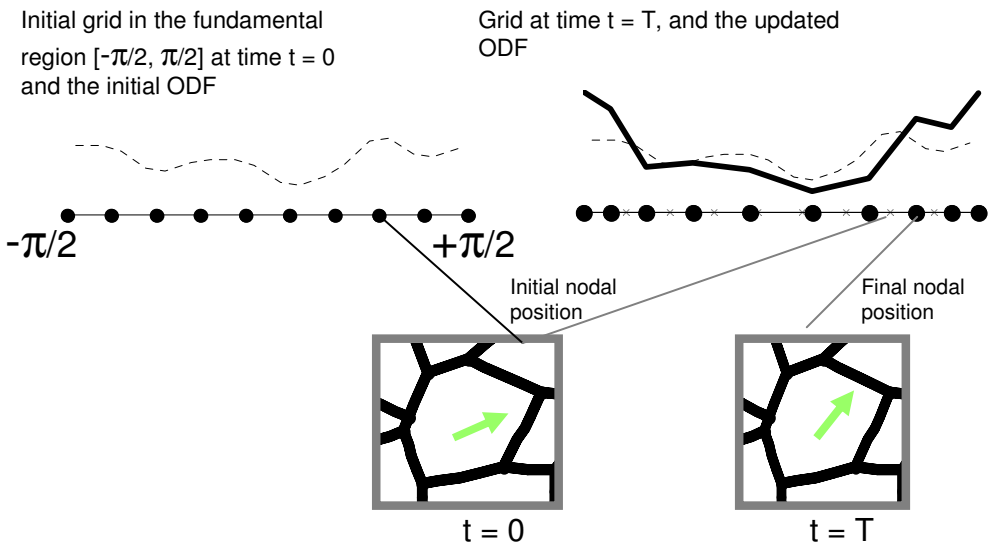

Figure 5.3: *Probability update scheme in FE space: During deformation, the nodal points ($\boldsymbol{g}$) of the FE mesh are moved to reflect reorientation ($\Delta\boldsymbol{g}$) of crystals. The new ODF is obtained using Eq. 5.11 that ensures that the normalization constraint (Eq. 5.9) is met in the reoriented mesh.*

Note that the integrand in Eq. 5.10 needs to be continuous for the localization relationship to be valid. Thus, it is implied that $J(\boldsymbol{g}_o, t)$ needs to be continuous and consequently, $\boldsymbol{v}$ needs to be continuously differentiable (at least piecewise) in the fundamental region. The latter is rather a restriction on the constitutive model and macro–micro linking assumption that is used to compute $\boldsymbol{v}$.[1] Note that the differentiability of $\boldsymbol{v}$ will also ensure invertibility of the map from $\boldsymbol{g}_o$ to $\boldsymbol{g}_t$.

Similar approach is used to update the probability densities $\mathcal{P}$ and $\mathcal{F}$ in the meshes $M_{r|g}$ and $M_{g'|gr}$ respectively. The evolution of geometrical probability density $\mathcal{P}$ is given by conservation equation 5.4 as:

$$\int (\hat{\mathcal{P}}(\boldsymbol{r}_o, t|\boldsymbol{g}_t) J(\boldsymbol{r}_o, t|\boldsymbol{g}_t) - \mathcal{P}(\boldsymbol{r}_o, t=0|\boldsymbol{g}_t)) d\boldsymbol{r}_{o_g} = 0 \tag{5.12}$$

where $d\boldsymbol{r}_{o_g}$ represents the volume element in the undeformed (initial) mesh ($M_{r|g}$) and

[1] Some rate-independent crystal plasticity models give sharp differences in reorientation velocities for orientations that are, in fact, very close to each other. When using such models, the Jacobian may become ill–defined.

$J(\boldsymbol{r}_o, t|\boldsymbol{g}_t) = \det(\frac{\partial \boldsymbol{r}_t}{\partial \boldsymbol{r}_o}(\boldsymbol{g}_t))$ is the Jacobian for a volume element initially at location $\boldsymbol{r}_o$ from orientation $\boldsymbol{g}_t$. A localized relation of the following form is used to compute the geometrical probability density at time t:

$$\hat{\mathcal{P}}(\boldsymbol{r}_o, t|\boldsymbol{g}_t) J(\boldsymbol{r}_o, t|\boldsymbol{g}_t) = \mathcal{P}(\boldsymbol{r}_o, t = 0|\boldsymbol{g}_t) \tag{5.13}$$

We consider the microstructure to be periodic, in which case, the initial probability $\mathcal{P}(\boldsymbol{r}_o, t = 0|\boldsymbol{g}) = c_o$, a constant independent of $\boldsymbol{g}$. That is, from a given crystal, all r–vectors are equally probable due to periodicity.

For computing the COCF, we first look at the r–interdependence (Eq. 5.2):

$$\int \mathcal{F}(\boldsymbol{g}_t^{'}|(\boldsymbol{g}_t, \boldsymbol{r}_t)) \mathcal{P}(\boldsymbol{r}_t|\boldsymbol{g}_t) d\boldsymbol{r}_t = A(\boldsymbol{g}_t^{'}) \tag{5.14}$$

The two localization relations given by Eq. 5.11 and Eq. 5.13 are used to reduce the above equation:

$$\int \hat{\mathcal{F}}(\boldsymbol{g}_t^{'}|(\boldsymbol{g}_t, \boldsymbol{r}_o, t)) \frac{\mathcal{P}(\boldsymbol{r}_o, t = 0|\boldsymbol{g}_t)}{J(\boldsymbol{r}_o, t|\boldsymbol{g}_t)} J(\boldsymbol{r}_o, t) d\boldsymbol{r}_o = \frac{\mathcal{A}(\boldsymbol{g}_o^{'}, t = 0)}{J(\boldsymbol{g}_o^{'}, t)} \tag{5.15}$$

$$= \frac{1}{J(\boldsymbol{g}_o^{'}, t)} \int \mathcal{F}(\boldsymbol{g}_o^{'}, t = 0|(\boldsymbol{g}_o, \boldsymbol{r}_o)) \quad \mathcal{P} \quad (\boldsymbol{r}_o, t = 0|\boldsymbol{g}_o) d\boldsymbol{r}_o \tag{5.16}$$

$$\int c_o(\hat{\mathcal{F}}(\boldsymbol{g}_t^{'}|(\boldsymbol{g}_t, \boldsymbol{r}_o, t)) \frac{J(\boldsymbol{g}_o^{'}, t) J(\boldsymbol{r}_o, t)}{J(\boldsymbol{r}_o, t|\boldsymbol{g}_t)} \quad - \quad \mathcal{F}(\boldsymbol{g}_o^{'}, t = 0|(\boldsymbol{g}_o, \boldsymbol{r}_o))) d\boldsymbol{r}_o = 0 \tag{5.17}$$

In the above derivation, we have used the fact that $\mathcal{P}(\boldsymbol{r}_o, t = 0|\boldsymbol{g}) = c_o$ at time t = 0 due to periodicity. The localization relationship obtained from Eq. 5.17 leads to a simple probability update strategy for the COCF:

$$\hat{\mathcal{F}}(\boldsymbol{g}_t^{'}|(\boldsymbol{g}_t, \boldsymbol{r}_o, t)) \frac{J(\boldsymbol{g}_o^{'}, t) J(\boldsymbol{r}_o, t)}{J(\boldsymbol{r}_o, t|\boldsymbol{g}_t)} = \mathcal{F}(\boldsymbol{g}_o^{'}, t = 0|(\boldsymbol{g}_o, \boldsymbol{r}_o)) \tag{5.18}$$

The above equation gives the COCF in locations $(\boldsymbol{g}_t, \boldsymbol{r}_t)$ for all times $t > 0$. Finally, we need to develop a mesh update strategy that ensures the normalization

equation for COCF ($\mathcal{F}$) (Eq 5.1) is satisfied at times $t > 0$:

$$\int \mathcal{F}(\boldsymbol{g}_t^{'}|(\boldsymbol{r}_t, \boldsymbol{g}_t))d\boldsymbol{g}_{t_{rg}}^{'} = 1 \tag{5.19}$$

where $d\boldsymbol{g}_{t_{rg}}^{'}$ represents the volume element at orientation $\boldsymbol{g}_t^{'}$ in the deformed COCF mesh ($M_{g'|gr}$) located at a distance of $\boldsymbol{r}_t$ from $\boldsymbol{g}_t$.

Using Eq. 5.18, the conservation equation is written as:

$$\int \mathcal{F}(\boldsymbol{g}_o^{'}, t=0|(\boldsymbol{g}_o, \boldsymbol{r}_o))\frac{J(\boldsymbol{r}_o, t|\boldsymbol{g}_t)}{J(\boldsymbol{g}_o^{'}, t)J(\boldsymbol{r}_o, t)}d\boldsymbol{g}_{t_{rg}}^{'} = \int \mathcal{F}(\boldsymbol{g}_o^{'}, t=0|(\boldsymbol{g}_o, \boldsymbol{r}_o))d\boldsymbol{g}_{o_{rg}}^{'} = 1 \tag{5.20}$$

By inspection of the above equation, the Jacobian for the COCF mesh evolution can be obtained as:

$$J(\boldsymbol{g}_o^{'}, t|(\boldsymbol{r}_t, \boldsymbol{g}_t)) \;=\; \det(\frac{\partial \boldsymbol{g}_t^{'}}{\partial \boldsymbol{g}_o^{'}}(\boldsymbol{r}_t, \boldsymbol{g}_t)) = \frac{J(\boldsymbol{g}_o^{'}, t)J(\boldsymbol{r}_o, t)}{J(\boldsymbol{r}_o, t|\boldsymbol{g}_t)} \tag{5.21}$$

The initial COCF mesh (at $t = 0$) is the same at all locations $\boldsymbol{r}$ and $J(\boldsymbol{g}_o^{'}, t|(\boldsymbol{r}_o, \boldsymbol{g}_t))$ is also numerically equal to the above Jacobian. This equation gives a mesh update strategy for the COCF. As explained previously, ODF mesh update uses the reorientation gradient $\boldsymbol{F}(\boldsymbol{g}_o^{'}, t) = \frac{\partial \boldsymbol{g}_t}{\partial \boldsymbol{g}_o}$ computed from the reorientation velocity $\boldsymbol{v} = \frac{\partial \boldsymbol{g}_t}{\partial t}$ (as given by the constitutive model). At each location $\boldsymbol{r}_t$ and $\boldsymbol{g}$, the node points of the COCF mesh ($M_{g'|gr}$) are moved using the same reorientation gradient (with Jacobian $J(\boldsymbol{g}_o^{'}, t)$) but scaled by a factor $(\frac{J(\boldsymbol{r}_o, t)}{J(\boldsymbol{r}_o, t|\boldsymbol{g}_t)})^{\frac{1}{d}}$, where d is the dimensionality of the orientation space. We next look at the approach to compute this scaling factor.

Apart from crystal reorientations, the COCF also evolves due to stretching of grains during deformation (Fig 5.4). Let us say, for now, that the velocity gradient ($\boldsymbol{L}$) for each grain of orientation $\boldsymbol{g}$ can be computed (this is discussed later in section 5.3.1). In Fig. 5.4, the rate of change of vector $\boldsymbol{r}$ originating from orientation $\boldsymbol{g}$ (shown as a red line) can be found by integrating $\boldsymbol{L}d\boldsymbol{r}$ over the vector $\boldsymbol{r}$. However,

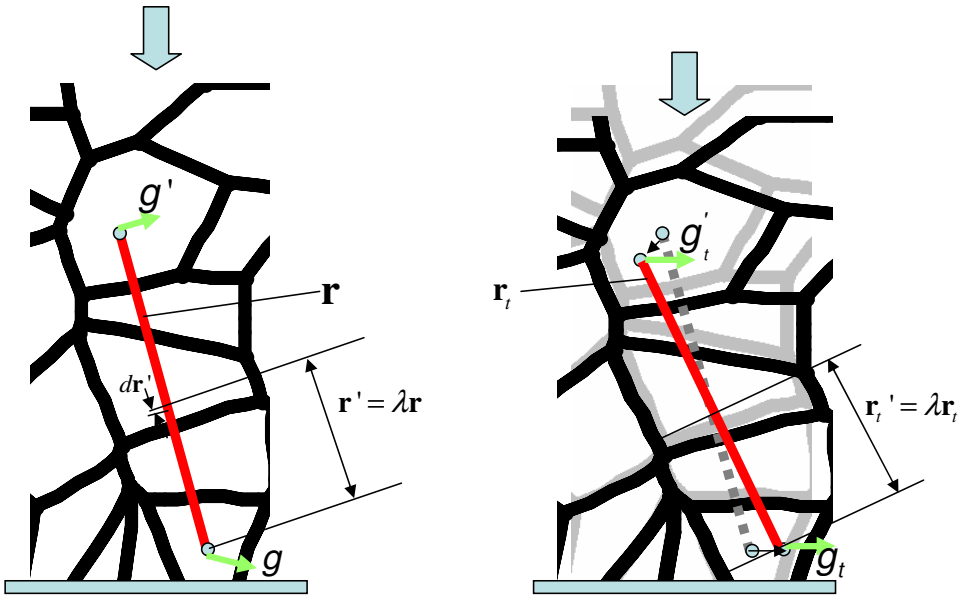

Figure 5.4: *During deformation, the two–point descriptor evolves due to reorientation of crystals with initial orientation* $\boldsymbol{g}'$ *and* $\boldsymbol{g}$ *at the end points of vector* $\boldsymbol{r}$*. In addition, both the length and orientation of* $\boldsymbol{r}$ *vector changes during deformation.*

in the COCF approach, the velocity gradient $\boldsymbol{L}$ along the vector $\boldsymbol{r}$ is only known in a statistical sense. For eg. the average velocity gradient at a distance of $\boldsymbol{r}'$ ($\boldsymbol{r}' = \lambda \boldsymbol{r}$, $0 \leq \lambda \leq 1$) from orientation $\boldsymbol{g}$, denoted as $< \boldsymbol{L}(\boldsymbol{r}'|\boldsymbol{g}) >$, can be found by averaging over the COCF:

$$< \boldsymbol{L}(\boldsymbol{r}'|\boldsymbol{g}) >= \int \mathcal{F}(\boldsymbol{g}'|(\boldsymbol{g}, \boldsymbol{r}'))L(\boldsymbol{g}')d\boldsymbol{g}'_{r'g} \tag{5.22}$$

The average rate of change of vector $\boldsymbol{r}$ can then be written as a path integral of averaged velocity gradient ($< \boldsymbol{L}(\boldsymbol{r}'|\boldsymbol{g}) >$) along $\boldsymbol{r}$:

$$< \dot{\boldsymbol{r}} >_{\boldsymbol{g}} = \int_0^{\boldsymbol{r}} < \boldsymbol{L}(\boldsymbol{r}'|\boldsymbol{g}) > d\boldsymbol{r}'_g \tag{5.23}$$

Nodes in the mesh $M_{r|g}$ are updated using the velocities computed in Eq. 5.23 from which the Jacobian $J(\boldsymbol{r}_o, t|\boldsymbol{g})$ can be computed. The probability $\mathcal{P}(\boldsymbol{r}_t)$ is computed

from the relationship:

$$\int \mathcal{P}(\boldsymbol{r}_t|\boldsymbol{g}_t)\mathcal{A}(\boldsymbol{g}_t)d\boldsymbol{g}_t = \mathcal{P}(\boldsymbol{r}_t) \tag{5.24}$$

Then, the Jacobian is computed as $J(\boldsymbol{r}_o, t) = \frac{\mathcal{P}(\boldsymbol{r}_o)}{\mathcal{P}(\boldsymbol{r}_t)}$.

5.2.1 Case of rotationally invariant COCF:

When using the *rotationally invariant* COCF, only the rate of change of *magnitude* of $\boldsymbol{r}$ needs to be calculated. The vector $\boldsymbol{r'}$ is written as a product of the magnitude r' and a unit vector $\boldsymbol{n}$ (ie. $\boldsymbol{r'} = r'\boldsymbol{n}$). Eq. 5.23 is rewritten in terms of the stretch rate tensor $< \boldsymbol{D} >$ (symmetric part of $< \boldsymbol{L} >$) and another integral is performed over the surface of a unit sphere in order to average over all possible unit vectors $\boldsymbol{n}$.

$$< \dot{r} >_{\boldsymbol{g}} = \int \left[\int_0^r \boldsymbol{n}^T < \boldsymbol{D}(\boldsymbol{n}r'|\boldsymbol{g}) > \boldsymbol{n} dr_g^{'} \right] d\boldsymbol{n} \tag{5.25}$$

The average velocity gradient is computed from the rotationally invariant COCF as follows:

$$< \boldsymbol{L}(\boldsymbol{n}r^{'}|\boldsymbol{g}) > = \int \mathcal{F}(\boldsymbol{g'}|(\boldsymbol{g}, r'))L(\boldsymbol{g'})d\boldsymbol{g}'_{r'g} \tag{5.26}$$

The right hand side of the above expression is clearly independent of $\boldsymbol{n}$ due to the use of rotationally invariant COCF (ie. $< \boldsymbol{L}(\boldsymbol{n}r'|\boldsymbol{g}) > = < \boldsymbol{L}(r'|g) >$). Thus, Eq. 5.25 can be rewritten as follows:

$$< \dot{r} >_{\boldsymbol{g}} = \left[\int_0^r < \boldsymbol{D}(r'|\boldsymbol{g}) > dr_g^{'} \right] \left[\int \boldsymbol{n}^T \boldsymbol{n} d\boldsymbol{n} \right] \tag{5.27}$$

Using the property $\int \boldsymbol{n}^T \boldsymbol{n} d\boldsymbol{n} = \frac{1}{3}\delta_{ij}$, we can rewrite Eq. 5.27 as:

$$< \dot{r} >_{\boldsymbol{g}} = \frac{1}{3} \int_0^r trace(< \boldsymbol{D}(r'|\boldsymbol{g}) >) dr_g^{'} \tag{5.28}$$

Note that the velocity $< \dot{r} >_{\boldsymbol{g}}$ will be zero in viscoplastic analysis due to the incompressibility constraint $trace(< \boldsymbol{D} >) = 0$.

Remark: Note that the rate of change of r–vector between two orientations ($\boldsymbol{g}$ and $\boldsymbol{g'}$) can be accurately computed if conditional three–point probability functions are known (Adams et al. (1989)):

$$< \boldsymbol{L}(\boldsymbol{r'}|(\boldsymbol{g'}, \boldsymbol{g}, \boldsymbol{r})) >= \int \mathcal{F}(\boldsymbol{g''}|(\boldsymbol{g'}, \boldsymbol{g}, \boldsymbol{r}, \boldsymbol{r'}))L(\boldsymbol{g''})d\boldsymbol{g}''_{g'gr'r} \tag{5.29}$$

$$< \dot{\boldsymbol{r}} >_{(\boldsymbol{g},\boldsymbol{g'})}= \int_0^{\boldsymbol{r}} < \boldsymbol{L}(\boldsymbol{r'}|(\boldsymbol{g'}, \boldsymbol{g}, \boldsymbol{r})) > d\boldsymbol{r}'_{g'gr} \tag{5.30}$$

where $\mathcal{F}(\boldsymbol{g''}|(\boldsymbol{g'}, \boldsymbol{g}, \boldsymbol{r}, \boldsymbol{r'}))$ is the probability of orientation $\boldsymbol{g''}$ at a distance $\boldsymbol{r'} = \lambda \boldsymbol{r}$ from orientation $\boldsymbol{g}$ given that orientation $\boldsymbol{g'}$ is at a distance of $\boldsymbol{r}$ from $\boldsymbol{g}$. Here, the rate of change $< \dot{\boldsymbol{r}} >$ is assumed to depend on both $\boldsymbol{g}$ and $\boldsymbol{g'}$. In the current work, we compute the rate of change $< \dot{\boldsymbol{r}} >$ using only the starting orientation $\boldsymbol{g}$. This is based on our Bayesian separation of variables: $\mathcal{F}(\boldsymbol{g}, \boldsymbol{g'}, \boldsymbol{r}) = \mathcal{F}(\boldsymbol{g'}|(\boldsymbol{g}, \boldsymbol{r}))\mathcal{P}(\boldsymbol{r}|\boldsymbol{g})\mathcal{A}(\boldsymbol{g})$. In the second term ($\mathcal{P}(\boldsymbol{r}|\boldsymbol{g})$), the deformation of r-mesh is modeled to depend only on the starting orientation $\boldsymbol{g}$. Our motivation here was to restrict ourselves to the known two–point probability function and avoid computing or storing the even more complex three–point probability function. In another paper (Garmestani et al. (2001)), the three–point probability function was approximated using the known two–point probability functions, but the approximation violated the normalization relationships for the three–point probability function. Derivation of consistent approximations are the subject of recent research (Mikdam et al. (2009)).

5.2.2 Symmetry constraints in the COCF

Since $\boldsymbol{g}$ and $\boldsymbol{g'}$ can be switched in the joint distribution ($\mathcal{F}(\boldsymbol{g}, \boldsymbol{g'}, \boldsymbol{r})$) without change in the probability density, a symmetry relationship of the following form is obtained:

$$\mathcal{F}(\boldsymbol{g}|(\boldsymbol{g}',\boldsymbol{r}))\mathcal{P}(\boldsymbol{r}|\boldsymbol{g}')\mathcal{A}(\boldsymbol{g}') = \mathcal{F}(\boldsymbol{g}'|(\boldsymbol{g},\boldsymbol{r}))\mathcal{P}(\boldsymbol{r}|\boldsymbol{g})\mathcal{A}(\boldsymbol{g}) \tag{5.31}$$

Substituting the localized Lagrangian conservation relationships in the above relationship leads to the following equation:

$$\frac{\mathcal{F}(\boldsymbol{g}_o, t=0|(\boldsymbol{g}_o^{'},\boldsymbol{r}_o))}{J(\boldsymbol{g}_o,t|(\boldsymbol{g}',\boldsymbol{r}))}\frac{\mathcal{P}(\boldsymbol{r}_o,t=0|\boldsymbol{g}')}{J(\boldsymbol{r}_o,t|\boldsymbol{g}')}\frac{\mathcal{A}(\boldsymbol{g}_o^{'})}{J(\boldsymbol{g}_o^{'},t)} = \frac{\mathcal{F}(\boldsymbol{g}_o^{'}, t=0|(\boldsymbol{g}_o,\boldsymbol{r}_o))}{J(\boldsymbol{g}_o^{'},t|(\boldsymbol{g},\boldsymbol{r}))}\frac{\mathcal{P}(\boldsymbol{r}_o,t=0|\boldsymbol{g})}{J(\boldsymbol{r}_o,t|\boldsymbol{g})}\frac{\mathcal{A}(\boldsymbol{g}_o)}{J(\boldsymbol{g}_o,t)} \tag{5.32}$$

Using the definition for Jacobian of COCF (Eq. 5.18) and the fact that $\mathcal{P} = c_o$ at time $t = 0$, the above equation reduces to:

$$\mathcal{F}(\boldsymbol{g}_o, t=0|(\boldsymbol{g}_o^{'},\boldsymbol{r}_o))\mathcal{A}(\boldsymbol{g}_o^{'}) = \mathcal{F}(\boldsymbol{g}_o^{'}, t=0|(\boldsymbol{g}_o,\boldsymbol{r}_o))\mathcal{A}(\boldsymbol{g}_o) \tag{5.33}$$

Note that the reference COCF sampled from the microstructure satisfies the above constraint. This indicates that the evolution of the COCF will continue to follow the symmetry constraint Eq. 5.31 when using the proposed probability update scheme.

5.3 Constitutive modeling

The OCF evolution of a viscoplastic polycrystal is calculated using the following constitutive model (Asaro and Needleman (1985)). The velocity gradient of a crystal with orientation, $\boldsymbol{g}$ (and rotation matrix $\boldsymbol{R}$) is taken to be of the following form:

$$\boldsymbol{L}(\boldsymbol{g}) = \boldsymbol{\Omega} + \boldsymbol{R}\sum_{\alpha}\dot{\gamma}^{\alpha}\acute{\boldsymbol{S}}^{\alpha}\boldsymbol{R}^{T} \tag{5.34}$$

where $\boldsymbol{\Omega}$ is the lattice spin, $\dot{\gamma}^{\alpha}$ is the shearing rate along the slip system α and $\acute{\boldsymbol{S}}^{\alpha}$ is the Schmid tensor for the slip system α, given by $(\acute{\boldsymbol{m}}^{\alpha} \otimes \acute{\boldsymbol{n}}^{\alpha})$, where $\acute{\boldsymbol{m}}^{\alpha}$ is the

slip direction and $\acute{\boldsymbol{n}}^{\alpha}$ is the slip plane normal, both in the crystal lattice frame. The expressions for the spin and symmetric parts are obtained as shown below:

$$\boldsymbol{\Omega} \;=\; \boldsymbol{W} \;-\; \boldsymbol{R}\sum_{\alpha}\dot{\gamma}^{\alpha}\acute{\boldsymbol{Q}}^{\alpha}\boldsymbol{R}^{T} \tag{5.35}$$

$$\acute{\boldsymbol{D}} \;=\; \sum_{\alpha}\dot{\gamma}^{\alpha}\;\acute{\boldsymbol{P}}^{\alpha} \tag{5.36}$$

where $\acute{\boldsymbol{P}}^{\alpha}$ and $\acute{\boldsymbol{Q}}^{\alpha}$ are the symmetric and skew parts of the Schmid tensor respectively and $\acute{\boldsymbol{D}}$ is the deviatoric deformation rate expressed in the lattice frame through, $\acute{\boldsymbol{D}} \;=\; \boldsymbol{R}^{T}\boldsymbol{D}\boldsymbol{R}$. The shearing rate on slip systems is given by a power law and we further assume that all slip systems have identical slip system resistance.

$$\dot{\gamma}^{\alpha} \;=\; \dot{\gamma}^{0}\left|\frac{\tau^{\alpha}}{s}\right|^{1/m} sign\left(\frac{\tau^{\alpha}}{s}\right) \tag{5.37}$$

where s is the slip system resistance, m is the strain rate sensitivity, $\dot{\gamma}^{0}$ is a reference rate of shearing and τ^{α} is the resolved shear stress on slip system α. Further, the resolved stress is related to the deviatoric crystal Cauchy stress as

$$\tau^{\alpha} \;=\; \acute{\boldsymbol{\sigma}}\boldsymbol{\bullet}\,\acute{\boldsymbol{P}}^{\alpha} \tag{5.38}$$

If the velocity gradient for the crystal ($\boldsymbol{L}(\boldsymbol{g})$) is known, then solving the system of equations ($5.36 - 5.38$) will lead to the deviatoric crystal cauchy stress ($\acute{\boldsymbol{\sigma}}$) and the shear rate ($\dot{\gamma}^{\alpha}$). A Newton algorithm is used to find the stress for a given velocity gradient and orientation. The secant moduli (symmetric tensor $\acute{\boldsymbol{N}}$) that relates the deviatoric deformation rate to the deviatoric stress tensor (as in $\acute{\boldsymbol{\sigma}} = \acute{\boldsymbol{N}}\acute{\boldsymbol{D}}$) in the lattice frame is then computed based on Eq. 5.39. The secant moduli in the lattice frame is then rotated back to the sample reference frame to calculate $\boldsymbol{N}$.

$$\acute{N}_{ijkl} = \left[\sum_{\alpha} (\frac{\dot{\gamma}_o}{s}) |\acute{P}^{\alpha}_{rs} \acute{\sigma}_{rs}/s|^{\frac{1}{m}-1} \acute{P}^{\alpha}_{ij} \acute{P}^{\alpha}_{kl} \right]^{-1} \tag{5.39}$$

5.3.1 Interaction Law

In the following section, the interaction law is derived for a viscoplastic polycrystal following an integral equation approach (Molinari et al. (1987)). We denote by $\boldsymbol{T}$ the local Cauchy stress, $\boldsymbol{T} = \boldsymbol{\sigma} - p\boldsymbol{I}$, with $\boldsymbol{\sigma}$ representing the deviatoric cauchy stress, p representing the pressure and $\boldsymbol{I}$ being the second-order identity tensor. $\boldsymbol{N}$ refers to the secant modulus (in the sample reference frame) derived from the constitutive problem with the relationship $\boldsymbol{\sigma} = \boldsymbol{N}\boldsymbol{D} = \boldsymbol{N}\boldsymbol{L}$. Therefore, the governing equations for deformation (equilibrium equation with incompressibility constraint) in the polycrystal can be expressed as:

$$T_{ij,j} = (N_{ijkl} L_{kl})_{,j} - p_{,i} = 0 \text{ with } L_{ii} = 0 \tag{5.40}$$

A macroscopic velocity gradient $\bar{\boldsymbol{L}}$ (with $\bar{L}_{ii} = 0$) is imposed upon the aggregate. Our objective is to find out the *local* velocity gradient ($\boldsymbol{L}$) in each crystal that satisfies the above governing equation. To this end, we first decompose $\boldsymbol{N}$ as the sum of a uniform part $\bar{\boldsymbol{N}}$ and a space dependent part $\tilde{\boldsymbol{N}}$ to obtain $\boldsymbol{N} = \bar{\boldsymbol{N}} + \tilde{\boldsymbol{N}}$. The uniform part is a tensor that is constant over the microstructure. In this work, the constant tensor $\bar{\boldsymbol{N}}$ is taken as the instantaneous secant moduli of the (first order) homogenized microstructure:

$$\bar{\boldsymbol{N}} = \int \mathcal{A}(\boldsymbol{g}) \boldsymbol{N}(\bar{\boldsymbol{L}}, \boldsymbol{g}) d\boldsymbol{g} \tag{5.41}$$

Molinari et al. (1987) proposed a Green's function solution for the set of PDEs represented by Eq.(5.40) and the compatibility conditions, $L_{ii} = 0$

$$L_{ik}(\boldsymbol{r}) = \bar{L}_{ik} + \int G_{ij,kl}(\boldsymbol{r} - \boldsymbol{r}') \tilde{\sigma}_{jl}(\boldsymbol{r}') d\boldsymbol{r}' \tag{5.42}$$

Here, $G_{ij,kl}$ is the spatial Green's function that is obtained from Eqs. 5.40 (Fig. 5.5), the positions $\boldsymbol{r}$ are those computed at current time t and the fluctuation stress is given as:

$$\tilde{\sigma}_{jl}(\boldsymbol{r}') = \tilde{N}_{jlrs}(\boldsymbol{L}(\boldsymbol{r}^{'}), \boldsymbol{g}(\boldsymbol{r}^{'}))L_{rs}(\boldsymbol{r}^{'}) \tag{5.43}$$

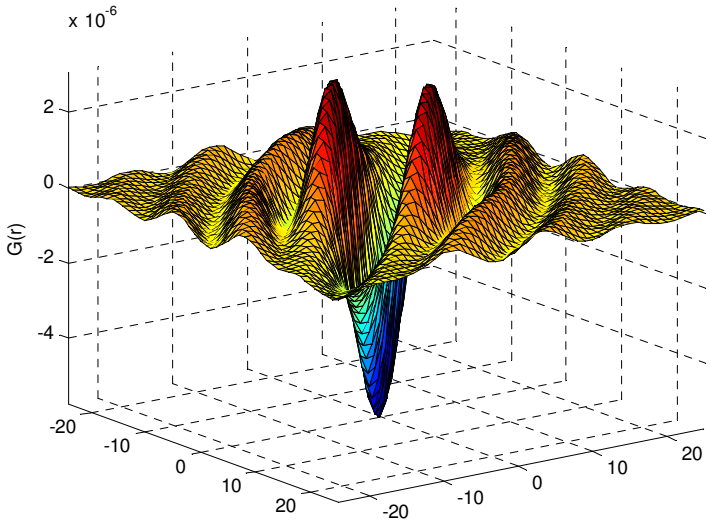

Figure 5.5: *Real part of Green's function operator* $G_{11,11}(\boldsymbol{r})$ *for a 2D microstructure. The function peaks at* $\boldsymbol{r} = (0, 0)$ *and decays to zero at large* $\boldsymbol{r}$.

Using an abbreviated form for the convolution operator, the above equation can be concisely written as:

$$\boldsymbol{L}(\boldsymbol{r}) \quad = \bar{\boldsymbol{L}} + \boldsymbol{G}(\boldsymbol{r} - \boldsymbol{r}^{'}) * \tilde{\boldsymbol{\sigma}}(\boldsymbol{r}') \tag{5.44}$$

Adams et al. (1989) developed an approach where statistical correlation functions can be used to compute this velocity gradient. When using the COCF descriptor, we assume that all grains with orientation $\boldsymbol{g}$ have one local velocity gradient that is calculated as an ensemble average. Note that there may be differences in the deformation of crystals with the same orientation but located at different positions in the microstructure. Unlike aggregate FE models, the local neighborhoods are not explicitly resolved in the COCF descriptor but are rather averaged for crystals with

orientation $\boldsymbol{g}$. Symbol $\langle\cdot\rangle_{\boldsymbol{g}}$ denotes such an ensemble average. Applying this to Eq.(5.44), the ensemble average of the local velocity gradients belonging to the same orientation $\boldsymbol{g}^*$ can be calculated (approximation is valid within the ergodic hypothesis described in Beran (1968)):

$$\begin{aligned}\boldsymbol{L}(\boldsymbol{g}^*) &= \langle \boldsymbol{L}(\boldsymbol{r})\rangle_{\boldsymbol{g}(\boldsymbol{r})=\boldsymbol{g}^*} = \bar{\boldsymbol{L}} + \boldsymbol{G}(\boldsymbol{r}-\boldsymbol{r}^{'}) * \langle \tilde{\boldsymbol{\sigma}}(\boldsymbol{r}')\rangle_{\boldsymbol{g}(\boldsymbol{r})=\boldsymbol{g}^*} \\ &= \bar{\boldsymbol{L}} + \boldsymbol{G}(\boldsymbol{r}-\boldsymbol{r}^{'}) * \left[\int \mathcal{F}(\boldsymbol{g}^{'}|(\boldsymbol{r}-\boldsymbol{r}^{'},\boldsymbol{g}^*))\tilde{\boldsymbol{\sigma}}(\boldsymbol{g}')d\boldsymbol{g}^{'}_{r'g}\right] \end{aligned} \tag{5.45}$$

This equation is non–linear since $\tilde{\boldsymbol{\sigma}}$ in itself depends on the velocity gradient (Eq. 5.43). The velocity gradient for any orientation $\boldsymbol{g}$ can be found by solving the above equation in a self–consistent iterative manner. No such iterations are required if we use a simplifying assumption that velocity gradient field does not deviate too far from the uniform field of the Taylor-type polycrystal (using a first order correction $\boldsymbol{L}(\boldsymbol{r}^{'}) \approx \bar{\boldsymbol{L}}$):

$$\langle \tilde{\boldsymbol{\sigma}}(\boldsymbol{r}')\rangle_{\boldsymbol{g}(\boldsymbol{r})=\boldsymbol{g}^*} \approx \int \mathcal{F}(\boldsymbol{g}^{'}|(\boldsymbol{r}-\boldsymbol{r}^{'},\boldsymbol{g}^*))\tilde{\boldsymbol{N}}(\bar{\boldsymbol{L}},\boldsymbol{g}')\bar{\boldsymbol{L}}d\boldsymbol{g}^{'}_{r'g} \tag{5.46}$$

For the purpose of demonstration of our probability update scheme, we employ this first order correction in a similar vein as Garmestani et al.(2001). The average velocity gradient provided by the approach is enough to compute the necessary Jacobians used in updating the probability functions. There is, however, further room for development of the Green's function approach. Extensions to the case where state variables (eg. s in Eq. 5.37) evolve with deformation has been treated in Kumar and Dawson (1996a) for ODFs. A similar approach may be used where ensemble average of the state variable is computed for all grains of the same orientation. In addition, Eq. 5.45 can be enhanced by modifying it to calculate the velocity gradient as a function of distance from orientation $\boldsymbol{g}$. These enhancements will be a subject of future study.

5.4 Numerical examples

The improvement in prediction of texture and strains achieved by the COCF approach over ODF–based methods has been quantified through simple deformation analysis of a planar polycrystalline microstructure. Orientations of planar crystals are characterized by the two dimensional rotation $\boldsymbol{R}$ relating the crystal lattice frame to the reference sample frame. A parametrization of the associated rotation group is,

$$\boldsymbol{R} = \boldsymbol{I}cos(\boldsymbol{r}) - \boldsymbol{E}sin(\boldsymbol{r}) \tag{5.47}$$

where $\boldsymbol{r}$ is the angle between the crystal and sample axes, $\boldsymbol{E}$ is the two dimensional alternator ($E_{11} = E_{22} = 0, E_{12} = -E_{21} = 1$), and $\boldsymbol{I}$ is the identity tensor. Under the symmetry, crystal orientations can be described uniquely by parameters drawn from a simply connected fundamental region $[a, a+\pi)$. Out of convenience, we will restrict the choice of fundamental regions to the interval closest to the origin $(-\pi/2, \pi/2)$. Due to symmetry, the orientation $\pi/2$ is exactly the same as orientation $-\pi/2$. This constraint on the ODF and COCF is enforced in practise by using periodic boundary conditions in the finite element mesh (Sundararaghavan and Zabaras (2007)) wherein node at $g = \pi/2$ is considered a dependent node with field values updated using the values at $g = -\pi/2$. The crystal reorientation velocity follows by taking a derivative of relation Eq. 5.47 and using Ω from Eq. 5.35:

$$\boldsymbol{v} = \frac{1}{2}E.\Omega \tag{5.48}$$

The following parameters were used in the power law: $\dot{\gamma}^0 = 1\ sec^{-1}$, $s = 27.17$ MPa and $m = 0.05$. A specific crystal geometry with two slip systems at orientation $-\pi/6$ and $+\pi/6$ were considered. Kumar and Dawson (1996b) showed that this model leads to continuity in both reorientation velocity (v) and its gradient (∇v) over the

orientation space. Thus, a localized Lagrangian model is admissible for the test case. The imposed macroscopic velocity gradient $\boldsymbol{L}$ (tension) is given as:

$$\boldsymbol{L} = \eta \begin{bmatrix} 1 & 0 \\ 0 & -1 \end{bmatrix} \tag{5.49}$$

Here η is a constant strain rate taken to be 0.1. To test the proposed formulation, a representative volume element (RVE) containing 36 crystals was chosen. The microstructure is divided into $N \times N$ ($N = 18$) smaller elements and the orientations were randomly assigned. It is assumed that this microstructure contains adequate number of grains to represent the overall one and two–point statistics. To avoid edge effects in sampling two–point statistics, it is assumed that the microstructure is periodic in the x- and y- directions. Fig. 5.6 shows the initial microstructure as well as the initial ODF sampled from the RVE. The initial ODF is plotted on a finite element grid with nine line elements in the fundamental region $(-\pi/2, \pi/2)$ of a planar microstructure. Both locations of nodal points and integration points are indicated in Fig. 5.6(b).

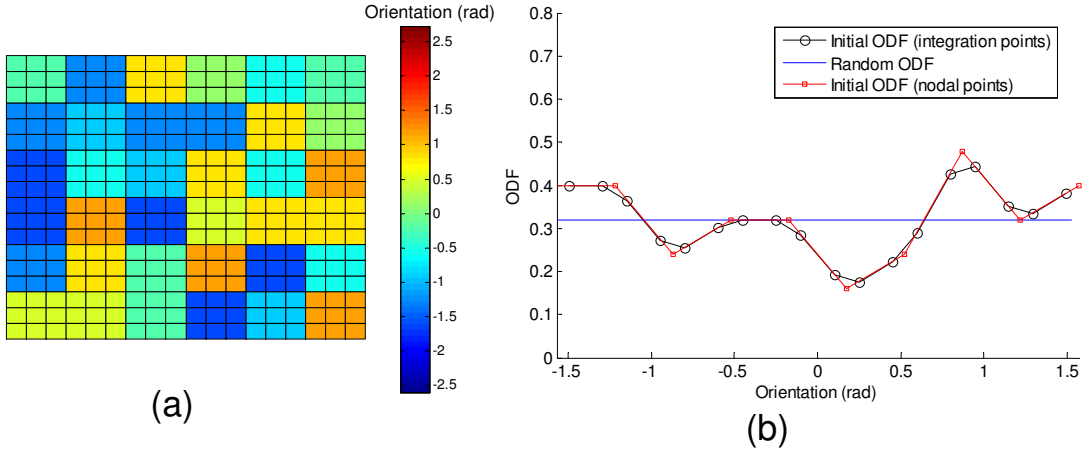

Figure 5.6: *(a) The initial (periodic) RVE with 324 elements and 36 crystals. Each crystal is divided into 9 elements. (b) The initial ODF sampled from the RVE is plotted on a finite element grid in the fundamental region* $(-\pi/2, \pi/2)$*. Both locations of nodal points and integration points are indicated.*

The COCF of the microstructure was sampled to compute probabilities at the node points of finite element meshes $M_{g'|gr}$, $M_{r|g}$ and M_g. Grains that have orientations close to the nodal points in the M_g mesh (within an error of $\pm\delta\boldsymbol{g}$, $\delta\boldsymbol{g} = 0.05rad$ being a small smoothing parameter in the g–space) are chosen for sampling. From these selected grains, a set of $\boldsymbol{r}$ vectors are drawn. The lengths and orientation of the $\boldsymbol{r}$ vectors are chosen based on the location of node points in the $M_{r|g}$ mesh. If the end point of these vectors fall in orientation that corresponds to a node point (within the smoothing parameter) in the COCF mesh $M_{g'|gr}$, then the weight for this node is incremented by one. The approach is illustrated in Fig.5.7. COCF weights are computed for all combination of node points in meshes $M_{r|g}$ and M_g. The nodal probabilities are then computed through normalization of the weights over the COCF mesh ($M_{g'|gr}$). Note that there is no limitation on the number of crystals in the actual microstructure when using the COCF mesh. The COCF is sampled using a fixed set of elements in the $\boldsymbol{g}$, $\boldsymbol{r}$ and $\boldsymbol{g}'$ meshes irrespective of how many grains are actually present in the microstructure. The present example was only used as a simple test case and larger systems (with more grains) could have been considered without restriction.

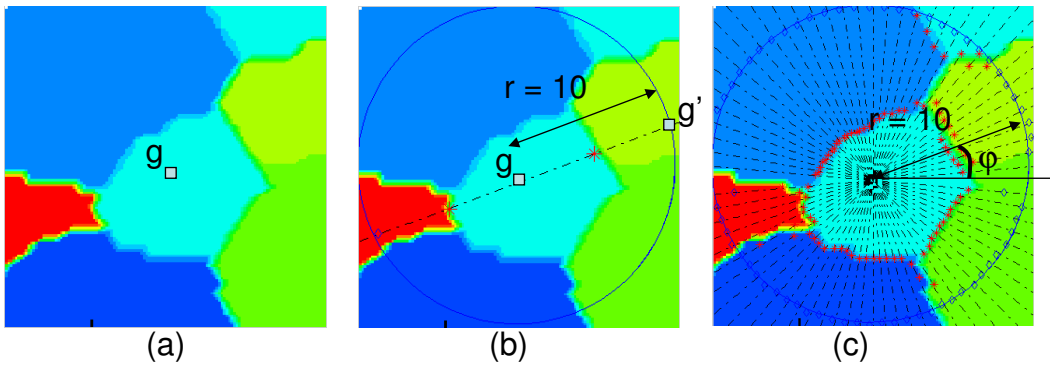

Figure 5.7: *Illustration of the sampling approach for COCF: (a) Sample a pixel in a grain with orientation g corresponding to a node point in the M_g mesh (b) Draw a line passing through the pixel to identify the orientation g′ at a distance r, increment the weights in a 3D array $F(g, r, g')$ (c) Sample lines at various angles to capture orientation dependence. The lengths and orientation of the lines are chosen based on the location of node points in the $M_{r|g}$ mesh.*

The Green's function ($G_{11,11}$) for the proposed constitutive model parameters was shown in Fig. 5.5. From analysis of the decay of this and other components of the tensor ($G_{ij,kl}$), a cut-off distance of 25 mm was chosen for the $M_{r|g}$ mesh. The microstructure is taken to be of length 100 mm, much larger than the cut–off distance of 25 mm, for computational convenience. A semi–circular mesh is adequate in the r–space owing to the symmetry of the Green's function. For maintaining consistency in the convolution operation in Eq. 5.42, two r–vectors $+\boldsymbol{r}$ and $-\boldsymbol{r}$ need to be sampled from location $\boldsymbol{g}$ to update the value of COCF weights at nodal location r in the $M_{r|g}$ mesh. Linear interpolation was used in the M_g and $M_{g'|gr}$ meshes with two integration points per element. In the $M_{r|g}$ mesh, four noded quadrilateral elements with bilinear interpolation and four integration points per element were employed.

Finite element integration techniques (where quantities are summed at gauss points) are used to compute integrals such as Eq. 5.22 and Eq. 5.42. This approach circumvents the issue of singularity of Green's functions at $\boldsymbol{r} - \boldsymbol{r'} = 0$ since Gauss points do not fall at this location[2]. However, smaller elements are needed close to the singularity to capture the sharp changes in the Green's function close to $\boldsymbol{r} - \boldsymbol{r'} = 0$. For this purpose, a convergence study was performed to select the best possible mesh in the $M_{r|g}$ space that allows good trade–off between computational speed and accuracy. Fig. 5.8 depicts various different meshes ($M_{r|g}$) used for testing the convergence of the Green's function approach. The Green's function shown in Fig. 5.5 is superposed on these meshes as a color contour. The meshes were adapted to capture the major variations in Green's function that occur at small values of $\boldsymbol{r} - \boldsymbol{r'}$.

In order to test the approach, an aggregate model was developed where a mesh in

[2]A proper solution to the singularity problem is to construct solutions for a finite small volume V_c surrounding point $\boldsymbol{r}$, then calculate the average value of the velocity gradient to replace the value at $\boldsymbol{r}$ (Kroner (1987)). The average value of velocity gradient $\boldsymbol{L}^0(\boldsymbol{g}^*)$ is given as:

$$\boldsymbol{L}^0(\boldsymbol{g}^*) = \bar{L} + \frac{1}{V_c} \int\limits_{r \in V_c} G(\boldsymbol{r} - \boldsymbol{r}^{'}) * \langle \tilde{\sigma}(\boldsymbol{r}^{'}) \rangle_{\boldsymbol{g}(r) = \boldsymbol{g}^*} d\boldsymbol{r}$$

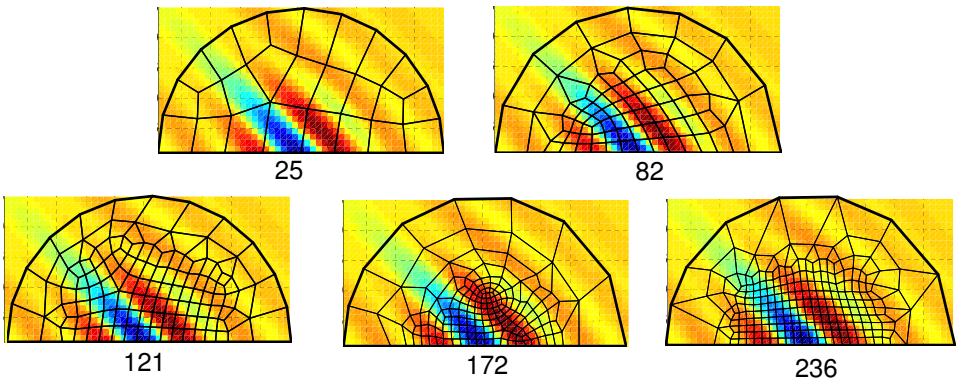

Figure 5.8: *Various meshes used to discretize the* $\boldsymbol{r}$ *space for testing the convergence of the Green's function approach. The Green's function* $G_{11,11}$ *is superposed on the r-mesh as a color contour.*

the r–space (a full circular mesh) is directly utilized at every integration point in the aggregate RVE to compute the local velocity gradients in the crystals. The approach is similar to the work of Lebensohn (2001) and Lee et al. (2011), except that Green's function convolution is performed in the real space instead of the k–space. A first order correction (eq. 5.46) is used similar to the COCF model. This approach, called the 'aggregate model', is more accurate than the COCF model as it explicitly includes the neighborhood of each crystal rather than an 'average' neighborhood computed during COCF sampling. The convergence results are shown in Fig. 5.9. The y-axis shows the l_2 norm of the change in nodal coordinates when using the current mesh (compared to the previous coarser mesh). The final microstructure at $t = 1$ sec is also shown for a few cases. An 82 element mesh in the r-space was chosen based on this study. We also tested the singularity averaging approach (Kroner (1987), see footnote 3) and found the change to be modest, with less than 4% change in the Green's function term for orientation $\boldsymbol{g} = -\pi/2$.

The algorithm for the COCF update is given in Table 1. In the algorithm, we first compute the velocity gradient of each orientation $\boldsymbol{g}$ using the Green's function approach. Subsequently, the velocity gradient is used to compute the reorientation velocities in the $M(g)$ mesh and the nodal displacements in $M(r|g)$ meshes. The

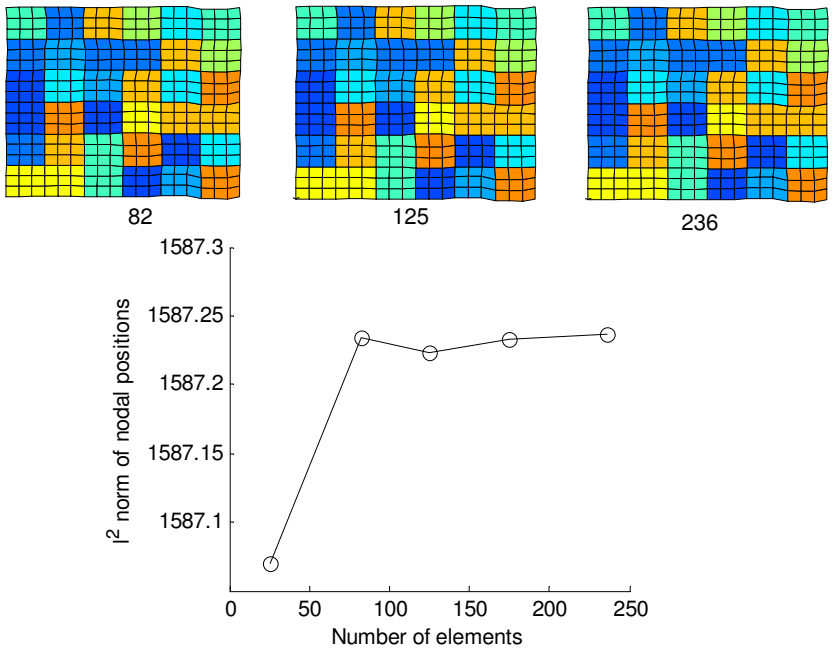

Figure 5.9: *Convergence with respect to r–mesh: The y-axis shows the l_2 norm of the change in nodal coordinates when using the current mesh (compared to the previous coarser mesh). The final microstructure at $t = 1$ sec is also shown for all cases. An 82 element mesh in the r-space was chosen based on this study.*

results are used to compute the Jacobians necessary to update the COCF. A total lagrangian approach is used where the fundamental region mesh for $\boldsymbol{g}$ and $\boldsymbol{g}'$ remain unchanged and the reorientations are only stored at the nodal points. If the reorientations are used to move the nodal locations, new orientation spaces are obtained, which are also valid fundamental regions (Kumar and Dawson (1996a)). Several ideas from the finite element community were used to solve the COCF evolution problem. For example, shape functions were used to calculate the gradient of deformation and the Jacobians, integrations were performed at the integration points to compute integrals (eg. in Eqs. (5.22–5.24,5.41,5.45)), interpolations are performed using shape functions to transfer deformation from nodes to integration points, smoothing is performed to transfer the computed jacobians from integration points to nodes. The total Lagrangian approach used in this work was found to be adequate up to a strain of 0.2. At larger strains, the nodal points may begin to overlap and interpenetrate.

To address such situations, remeshing techniques and updated lagrangian methods need to be developed in the future.

Table 5.1: Algorithm for COCF evolution

(1) Initialize meshes $M(g), M(r|g)$ and $M(g'|rg)$ and load probabilities $\mathcal{A}(g)$, $\mathcal{P}(r|g)$ and $\mathcal{F}(g'|(r,g))$ computed from the sampling algorithm.
(2) Apply time increment Δt.
(3) At current time step:
(3.1) Calculate $\bar{N}$ from Equation 5.41.
(3.2) Compute and store the Green's function at integration points of r–mesh (3.3) Compute and store $\tilde{\boldsymbol{\sigma}}$ at integration points of r–mesh connected to each orientation $\boldsymbol{g}$ using Eq. 5.46
(3.4) Loop over all nodes in mesh $M(\boldsymbol{g})$ and perform convolution of $\tilde{\boldsymbol{\sigma}}$ with the Green's function (Eq. 5.45) to compute the velocity gradient at each nodal orientation.
(4) Update Probabilities:
(4.1) Call constitutive model to compute reorientation velocities at nodes in the fundamental region (use velocity gradient found in step (3.4)).
(4.2) Update ODF using Eq. 5.11
(4.3) Compute velocity of nodes in meshes $M(r|g)$ using Eq 5.23 and deform the $M(r|g)$ meshes.
(4.4) Compute $\hat{\mathcal{P}}(\boldsymbol{r}|\boldsymbol{g})$ using Eq. 5.13 and then, compute $\hat{\mathcal{P}}(\boldsymbol{r})$ using Eq. 5.24
(4.5) Update COCF $\mathcal{F}(\boldsymbol{g}'|(\boldsymbol{r},\boldsymbol{g}))$ using Eq. 5.21
(5) Go to step (2) if time $t < t_{final}$.

The final texture predicted by the COCF model for the microstructure at $t = 1$ sec is shown in Fig. 5.10. From Kumar and Dawson (1996b), it is seen that texture from tension process leads to an orientation sink at zero degrees and source at $\pm\pi/2$; with the basin of the sink spanning all of orientation space. Thus the ODF will evolve exponentially with strain and eventually approach the asymptote, $A(r) = \delta(r - \pi/2)$. As seen in Fig. 5.10, there is tendency for crystals with angles close to the origin to reorient farther away (sink) and an associated increase in the ODF close to the ideal orientation of $\theta = \pm\pi/2$ (source) as expected.

The initial Lagrangian COCF $\hat{F}(\boldsymbol{g}'|(\boldsymbol{g} = -\pi/2, \boldsymbol{r}))$ and the COCF calculated

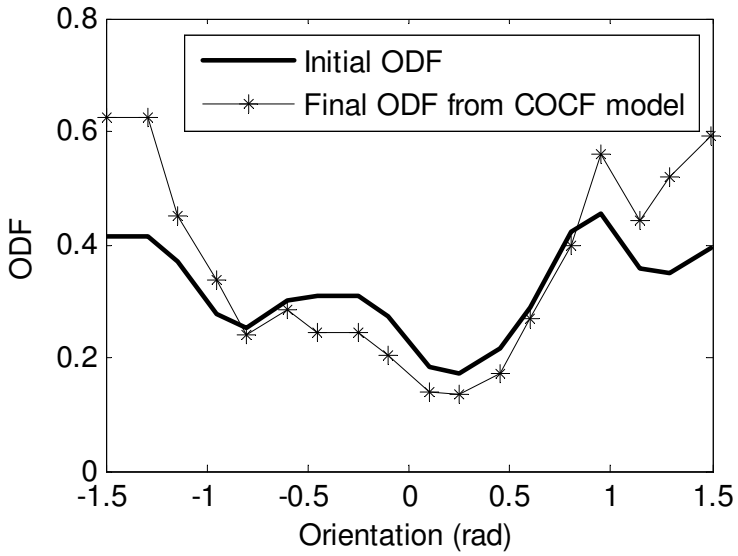

Figure 5.10: *The final texture predicted by the COCF model is shown. There is strong tendency for crystals with smaller angles (close to the origin) to reorient farther away from the origin. An increase in the ODF close to an ideal orientation of* $\theta = \pm\pi/2$ *is seen.*

at t = 1 sec is shown in Fig. 5.11. In this visualization, probability density of various orientations $\boldsymbol{g}'$ at distances $\boldsymbol{r}$ from orientation $\boldsymbol{g} = -\pi/2$ is shown over the r-mesh. At $t = 0$, the figure shows the average neighborhood of grain with orientation $\boldsymbol{g} = -\pi/2$ as computed from the sampling algorithm. The circles shown in the line connecting various $M(r|g)$ (semi-circle) meshes correspond to various values of $\boldsymbol{g}'$ from $(-\pi/2, \pi/2)$. Thus, the first mesh corresponds to the probability of finding orientation $\boldsymbol{g}' = -\pi/2$ at various distances r from orientation $\boldsymbol{g} = -\pi/2$, given as $\hat{F}(\boldsymbol{g}' = -\pi/2|(\boldsymbol{g} = -\pi/2, \boldsymbol{r}))$. The second mesh corresponds to $\hat{F}(\boldsymbol{g}' = -0.39\pi|(\boldsymbol{g} = -\pi/2, \boldsymbol{r}))$ etc. At $r = 0$, a delta function is obtained $\hat{F}(\boldsymbol{g}'|(\boldsymbol{g} = -\pi/2, \boldsymbol{r} = 0))$ with a large value (seen at node with $\boldsymbol{r} = 0$) in the first mesh and zeros at the same node in the other meshes (not shown). The evolved COCF at a strain of 0.1 is also shown.

The next figure (Fig. 5.12) shows another facet of the COCF $\hat{F}(\boldsymbol{g}' = -\pi/2|(\boldsymbol{g}, \boldsymbol{r}))$. Here, the representation depicts the probability of finding orientation $\boldsymbol{g}' = -\pi/2$ in the neighborhood of all other nodal orientations. The circles correspond to various val-

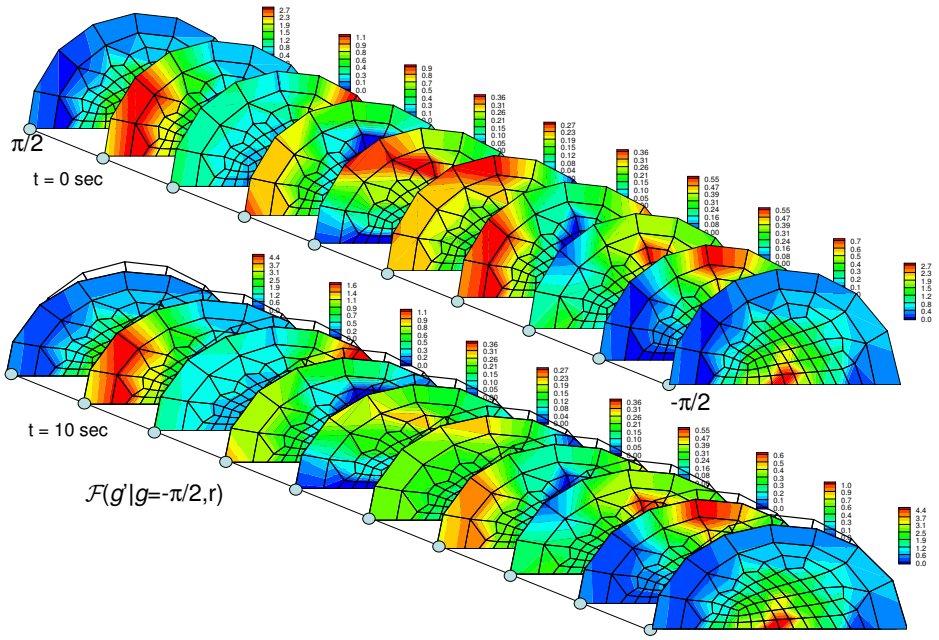

Figure 5.11: *Visualization of Lagrangian COCF* $\hat{F}(\boldsymbol{g}'|(\boldsymbol{g} = -\pi/2, \boldsymbol{r}))$*: The circles correspond to various values of* $\boldsymbol{g}'$ *from* $(-\pi/2, \pi/2)$*. The probability density of orientations* $\boldsymbol{g}'$ *at various distances* $\boldsymbol{r}$ *from orientation* $\boldsymbol{g} = -\pi/2$ *is shown over the r-mesh. The first mesh corresponds to* $\hat{F}(\boldsymbol{g}' = -\pi/2|(\boldsymbol{g} = -\pi/2, \boldsymbol{r}))$*, the second mesh corresponds to* $\hat{F}(\boldsymbol{g}' = -0.39\pi|(\boldsymbol{g} = -\pi/2, \boldsymbol{r}))$ *etc. The evolved COCF at* $t = 1$ *sec is also shown.*

ues of $\boldsymbol{g}$ from $(-\pi/2, \pi/2)$. The COCF shown here is closely related to that shown in Fig. 5.11 through the switching symmetry. Recall the equation for switching symmetry in this context $\mathcal{F}(\boldsymbol{g}' = -\pi/2|(\boldsymbol{g}, \boldsymbol{r})) = \mathcal{F}(\boldsymbol{g}|(\boldsymbol{g}' = -\pi/2, \boldsymbol{r}))\frac{\mathcal{P}(\boldsymbol{r}|\boldsymbol{g}'=-\pi/2)\mathcal{A}(\boldsymbol{g}'=-\pi/2)}{\mathcal{P}(\boldsymbol{r}|\boldsymbol{g})\mathcal{A}(\boldsymbol{g})}$. Note that the ratio of geometrical probabilities ($\mathcal{P}$) is not significantly different from the initial value of one under the moderate strain imposed here. Since the ODF at $g = -\pi/2$ at $t = 10$ sec is larger than ODF at any other orientation (from Fig. 5.10), this would imply that the COCF $\hat{F}(\boldsymbol{g}' = -\pi/2|(\boldsymbol{g}, \boldsymbol{r}))$ in Fig. 5.12 (at $t = 10$ sec) will be larger than the COCF shown in Fig. 5.11. This was used as a quick check to ensure that the switching symmetry is indeed satisfied during the simulation. Fig. 5.13 demonstrates the switching symmetry in more detail where the COCF $\hat{F}(\boldsymbol{g}' = 0.055\pi|(\boldsymbol{g} = -0.5\pi, \boldsymbol{r}))$ can be seen to be the same as $\hat{F}(\boldsymbol{g}' = -0.5\pi|(\boldsymbol{g} = 0.055\pi, \boldsymbol{r}))$ after multiplying it with the scaling factor.

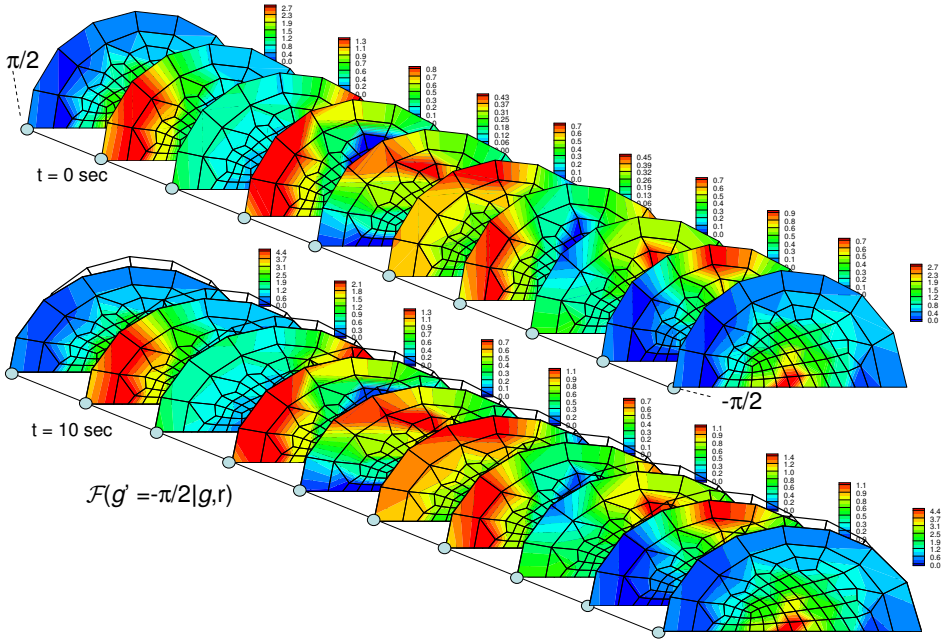

Figure 5.12: *Visualization of Lagrangian COCF* $\hat{F}(\boldsymbol{g}' = -\pi/2|(\boldsymbol{g}, \boldsymbol{r}))$*: The circles correspond to various values of* $\boldsymbol{g}$ *from* $(-\pi/2, \pi/2)$*. The probability density of orientation* $\boldsymbol{g}' = -\pi/2$ *at various distances* $\boldsymbol{r}$ *from orientations* $\boldsymbol{g}$ *is shown over the r-mesh. The evolved COCF at* $t = 1$ *sec is also shown. The COCF shown here is closely related to that shown in Fig. 5.11 through the switching symmetry.*

A comparison of the ODF predicted by the Taylor and COCF model at various times are shown in Fig. 5.14. The Taylor model predicts a sharper ODF at the location of the source ($\boldsymbol{g} = \pi/2$) as expected (Sundararaghavan and Zabaras (2006)). The ODF values for crystals with an orientation close to the location of the source (± 85.8 degrees) as predicted by the Taylor and COCF models are directly compared with that sampled from the aggregate model in Fig. 5.14(b,c). In both cases, the Taylor model predicts the largest ODF. The COCF model predicts an ODF that falls in between those predicted by the Taylor model and the aggregate model.

In order to visually interpret the results of the COCF model, we performed a direct comparison of the microstructure predicted by aggregate and COCF models in Fig 5.15. In the case of COCF model, the average velocity gradients predicted for each orientation (from Eq. 5.45) were used to update the microstructure mesh. In addition, crystal orientations are also updated. Compared to the aggregate model,

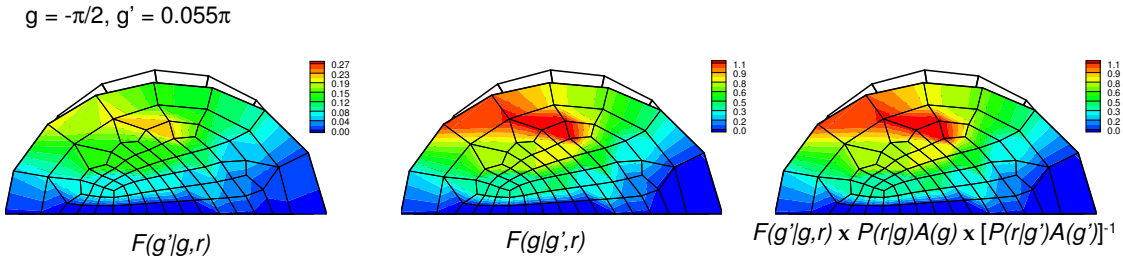

Figure 5.13: *Switching symmetry of the COCF at* $t = 1$ *sec: The COCF* $\hat{F}(\boldsymbol{g}' = 0.055\pi|(\boldsymbol{g} = -0.5\pi, \boldsymbol{r}))$ *can be seen to be equal to* $\hat{F}(\boldsymbol{g}' = -0.5\pi|(\boldsymbol{g} = 0.055\pi, \boldsymbol{r}))$ *after multiplying it with the scaling factor* $\frac{\mathcal{P}(\boldsymbol{r}|\boldsymbol{g})\mathcal{A}(\boldsymbol{g})}{\mathcal{P}(\boldsymbol{r}|\boldsymbol{g}')\mathcal{A}(\boldsymbol{g}')}$.

COCF approach is seen to give less pronounced deviations of intergranular strains from the applied macroscopic strain. However, the modes of deformation predicted in each crystal is close to those given by the aggregate model. Lower strains are primarily due to the fact that the COCF uses an average neighborhood for each orientation. In other words, it overlooks the differences in local neighborhood if two or more crystals have the same orientation but are at different locations. Alternately, the COCF results shown here can be seen as an ensemble average obtained for all microstructures with the given initial two–point descriptor. In contrast, the aggregate solution shown here provides a single sample from this large ensemble of microstructures. The crystal orientations and displacements predicted by Taylor and COCF models (in Fig. 5.15) were analyzed with respect to those predicted by the aggregate model. Fig. 5.16 shows the evolution of error in prediction of orientations and displacements as a function of time. The y-axes correspond to the l^2 norm of the difference in nodal values between Taylor/COCF meshes with respect to the aggregate mesh. The Taylor model gives a larger error in both orientation and displacement compared to the COCF model.

Fig. 5.17(a) shows that the use of COCF information reduces the error in prediction of displacements and orientations by 30 % when compared to the Taylor model. The percentage improvement remained almost constant for all strains over the simulation. More importantly, the 30 % improvement in error is achieved with a significantly less computational cost compared to the aggregate model. The COCF

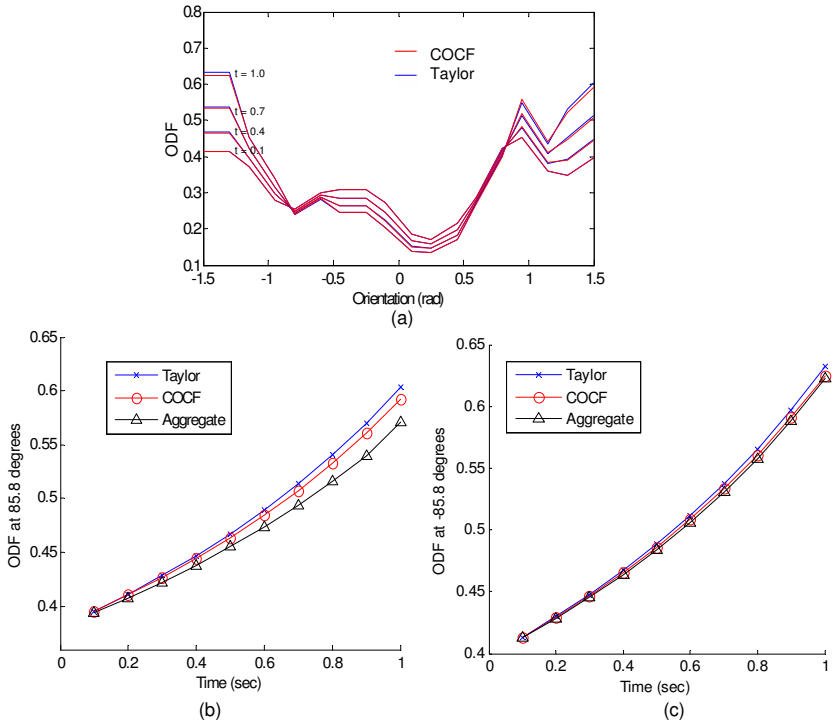

Figure 5.14: *(a) Comparison of the Lagrangian ODF predicted by the Taylor and COCF model at times t = 0.1,0.4,0.7 and 1.0 sec. (b,c) The ODF values at* ± 85.8 *degrees predicted by the Taylor and COCF models are compared with that predicted by the aggregate model.*

simulation for the test case was three times faster than the aggregate simulation. As shown in Fig 5.17(b), the computational time is significantly lower than a full aggregate model as the number of element increases. The simulation time for the COCF model is independent of the size of the RVE since the statistics are represented over the same COCF mesh for all cases. However, as the number of elements in the RVE increases, the computational expense in aggregate models increase as $O(N^2)$. The improvement in computational efficiency achieved by COCF models is most useful when performing multiscale design of industrial forming processes (eg. our work in Sundararaghavan and Zabaras (2008)). Once the initial COCF of the raw material (or preform) is known, the data can be used to perform more accurate multiscale simulations without resorting to the use of less accurate Taylor–based or computationally expensive FE–based microstructural models.

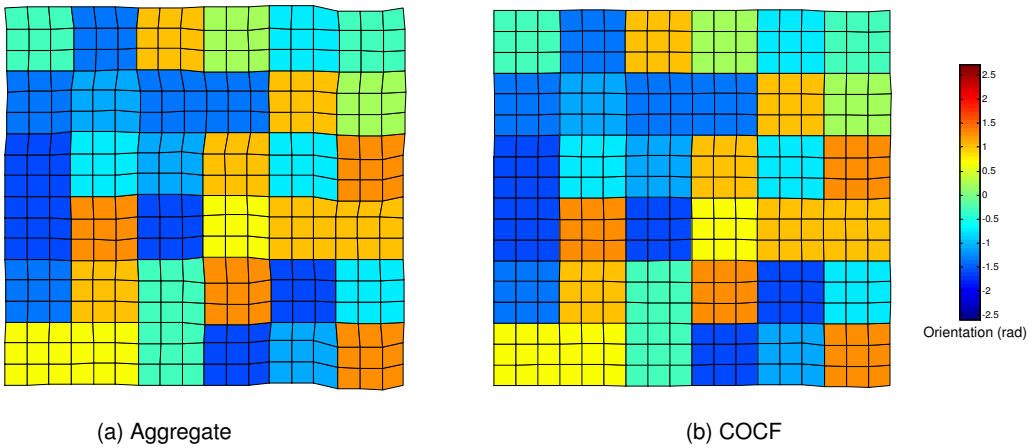

Figure 5.15: *Direct comparison of the microstructure predicted by (a) aggregate and (b) COCF model. The average velocity gradient predicted by the COCF model (for each orientation) is used to update the microstructure mesh.*

5.5 Conclusion

In this paper, a probabilistic model based on conditional orientation correlation function (COCF) is used for describing microstructure evolution during deformation. The COCF approach is an attempted move towards a new regime of computation where instead of microstructures, probabilistic descriptors are represented and evolved using finite element analysis. The COCF describes the probability density of occurrence of a crystal orientation $\boldsymbol{g}'$ at a distance $\boldsymbol{r}$ from a given orientation $\boldsymbol{g}$. As the microstructure evolves, the reoriented neighborhood and strain field close to an orientation ($\boldsymbol{g}$) is captured by updating the probability fields in a finite element mesh of the fundamental region of crystal orientation ($\boldsymbol{g}'$) attached to a mesh of distance vectors ($\mathbf{r}$). A novel total Lagrangian approach was developed to perform the probability update that allows evolution of probability densities while satisfying normalization constraints and symmetries.

In contrast to volume fraction (ODF) based models that do not use neighborhood information, COCF–based models capture length scales associated with the actual microstructure and include information about the neighborhood of each crystal ori-

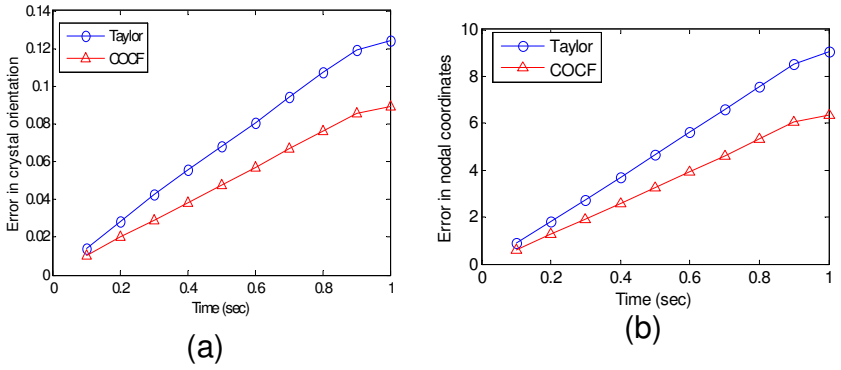

Figure 5.16: *Comparison of error in (a) crystal orientations and (b) nodal coordinates that arise in Taylor and COCF models. The errors correspond to l^2 norm of the difference in values between Taylor/COCF models with respect to the aggregate model. Errors are plotted as a function of simulation time.*

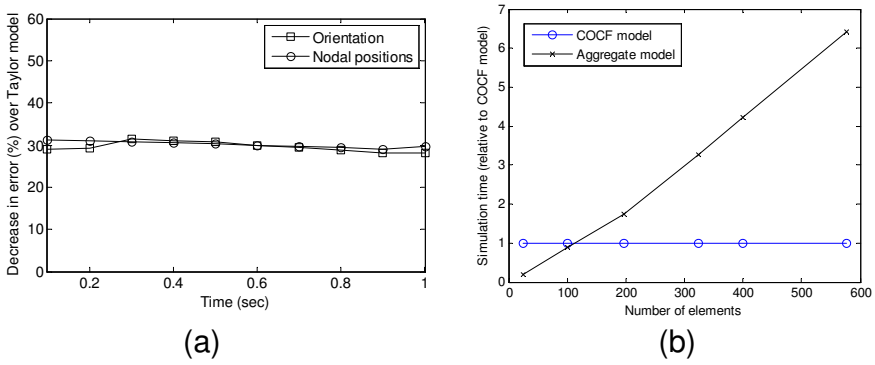

Figure 5.17: *(a) COCF model reduces the error in prediction of displacements and orientations by 30 % when compared to the Taylor model. (b) Comparison of computational speed of aggregate model with respect to COCF model as number of elements in RVE increases.*

entation. Thus, non–local interactions that lead to complex grain boundary evolution during loading may be statistically captured (using Green's functions). In contrast, Taylor models do not model equilibrium across grain boundaries. Finite element (FE) models with complete microstructural input can capture this effect, however, FE techniques are not of practical use in multiscale simulations due to large computational cost involved in modeling realistic microstructures.

Simulations comparing Taylor, COCF and aggregate models were presented for the case of deformation of a planar (2D) microstructure. Our simulation results indicate

that the COCF model decreases the error in prediction of texture and strain by about 30 %. The differences between a full microstructure simulation and a COCF–based simulation was primarily attributed to the fact that two–point descriptors contain an average neighborhood for each orientation. In other words, the differences in local neighborhood for two or more crystals with the same orientation that may be present at different locations is overlooked. Thus, the COCF model gives a more constrained solution than the actual deformation, but is less constrained than the deformation predicted by the one–point descriptor (eg. ODF/Taylor model) that has no neighborhood information. At larger strains, the fundamental region may get severely distorted and remeshing methods still need to be developed. In contrast to finite element methods for which simulation time increases with the size of the RVE, the simulation time is practically constant with the size or discretization of the microstructure. For realistic microstructures, the COCF approach is expected to be significantly faster than FE approaches. In the future, we plan to extend the approach to 3D orientation spaces (FCC, HCP crystals) to address the well–known limitations of Taylor models, and to problems involving twinning (eg. Abdolvand et al.(2011)).

CHAPTER VI

Suggestions for future research

6.1 Key Contributions of the dissertation

The following is a summary of the primary contributions that the research proposed in this dissertation provides for microstructure representation, reconstruction, property analysis and optimization.

- In Chapter 2, Markov Random Field approach for reconstructing diverse microstructure from two–dimensional microstructures is presented. We performed rigorous testing of the stereological features (eg. grain size histograms) and other engineering properties (elastic properties, stress distribution) of reconstructed microstructures. We extended the approach to 3D, and were able to reconstruct 3D images through matching of 3D slices at different voxels to the representative 2D micrographs.

- In Chapter 3, we have developed a rate-independent elasto-plastic model of BCC Galfenol single crystal for studying the effect of microstructure on mechanical properties. Both loading and unloading processes have been simulated and a finite strain homogenization algorithm has been developed to investigate final microstructural response. The 3D model developed reproduces experimental behavior of polycrystalline Galfenol under coupled magnetic and stress fields.

This current study shows that microstructural features play an important role in determining the final magnetostriction in Galfenol.

- In Chapter 4, we have employed data mining techniques to identify microstructural features (in the form of ODFs) that lead to an optimal combination of magnetostrictive strains, yield strength and elastic stiffness. Using this data mining method we can search for multiple microstructure that can result in optimal property in fraction of time as compared to conventional optimization methods.

- In Chapter 5, we have developed a probabilistic model based on conditional orientation correlation function (COCF) which is used for describing microstructure evolution during deformation. The COCF approach is an attempted move towards a new regime of computation where instead of microstructures, probabilistic descriptors are represented and evolved using finite element analysis.Our simulation results showed that the COCF model decreases the error in prediction of texture and strain by about 30 %. In contrast to finite element methods for which simulation time increases with the size of the RVE, the simulation time is practically constant with the size or discretization of the microstructure.

6.2 Development of Process Design Methodologies

In spite of this increased use of computer and information technologies in the analysis of deformation processes, selection of actual process design variables to optimize property distribution in materials still requires a significant amount of expert knowledge. To overcome this dependency and to create products with optimal properties, optimization-based design techniques for deformation processing would be valuable. The methodology described here would enable expansion of the conventional design space to include objectives such as to obtain desired microstructure in

the final product. However, to identify optimal processing paths that lead to these microstructures is still an open problem. It will be interest to develop a coupled macro-micro framework for multi-scale design of Galfenol where the macro- process parameters and processing sequence in cold-working processes can be altered to tune microstructure-sensitive material properties. The design problem of interest, such as to optimize engineering properties such as stiffness and yield strength through control of process parameters like die shapes and forging velocities, has several industrially relevant applications. Our approach can also be extended towards the control of a variety of properties (e.g. control of magnetic properties or material anisotropy that are dependent on the microstructure. In addition to deformation processing, thermal processing is also of future interest. Recent experimental studies have indicated that magnetostriction in single crystals with gallium content upto 17 at.% is only weakly dependent on the thermal history. However, increasing beyond 17 at.% Ga results in a decrease in magnetostriction when single crystals have been furnace cooled, whereas when these alloys are rapidly quenched into water from temperatures 800^oC, the magnetostriction is increased. Rapid cooling leads to the emergence of directional short range ordering of Ga atoms which strains the the b.c.c. lattice of Fe along [100] directions and increases magnetostriction. However, slow cooling allows the formation of an ordered phase that decreases magnetostriction. Thermal processing involves recrystallization of deformed grains with dislocation-free grains. A stored energy is introduced (resulting from an accumulation of dislocations during deformation) in the homogenization model. This involves modeling of strain energy development and nucleation deterministically based on grain boundary (GB) energy [141, 19, 109, 55]. GB nucleation is modelled by considering all orientations in the deformation texture as nuclei and distributing them in the deformed matrix depending on the stored energy [37, 40]. Recovery kinetics of a deformed grain is determined by the number of different activated slip systems during deformation [117] with several different acti-

vated slip systems leading to faster recovery. For modeling recrystallization textures, boundary mobilities of nuclei are assumed to be given by a mean-field approximation where the rate of growth is proportional to the variation in strain energy from the mean field energy. The driving force for primary static recrystallization results from the difference between the stored energy densities of the deformed matrix and the nucleus obtained from finite element simulations. Energy minimization methods ([127]) could be used to simulate aspects of grain growth kinetics. In this method, a hamiltonian which governs the grain growth in the lattice is minimized. The hamiltonian is defined based on the grain boundary curvature and the stored energy. Models with well-calibrated parameters [111, 123, 102, 110, 85] have indeed shown reasonable comparisons with experimental results.

6.3 Extending the approach to other alloys, including HCP metals

The ODF representation developed for cubic crystal structure of Galfenol can be extended towards modeling of hexagonally close packed crystals such as Titanium. Key differences in modeling approach followed for cubic crystals such as Galfenol and HCP crystals such as Titanium include (i) the fundamental region for the ODF for HCP crystals is different and a different ODF mesh is used. (ii) the predominant slip systems for HCP crystals are different and are shown in Figure 6.1. The constitutive model, however, is similar to that developed for Galfenol in chapter 3. The slip systems active in HCP metals are the basal systems, prismatic systems, and one family of pyramidal systems. Slip-system normals and slip directions are indicated in the conventional indices for HCP systems. Typically, the pyramidal slip systems are stronger than either the basal or prismatic systems, and in this work we considered cases of initial strength ratios with factors of 1.5 and 2 of prismatic and pyramidal

in comparison to the basal system.Only the basal and prismatic slip systems were activate in determining the model parameters given in Tables 6.1 and 6.2.

The slip system hardening model used in the examples is given as:

$$h^{\alpha\beta} = [q + (1 - q)\delta^{\alpha\beta}]h^{\beta}(\text{no sum on } \beta) \tag{6.1}$$

where h^{β} is a single slip hardening rate, and q is the latent-hardening ratio. The parameter q is taken to be 1.0 for coplanar slip systems and 1.4 for non-coplanar slip systems. For the single slip hardening rate, the following specific form is adopted:

$$h^{\beta} = h_o(1 - \frac{s^{\beta}}{s_s})^a \tag{6.2}$$

where h_o,a, and s_s are slip hardening parameters taken to be identical for a particular slip system.

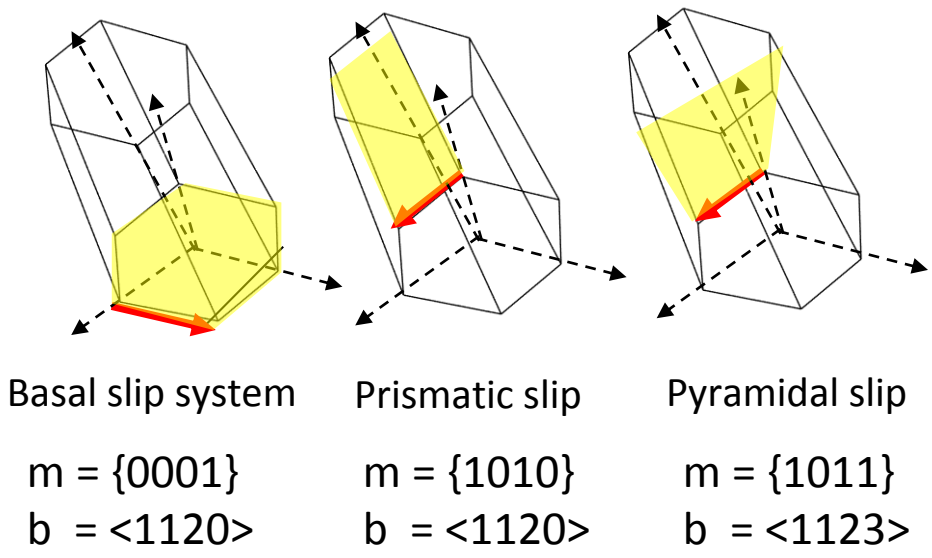

Figure 6.1: Pyramidal, basal, and prismatic slip systems used in titanium simulations

As a validation of the micro-scale texture evolution model, results are compared

with the experiments. The experiment corresponds to an z-axis compression with a strain rate of 0.001 $/s$ of Titanium polycrystal. The initial texturing of the material is assumed to be random, and this corresponds to a constant Lagrangian ODF of 1.2135. The reference fundamental region is discretized into 111 tetrahedral elements with cubic symmetry enforced in the solution procedure. Comparison of results of our model with the experiments is shown in Figure. 6.2. and 6.3

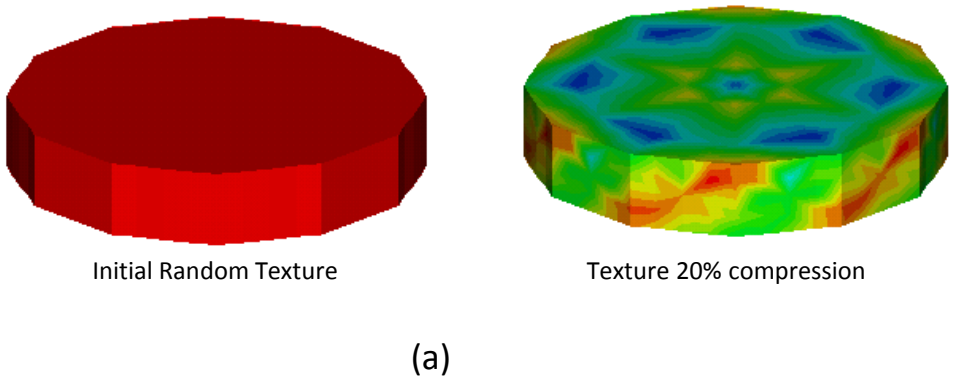

(a)

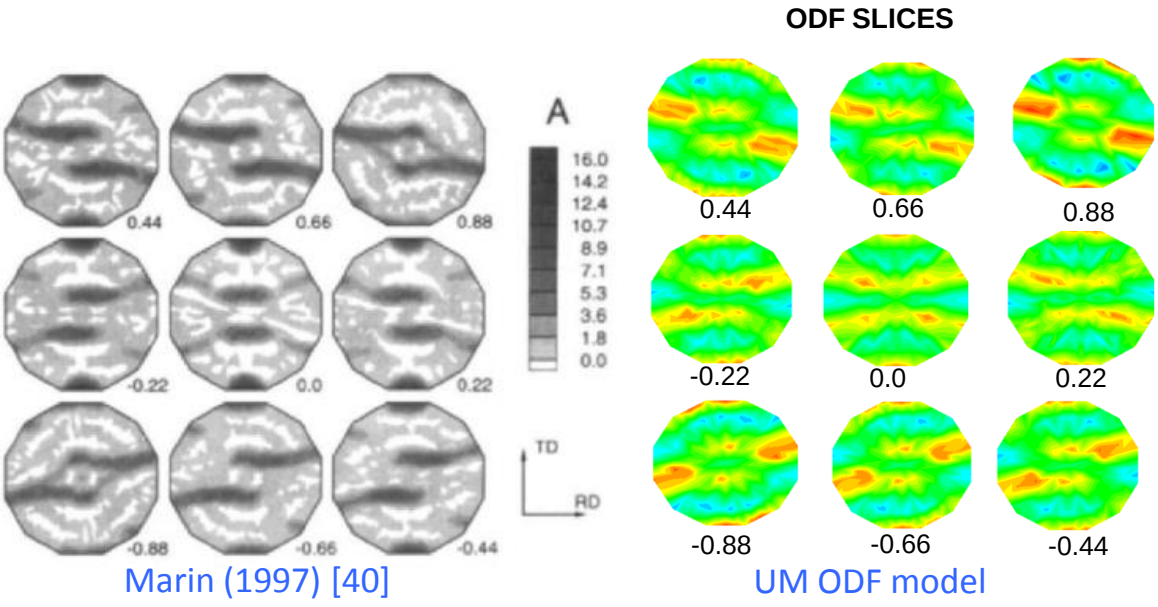

(b)

Figure 6.2: Comparison of texture evolution of Ti under plane strain compression using our ODF model after 200 sec of simple compression at the rate of $1e-3s^{-1}$

Table 6.1: Value of elastic parameters for single crystal HCP Titanium Alloys [121]

C_{11}	C_{12}	C_{13}	C_{33}	C_{55}
$125.3GPa$	$99.4GPa$	$68.8GPa$	$154.5GPa$	$31.6GPa$

Table 6.2: Crystal Plasticity parameters for HCP

s_0^{basal}	$s_0^{prismatic}$	$s_0^{pyramidal}$	h_0	a	s_s^{basal}	$s_s^{prismatic}$	$s_s^{pyramidal}$
$190MPa$	$250MPa$	$360MPa$	$400MPa$	1	$1000MPa$	$1500MPa$	$2500MPa$

Rigorous quantitative microstructural models of Titanium behavior at the meso-scale such as those developed here is expected to be important for controlling properties of commercially important components such as turbine blades and protective armors. Apart from texture, properties of metallic materials are affected by several characteristics that are stereological (grain sizes, shapes, grain boundary networks) attributes. The extension towards computing the effect of higher order features on properties described in this thesis will be useful towards this end.

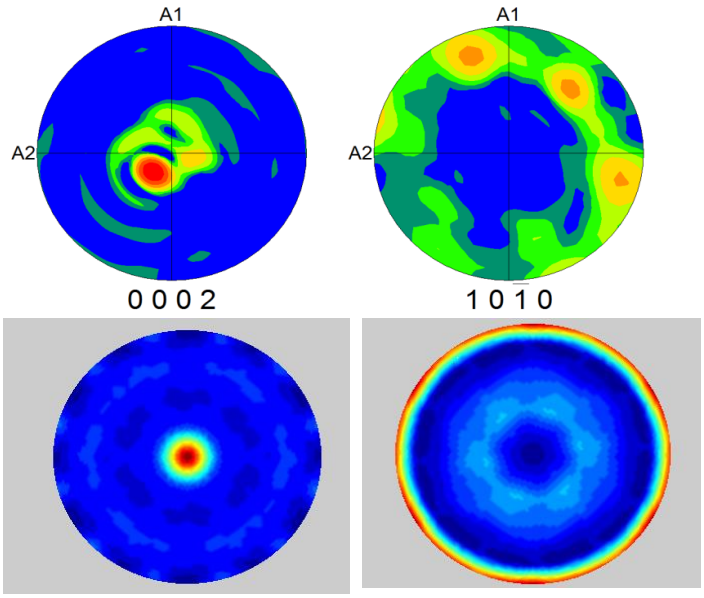

(a)

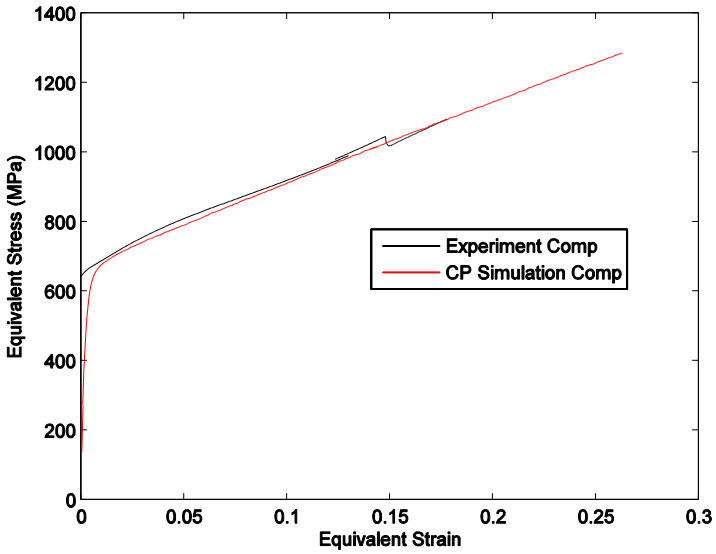

(b)

Figure 6.3: (a) Comparison for Pole Figure (b) Comparison of equivalent stress-strain response with results from experiments

BIBLIOGRAPHY

BIBLIOGRAPHY

[1] S. Acharjee and N. Zabaras. A proper orthogonal decomposition approach to microstructure model reduction in rodrigues space with applications to the control of material properties. *Acta Materialia*, pages 5627–5646, 2003.

[2] B. L. Adams, J. P Boehler, M. Guidi, and E. T. Onat. Group theory and representation of microstructure and mechanical behavior of polycrystals. *J. Mech Phys. Solids, 40*, pages 723–737, 1992.

[3] B. L. Adams, G. R. Canova, and A. Molinari. A statistical formulation of viscoplastic behavior in heterogeneous polycrystals. *Textures and Microstructures*, 11:57–71, 1989.

[4] B. L. Adams, X. C. Gao, and S. R Kalidindi. Finite approximations to the second-order properties closure in single phase polycrystals. *Acta Materialia*, 53(13):3563–3577, 2005.

[5] B. L. Adams, M. Lyon, and B. Henrie. Microstructures by design: linear problems in elastic–plastic design. *International Journal of Plasticity*, 20(8):1577–1602, 2004.

[6] F. Aherne, N. Thacker, and P. Rockett. The bhattacharyya metric as an absolute similarity measure for frequency coded data. *Kybernetika*, 32:1–7, 1997.

[7] J. Allison, D. Backman, and L. Christodoulou. Integrated computational materials engineering: A new paradigm for the global materials profession. *Journal of the Minerals Metals and Materials Society*, 58(11):25–27, 2006.

[8] N. S. Altman. An introduction to kernel and nearest-neighbor nonparametric regression. *The American Statistician*, 46(3):175–185, 1992.

[9] L. Anand and M. Kothari. A computational procedure for rate-independent crystal plasticity,. *Journal of the Mechanics and Physics of Solids*, 44:525–558, 1996.

[10] L. Anand and M. Kothari. A computational procedure for rate-independent crystal plasticity. *Journal of the Mechanics and Physics of Solids*, 44(4):525–558, 1996.

[11] S. Ankem and C. A. Greene. Recent developments in microstructure property relationships of beta titanium alloys. *Materials Science and Engineering A*, 263:127–131, 1999.

[12] W. D. Armstrong. Nonlinear behavior of magnetostrictive particle actuated composite materials,. *Journal of applied physics*, 87(6):3027–3031, 2000.

[13] R. J. Asaro and A. Needleman. Texture development and strain hardening in rate dependent polycrystals. *Acta Metall*, 33:923–953, 1985.

[14] M. F. Ashby and D. Cebon. Materials selection in mechanical design. *Le Journal de Physique IV*, 3(C7):C7–1, 1993.

[15] M. Ashikhmin. Synthesizing natural textures. *Proceedings of the 2001 symposium on Interactive 3D graphics*, pages 217–226, 2001.

[16] J. Atulasimha, A. B Flatau, and E. Summers. Characterization and energy-based model of the magnetomechanical behavior of polycrystalline iron–gallium alloys. *Smart materials and structures*, 16(4):1265, 2007.

[17] P. S. Bate and J. Quinta da Fonseca. Texture development in the cold rolling of if steel. *Materials Science and Engineering A*, 380(1-2):365–377, 2004.

[18] A. J. Beaudoin, H. Mecking, and U. F. Kocks. Development of localized orientation gradients in fcc polycrystals. *Philos Mag. A*, 73:1503–1518, 1996.

[19] A. J. Beaudoin, R. Srinivasan, and S. L. Semiatin. Microstructure modeling and prediction during thermomechanical processing. *JOM*, 54:25–29, 2002.

[20] R. Becker and S. Panchanadeeswaran. Effects of grain interactions on deformation and local texture in polycrystals. *Acta Metall Mater*, 43:2701–2719, 1995.

[21] R. Bellman. *Adaptive control processes: a guided tour*, volume 4. Princeton University Press Princeton, 1961.

[22] M. J. Beran, T. A. Mason, B. L. Adams, and T. Olson. Bounding elastic constants of an orthotropic polycrystal from measurements of the microstructure. *J. Mech Phys. Solids, 44, pp. 1543-1563*, 1996.

[23] J. Besag. Spatial interaction and the statistical analysis of lattice systems,. *Journal of the Royal Statistical Society Series B (Methodological)*, 36(2):192–236, 1974.

[24] A. Bhattacharyya. On a measure of divergence between two statistical populations defined by their probability distribution bull. *Calcutta Math Soc. 35*, pages 99–110.

[25] D. Bhattacharyya, G. B. Viswanathan, Robb Denkenberger, D. Furrer, and H. L. Fraser. The role of crystallographic and geometrical relationships between alpha and beta phases in an alpha beta titanium alloy. *Acta Materialia*, 51:4679–4691, 2003.

[26] J. S. D. Bonet. Multiresolution sampling procedure for analysis and synthesis of texture images. *In SIGGRAPH 97*, pages 361–368, 1997.

[27] A. Brahme, M. H. Alvi, D. Saylor, J. Fridy, and A. D. Rollett. 3d reconstruction of microstructure in a commercial purity aluminum. *Scripta Materialia*, 55(1):75–80, 2006.

[28] C. A. Bronkhorst, S. R. Kalidindi, and L. Anand. Polycrystalline plasticity and the evolution of crystallographic texture in fcc metals,. *Philos Trans R. Soc. Lond. A, 341*, pages 443–477, 1992.

[29] H. J. Bunge. *Texture Analysis in Materials Science*. (Butterworths) London, 1982.

[30] P. G. Callahan, J. P. Simmons, and M. De Graef. A quantitative description of the morphological aspects of materials structures suitable for quantitative comparisons of 3d microstructures. *MaterSci. Eng. 20*, 2012.

[31] L. M. Cheng, A. E. Nolting, B. Voyzelle, and C. Galvani. Deformation behavior of polycrystalline galfenol at elevated temperatures. In *Behavior and Mechanics of Multifunctional and Composite Materials*, volume 6526. J Proceedings of the SPIE, Volume 6526, 2007.

[32] J. Chraponski and W. Szkliniarz. Quantitative metallography of two-phase titanium alloys. *Materials Characterization*, 46:149–154, 2001.

[33] J. W. Christian and S. Mahajan. Deformation twinning. *Progress in Materials Science*, pages 1–20, 1995.

[34] A. Clement. Prediction of deformation texture using a physical principle of conservation,. *Materials Science and Engineering*, 55:203–210, 1982.

[35] Dorin Comaniciu, Visvanathan Ramesh, and Peter Meer. Kernel-based object tracking. *Pattern Analysis and Machine Intelligence, IEEE Transactions on*, 25(5):564–577, 2003.

[36] P. B. Corson. Correlation functions for predicting properties of heterogeneous materials. i. experimental measurement of spatial correlation functions in multiphase solids. *Journal of Applied Physics*, 45:3165–3170, 1976.

[37] I.L. Dillamore and H. Katoh. The mechanisms of recrystallization in cubic metals with particular reference to their orientation-dependence. *Metal Science*, 8(1):73–83, 1974.

[38] Y. Dong, S. Lefebvre, X. Tong, and G. Drettakis. Lazy solid texture synthesis. *Computer Graphics Forum*, 27(4):1165–1174, 2008.

[39] A. Efros and T. K Leung. Texture synthesis by non-parametric sampling. In *Computer Vision, 1999. The Proceedings of the Seventh IEEE International Conference on*, volume 2, pages 1033–1038. IEEE, 1999.

[40] O. Engler. Recrystallisation textures in copper-manganese alloys. *Acta materialia*, 49(7):1237–1247, 2001.

[41] Hosford W. F. *The mechanics of crystals and textured polycrystals*. Oxford University Press, New York, 1993.

[42] Vander Voort G. F. In *Metallography: principles and practice*. McGraw-Hill.

[43] Vander Voort G. F. Examination of some grain size measurement problems. In *Metallography: Past Present and Future*. American Society for testing and materials, 1993.

[44] R. Filip, K. Kubiak, W. Ziaja, and J. Sieniawski. The effect of microstructure on the mechanical properties of two-phase titanium alloys. *Journal of Materials Processing Technology*, 133:84–89, 2003.

[45] S. Ganapathysubramanian and N. Zabaras. Design across length scales: a reduced-order model of polycrystal plasticity for the control of microstructure-sensitive material properties. *Computer Methods in Applied Mechanics and Engineering*, 193(45):5017–5034, 2004.

[46] Edward J Garboczi. *Finite element and finite difference programs for computing the linear electric and elastic properties of digital images of random materials*. Building and Fire Research Laboratory, National Institute of Standards and Technology, 1998.

[47] H. Garmestani, S. Lin, B. L. Adams, and S. Ahzi. Statistical continuum theory for large plastic deformation of polycrystalline materials. *J Mech Phys Solids*, 49(3):589–607, 2001.

[48] M. G. Glavicic, J. D. Miller, and S. L. Semiatin. A method to measure the texture of secondary alpha in bimodal titanium-alloy microstructures. *Scripta Materialia*, 54:281–286, 2006.

[49] F. Glover. Heuristic for integer programming using surrogate constraints,. *Decision Sciences*, 8(1):156–166, 1977.

[50] D. E Goldberg and J. H Holland. *Genetic algorithms and machine learning*, volume 3. Springer, 1988.

[51] Morton E Gurtin. An introduction to continuum mechanics. Academic press, 1982.

[52] S Guruswamy, N Srisukhumbowornchai, A.E. Clark, J. B. Restorff, and M. Wun-Fogle. Strong, ductile, and low-field-magnetostrictive alloys based on fe-ga. *Scripta materialia*, 43(3):239–244, 2000.

[53] E. O. Hall. *Twinning and diffusionless transformations in metals*. Butterworths Scientific Publications, 1954.

[54] D. J. Heeger and J. R. Bergen. Pyramid-based texture analysis/synthesis. *In SIGGRAPH 95*, pages 229–238, 1995.

[55] A. Hildenbrand, L. S. Toth, A. Molinari, J. Baczynski, and J. J. Jonas. Self-consistent polycrystal modeling of dynamic recrystallization during shear deformation of ti if steel. *Acta Mater*, 47:447–460, 1999.

[56] J. H. Holland. Adaptation in natural and artificial systems,. *University of Michigan Press, Ann Arbor*, 1975.

[57] Ming-Kuei Hu. Visual pattern recognition by moment invariants. *Information Theory*, 8(2):179–187, 1962.

[58] E. Ising. Beitrag zur theorie des ferromagnetismus. *Zeitschrift für Physik A Hadrons and Nuclei*, 31(1):253–258, 1925.

[59] Kazufumi Ito and S.S. Ravindran. A reduced-order method for simulation and control of fluid flows. *Journal of computational physics*, 143(2):403–425, 1998.

[60] S. R. Kalidindi and H. K. Duvvuru. Spectral methods for capturing crystallographic texture evolution during large plastic strains in metals. *Acta Materialia*, 53(13):3613–3623, 2005.

[61] R. A. Kellogg, A. M. Russell, T. A. Lograsso, A. B. Flatau, A. E. Clark, and M. Wun-Fogle. Tensile properties of magnetostrictive iron gallium alloys. *Acta Mater. 52 (2004)*, pages 5043–5050.

[62] M. V. Klassen-Neklyudova. *Mechanical Twinning*. Springer, New York, 1960.

[63] U. F. Kocks, C. N. Tomé, and H. R. Wenk. *Texture and anisotropy - Preferred orientations in polycrystals and their effect on materials properties*. Cambridge University Press, Cambridge, 2000.

[64] J. Kopf, C. Fu, D. Cohen-Or, O. Deussen, D. Lischinski, and T. Wong. Solid texture synthesis from 2d exemplars. *ACM Transactions on Graphics (TOG)*, 26(3):2, 2007.

[65] E. Kroner. In J. Gittus and J. Zarka, editors, *Modelling Small Deformation of Polycrystals*, page 229. Elsevier/Applied Science, New York, 1987.

[66] A. Kumar and P. R. Dawson. The simulation of texture evolution using finite elements over orientation space i. *Comput Methods Appl. Mech. Engrg.*, 130:227–246, 1996.

[67] A. Kumar and P. R. Dawson. The simulation of texture evolution using finite elements over orientation space ii. application to planar crystals. *Comput Methods Appl. Mech. Engrg., 130*, pages 247–261, 1996.

[68] A Kumar and P. R. Dawson. Computational modeling of fcc deformation textures over rodrigues' space. *Acta Materialia*, 48(10):2719–2736, 2000.

[69] V. Kwatra, I. Essa, A. Bobick, and N. Kwatra. Texture optimization for example-based synthesis. *ACM Transactions on Graphics (Proc SIGGRAPH)*, 24(3):795–802, 2005.

[70] Wei L.-Y. and M. Levoy. Fast texture synthesis using tree-structured vector quantization. *In SIGGRAPH 00*, pages 479–488, 2000.

[71] R. Lakes. Deformation in extreme matter. *Science*, 288(5473):1976–7, 2000.

[72] R. A. Lebensohn. N-site modeling of a 3d viscoplastic polycrystal using fast fourier transform. *Acta mater*, 49:2723–2737, 2001.

[73] R. A. Lebensohn, O. Castelnau, R. Brenner, and P. Gilormini. Study of the antiplane deformation of linear 2-d polycrystals with different microstructures. *International Journal of Solids and Structures*, 42(20):5441–5459, 2005.

[74] E. H. Lee. Elastic-plastic deformation at finite strains. *Journal of Applied Mechanics*, 26(1969):1–6.

[75] P. S. Lee, H. R. Piehler, A. D. Rollett, and B. L. Adams. Texture clustering and long-range disorientation representation methods: application to 6022 aluminum sheet. *Metallurgical and Materials Transactions A*, 33(12):3709–3718, 2002.

[76] S.-B. Lee, R. A. Lebensohn, and A. D. Rollett. Modeling the viscoplastic micromechanical response of two-phase materials using fast fourier transforms. *International Journal of Plasticity*, 27(5):707–727, 2011.

[77] S. Lefebvre and H. Hoppe. Appearance-space texture synthesis. 25(3):541–548, 2006.

[78] D. S. Li, H. Garmestani, and B. L. Adams. A texture evolution model in cubic-orthotropic polycrystalline system. *International journal of plasticity*, 21(8):1591–1617, 2005.

[79] J.H. Li, X.X. Gao, J. Zhu, X.Q. Bao, T. Xia, and M.C. Zhang. Ductility, texture and large magnetostriction of fe–ga-based sheets. *Scripta Materialia*, 63(2):246–249, 2010.

[80] David G Luenberger and Yinyu Ye. *Linear and nonlinear programming*, volume 116. Springer, 2008.

[81] Hung V Ly and Hien T Tran. Modeling and control of physical processes using proper orthogonal decomposition. *Mathematical and computer modelling*, 33(1):223–236, 2001.

[82] Wei L.Y. *Texture synthesis by fixed neighborhood searching*. PhD thesis, Stanford University, 2002.

[83] M. Lyon and B. L. Adams. Gradient-based non-linear microstructure design. *Journal of the Mechanics and Physics of Solids*, 52(11):2569–2586, 2004.

[84] Mullins W. M. and Crane R. L. *Modeling and Quantification of Corroded Surfaces*. Proceeding of the tri-services corrosion conference Myrtle Beach SC, 1999.

[85] G. Gottstein L. Neumann H. Aretz M. Crumbach, M. Goerdeler and R. Kopp. Through-process texture modelling of aluminium alloys. *Modelling and Simulation in Materials Science and Engineering*, 12, 2004.

[86] JP MacSleyne, JP Simmons, and M De Graef. On the use of 2-d moment invariants for the automated classification of particle shapes. *Acta Materialia*, 56(3):427–437, 2008.

[87] S. Malinov and W. Sha. Application of artificial neural networks for modelling correlations in titanium alloys. *Materials Science and Engineering, A*, 365:202–211, 2004.

[88] C. Manwart, S. Torquato, and R. Hilfer. Stochastic reconstruction of sandstones,. *Phys Rev. E*, 62:893–899, 2000.

[89] D. L. McDowell. A perspective on trends in multiscale plasticity. *International Journal of Plasticity*, 26(9):1280–1309, 2010.

[90] D. L. McDowell and G. B. Olson. Concurrent design of hierarchical materials and structures. *Scientific Modeling and Simulations Springer Netherlands*, pages 207–240, 2009.

[91] L. Miaoquan, X. Aiming, H. Weichao, W. Hairong, S. Shaobo, and S. Lichuang. Microstructural evolution and modelling of the hot compression of a tc6 titanium alloy. *Materials Characterization*, 49:203–209, 2002.

[92] D. P. Mika and P. R. Dawson. Polycrystal plasticity modeling of intracrystalline boundary textures. *Acta Mater*, 47(4):1355–1369, 1999.

[93] A. Mikdam, A. Makradi, S. Ahzi, H. Garmestani, D. S. Li, and Y. Remond. A new approximation for the three-point probability function. *International Journal of Solids and Structures*, 46(21):3782–3787, 2009.

[94] A. Molinari, G. R. Canova, and S. Ahzi. A self consistent approach of the large deformation polycrystal viscoplasticity. *Acta Metallurgica*, 35:2983–2994, 1987.

[95] J. Ohser and F. Mucklich. Statistical analysis of microstructures. *Materials Science*, 2000.

[96] R. Paget and I. Longstaff. Texture synthesis via a noncausal nonparametric multiscale Markov random field. *IEEE Transactions on Image Processing*, 7(6):925–931, June 1998.

[97] J. S Peterson. The reduced basis method for incompressible viscous flow calculations. *SIAM Journal on Scientific and Statistical Computing*, 10(4):777–786, 1989.

[98] K. Popat and R. W Picard. Novel cluster-based probability model for texture synthesis, classification, and compression. pages 756–768, 1993.

[99] M. A. S. Qidwai, A. C. Lewis, and A. B. Geltmacher. Using image-based computational modeling to study microstructure–yield correlations in metals. *Acta Materialia*, 57(14):4233–4247, 2009.

[100] M. A. S. Qidwai, A. C. Lewis, and A. B. Geltmacher. Using image-based computational modeling to study microstructure–yield correlations in metals. *Acta Materialia*, 57(14):4233–4247, 2009.

[101] J. Quintanilla. Microstructure and properties of random heterogeneous materials: A review of theoretical results. *Polymer Engg Sci.*, 39:559–585, 1999.

[102] B. Radhakrishnan, G. B. Sarma, and T. Zacharia. Modeling the kinetics and microstructural evolution during static recrystallizationmonte carlo simulation of recrystallization. *Acta materialia*, 46(12):4415–4433, 1998.

[103] K. Rajan. Materials informatics,. *Materials Today*, 8(10):38–45, 2005.

[104] R. E. Reed-Hill, J. P. Hirth, and H. C. Rogers. *Deformation twinning*. Gordon & Breach, 1964.

[105] A. C. E. Reid, S.A. Langer, R C. Lua, V.R. Coffman, S-I. Haan, and R.E. Garcya. Image-based finite element mesh construction for material microstructures. *Comput. Mater. Sci. 43*, pages 989–999, 2008.

[106] A. C. E. Reid, R Lua, R E. Garcia, V.R. Coffman, and S.A. Langer. Modelling microstructures with oof2. *Int. J. Mater. Prod. Technol. 35*, pages 361–373, 2009.

[107] A. P. Roberts and E. J. Garboczi. Elastic properties of a tungsten-silver composite by reconstruction and computation. *J Mech Phys. Solids. 47*, pages 2029–2055, 1999.

[108] A. P. Roberts and S. Torquato. Chord-distribution functions of three-dimensional random media: Approximate first-passage times of Gaussian processes. *Physical Review E*, 59(5):4953–4963, 1999.

[109] A. D. Rollett. Overview of modeling and simulation of recrystallization. *Progress in materials science*, 42(1):79–99, 1997.

[110] A. D. Rollett, M. J. Lutton, and D. J. Srolovitz. Microstructural simulation of dynamic recrystallization. *Acta Metall*, 40:43–55, 1992.

[111] A. D. Rollett, D. J. Srolovitz, and M. P. Anderson. Simulation and theory of abnormal grain growth - anisotropic grain boundary energies and mobilities. *Acta Metall*, 37(4):1227–1240, 1989.

[112] Kirkpatrick S., C. Gelatt, and M. Vecchi. Optimization by simulated annealing,. *Science*, 220(4598):671–680, 1983.

[113] Zelinka S. and Garland M. Jump map based interactive texture synthesis. *ACM Trans Graph*, 23(4):930–962, 2004.

[114] A. A. Salem, S. R. Kalidindi, and R. D. Doherty. Strain hardening regimes and microstructure evolution during large strain compression of high purity titanium. *Scripta Materialia*, 46:419–423, 2002.

[115] A. A. Salem, S. R. Kalidindi, and S. L. Semiatin. Strain hardening due to deformation twinning in a-titanium: Constitutive relations and crystal-plasticity modeling. *Acta Materialia*, 53:3495–3502, 2005.

[116] G. B. Sarma, B. Radhakrishnan, and P. R. Dawson. Mesoscale modeling of microstructure and texture evolution during deformation processing of metals. *Adv Eng. Mater*, 4:509–514, 2002.

[117] M. Seefeldt, L. Delannay, B. Peeters, E. Aernoudt, and P. Van Houtte. Modelling the initial stage of grain subdivision with the help of a coupled substructure and texture evolution algorithm. *Acta Mater*, 49(2129-2143), 2001.

[118] V. Seetharaman and S. L. Semiatin. Microstructures and tensile properties of ti–45.5al–2nb–2cr rolled sheets. *Materials Science and Engineering A*, 299:195–209, 2001.

[119] C. E. Shannon. A mathematical theory of communication. *Bell SysTech. Journal, 27*, 1948.

[120] O. Sigmund and S. Torquato. Composites with extremal thermal expansion coefficients. *Applied Physics Letters*, 69(21):3203–3205, 1996.

[121] G. Simmons and H. Wang. *Single crystal elastic constants and calculated aggregate properties*. 1971.

[122] E. P. Simoncelli and J. Portilla. Texture characterization via joint statistics of wavelet coefficient magnitudes. In *Proc. 5th Int'l Conf. on Image Processing Chicago IL*, 1998.

[123] D. J. Srolovitz, G. S. Grest, and M. P. Anderson. Computer simulation of recrystallizationi. homogeneous nucleation and growth. *Acta metallurgica*, 34(9):1833–1845, 1986.

[124] Ravindran S.S. *Int J. Num Meth. Fluids*, 34:425–448, 2000.

[125] V. Sundararaghavan. Overview of reduced order and data mining methodologies for materials–by–design. *2009 US National Congress in Computational Mechanics (USNCCM9)*, 2009.

[126] V. Sundararaghavan and N. Zabaras. A dynamic material library for the representation of single phase polyhedral microstructures. *Acta Materialia*, pages 4111–4119, 2004.

[127] V. Sundararaghavan and N. Zabaras. Classification of three-dimensional microstructures using support vector machines. *Computational Materials Science*, 32:223–239, 2005.

[128] V. Sundararaghavan and N. Zabaras. On the synergy between classification of textures and deformation process sequence selection. *Acta Materialia*, pages 1015–1027, 2005.

[129] V. Sundararaghavan and N. Zabaras. Linear analysis of texture–property relationships using process-based representations of rodrigues space. *Acta materialia*, 55(5):1573–1587, 2007.

[130] V. Sundararaghavan and N. Zabaras. A multi-length scale continuum sensitivity analysis for the control of texture-dependent properties in deformation processing. *International Journal of Plasticity*, 24:1581–1605, 2008.

[131] V. Sundararaghavan and N. Zabaras. A statistical learning approach for design of polycrystalline materials. *Journal of statistical learning and data mining*, 1(5):306–321, 2009.

[132] G. I. Taylor. Plastic strain in metals. *J Inst Metals*, 62:307–325, 1938.

[133] J. Tiley, T. Searles, E. Lee, S. Kar, R. Banerjee, J. C. Russ, and H. L. Fraser. Quantification of microstructural features in α/β titanium alloys. *Materials Science and Engineering A*, 372:191–198, 2004.

[134] S. Tsurekawa, S. Nakamichi, and T. Watanabe. Correlation of grain boundary connectivity with grain boundary character distribution in austenitic stainless steel. *Acta Materialia*, 54(13):3617–3626, 2006.

[135] S. Umekawa, R. Kotfila, and O. D. Sherby. Elastic properties of a tungsten-silver composite above and below the melting point of silver. *J Mech Phys. Solids*, 13(4):229–230, 1965.

[136] F. Warchomicka, M. Stockinger, and H. P. Degischer. Quantitative analysis of the microstructure of near beta titanium alloy during compression tests. *Journal of Materials Processing Technology*, 177:473–477, 2006.

[137] G. S. Was, V. Thaveeprungsriporn, and D. C. Crawford. Grain boundary misorientation effects on creep and cracking in ni-based alloys. *J Metals*, 50:44–49, 1998.

[138] O. Watanabe, H. M. Zbib, and E. Takenouchi. Crystal plasticity: micro-shear banding in polycrystals using voronoi tessellation. *International Journal of Plasticity*, 14(8):771–788, 1998.

[139] I. Weiss and S. L. Semiatin. Thermomechanical processing of alpha titanium alloys–an overview. *Materials Science and Engineering, A*, 263:243–256, 1999.

[140] H. Wenk. *Preferred orientation in deformed metals and rocks, an introduction to modern texture analysis*. Academic Press, Inc., Orlando, FL, 1985.

[141] H. R. Wenk, G. Canova, Y. Brechet, and L. Flandin. A deformation based model for recrystallization of anisotropic materials. *Acta Mater*, 45(8):3283–3296, 1997.

[142] N. J. Wittridge and R. D. Knutsen. A microtexture based analysis of the surface roughening behaviour of an aluminium alloy during tensile deformation. *Mater Sci. Eng*, 269(1):205–216, 1999.

[143] Qing Wu and Yizhou Yu. Feature matching and deformation for texture synthesis. 23(3):364–367, 2004.

[144] Tong X., Zhang J., Liu L., Wang X., B. Guo, and Shum H.-Y. Synthesis of bidirectional texture functions on arbitrary surfaces. *In SIGGRAPH '02*, pages 665–672, 2002.

[145] H. Xu, D. A. Dikin, C. Burkhart, and W. Chen. Descriptor-based methodology for statistical characterization and 3d reconstruction of microstructural materials. *Computational Materials Science*, 85:206–216, 2014.

[146] L y Wei, S. Lefebvre, V. Kwatra, and G. Turk. *State of the Art in Example-based Texture Synthesis:in EUROGRAPHICS 2009*. State of the Art Report, 2009.

[147] C. L. Y. Yeong and S. Torquato. Reconstructing random media ii three-dimensional media from two-dimensional cuts. *Physical Review E*, 58(1):224–233, 1998.

[148] T. H. Yu and C. H. Koo. Microstructural evolution of a hot-rolled ti–40al–10nb alloy. *Materials Science and Engineering A 239-240*, pages 694–701, 1997.

[149] N. Zabaras, V. Sundararaghavan, and S Sankaran. An information theoretic approach for obtaining property pdfs from macro specifications of microstructural uncertainty. *TMS letters*, 3(1):1–4, 2006.

[150] K. S. Zhang, M. S. Wu, and R. Feng. Simulation of microplasticity-induced deformation in uniaxially strained ceramics by 3-d voronoi polycrystal modeling. *International Journal of Plasticity*, 21(4):801–834, 2005.

[151] S. Zhu, Y. Wu, and D. Mumford. Filters, random fields and maximun entropy (frame) - towards a unified theory for texture modeling. *International Journal of Computer Vision*, 27(2):107–126, 1998.